Building Blocks for Wavelength Converters

A Study of Monolithic Devices in Piezoelectric Materials

Forsch, M.

DOI
10.4233/uuid:09223911-3c3e-42f4-a94a-e40640d5acfc

Publication date
2020

Document Version
Final published version

Citation (APA)
Forsch, M. (2020). *Building Blocks for Wavelength Converters: A Study of Monolithic Devices in Piezoelectric Materials* (2020-27 ed.). [Dissertation (TU Delft), Delft University of Technology]. Casimir PhD Series. https://doi.org/10.4233/uuid:09223911-3c3e-42f4-a94a-e40640d5acfc

Building Blocks for Wavelength Converters

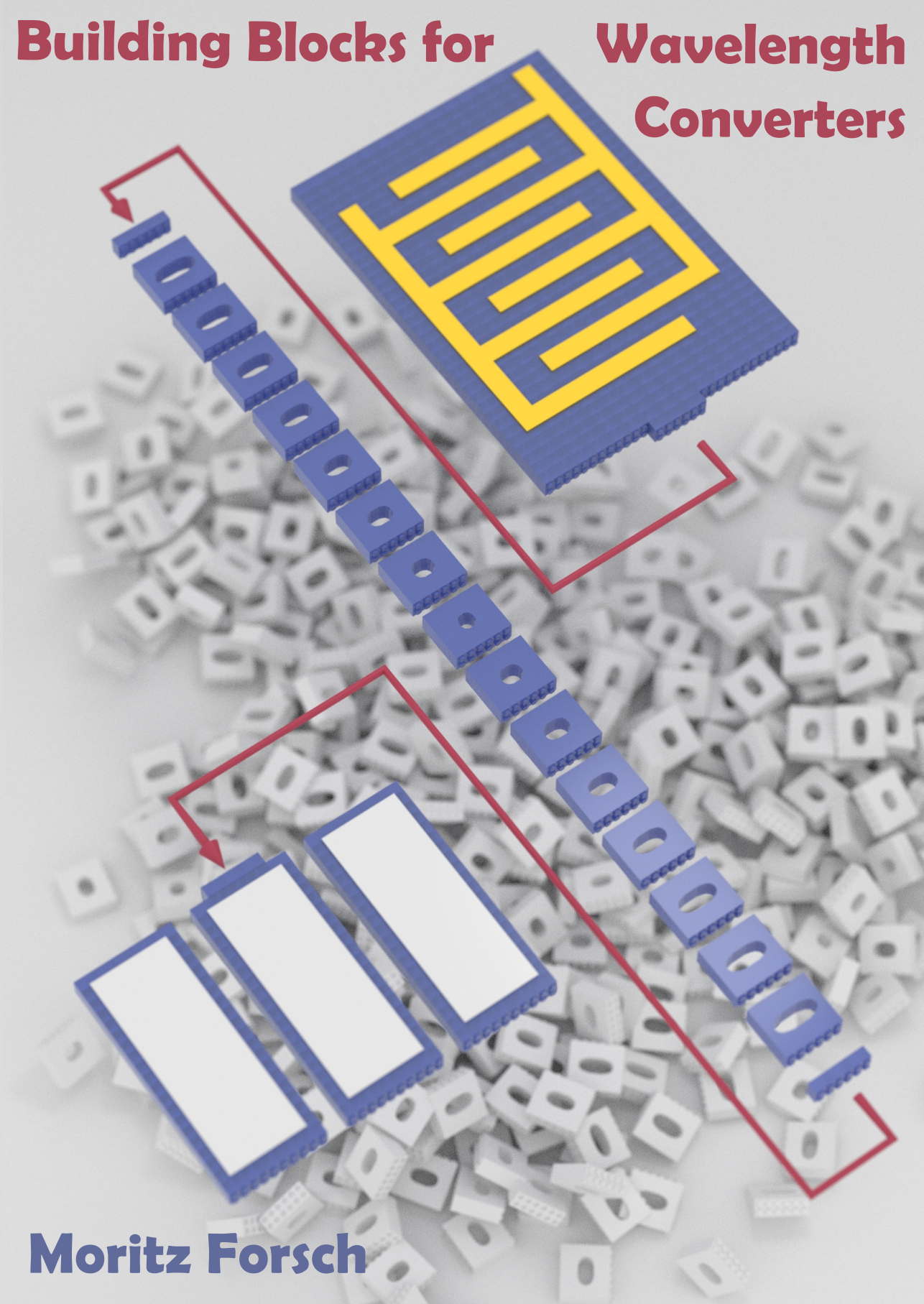

Moritz Forsch

Building Blocks for Wavelength Converters

A Study of Monolithic Devices in Piezoelectric Materials

Building Blocks for Wavelength Converters

A Study of Monolithic Devices in Piezoelectric Materials

Dissertation

for the purpose of obtaining the degree of doctor
at Delft University of Technology
by the authority of the Rector Magnificus, prof. dr. ir. T.H.J.J. van der Hagen,
chair of the Board for Doctorates
to be defended publicly on
Thursday 17 December 2020 at 10:00 o' clock

by

Moritz FORSCH

Master of Science in Physics,
Universität Regensburg, Germany
born in Duisburg, Germany.

This dissertation has been approved by the promotors.

Composition of the doctoral committee:

Rector Magnificus,	chairperson
Dr. S. Gröblacher,	Delft University of Technology, promotor
Prof. dr. L. Kuipers,	Delft University of Technology, promotor
Independent members:	
Prof .dr. Y. M. Blanter	Delft University of Technology
Prof. dr. ir. R. Hanson	Delft University of Technology
Dr. S. C. Conesa-Boj	Delft University of Technology
Prof. dr. E. Verhagen	AMOLF
Prof. dr. I. Favero	Paris Diderot University

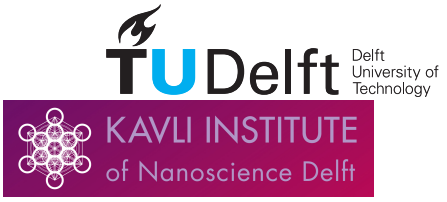

Keywords: Optomechanics, Piezoelectrics, Semiconductors, Wavelength Conversion

Printed by: Ipskamp Printing

Cover: Lego Nanobeam. by Moritz Forsch

ISBN 978-90-8593-453-0
Casimir PhD Series, Delft-Leiden 2020-27

An electronic version of this dissertation is available at
http://repository.tudelft.nl/.

to Loes

Contents

1

Introduction

The field of optomechanics provides a set of tools for the investigation of massive, mechanical systems. These tools can be exploited for applications such as sensing, as well as for fundamental research. Particularly in the realm of fundamental research, recent demonstrations have shown coherent control over non-classical states of such oscillators, motivating further quantum-technological applications. Such systems can be engineered to a high degree and allow coupling to many systems such as optical cavities or superconducting circuits. Particularly GHz-frequency optomechanical devices have entered the spotlight as a platform where the quantum ground state of motion can be readily accessible. Combined with the prospect of coupling to other quantum systems in this frequency domain, using mechanical resonators for wavelength conversion is a natural step. In this first chapter, we will introduce the basic concepts of optomechanics and wavelength conversion and put them in the context of specific measurement protocols.

1.1. Microwave-to-optics conversion for optical interfaces to superconducting circuits

Superconducting circuits are one of the most advanced quantum computing platforms, to date allowing processing with over 50 individually controllable qubits [1, 2]. So far, all experiments with multiple qubits have relied on all participating qubits being in the same cryogenic environment. This approach limits the scale of experiments due to the finite cooling power of dilution fridges and number of necessary drive and control lines. In addition, this approach limits the usefulness of such quantum computing nodes to local computation. In order to link several of such nodes over long distances into a quantum internet [3], a low-loss transmission channel for quantum information is necessary. For applications beyond the connection between two adjacent laboratories, the only viable option for such a channel are telecom wavelength photons and fiber-optic channels. In order to use telecom photons to share quantum information

from superconducting qubits over long distances, we need one crucial element: a transducer that can convert single quanta between the microwave and optical domains while adding a negligible amount of noise. This conversion can be realized by coupling the electric and optical degrees of freedom inside a nonlinear crystal using the electro-optic effect. However, the electro-optic effect is weak. In order to overcome this, on-chip electro-optic modulators typically rely on a large footprint compared to state-of-the art optical microcavities. Alternatively, an intermediate mode can be used. Mechanical vibrations, or phononic modes, are an excellent candidate for such an intermediate mode. Particularly attractive is their high degree of engineerability and allows for independent optimization of the opto- or electromechanical couplings. Recently, quantum control over mechanical resonators at GHz frequencies have been demonstrated independently from both the microwave [4–8] and optical [9–12] domains. With such high-frequency mechanical modes, it is then possible to realize a resonant interaction between the microwave and mechanical modes. This is typically done by coupling to piezoelectric moments of (a part of) the mechanical resonator. Further, the mechanical mode can be parametrically coupled to an optical cavity through the radiation pressure force in an optomechanical cavity. One advantage of this approach is that optomechanical devices typically do not rely on material-intrinsic resonances and can be designed to operate at telecom wavelengths. In the following section, we will briefly introduce optomechanics in general and then focus on the specific optomechanical system which is used throughout the rest of this thesis.

1.2. GHz-Optomechanical Crystals

Cavity optomechanics generally deals with optical cavities, where the motion of a mechanical degree of freedom shifts the cavity resonance. Thus, an oscillation at ω_m of this degree of freedom produces a modulation of the intracavity photon number with modulation frequency ω_m. While there are various implementations of such systems, we focus on only one type of optomechanical device: the 1D-nanobeam optomechanical crystal (OMC). This design has been a workhorse for various opto- and electro-opto-mechanical experiments. Initially developed in the Silicon-on-Insulator (SOI) material platform [13], the design has since been used in a variety of dielectrics such as aluminium nitride (AlN) [14, 15], gallium arsenide (GaAs) [16, 17], gallium phosphide (GaP) [18, 19], diamond [20], lithium niobate ($LiNbO_3$)[21], and silicon nitride (SiN) [22]. These structures can be engineered to exhibit optical modes that lie spectrally in the host material's transparency window. For technological reasons, they are typically designed for the optical telecom band and often exhibit mechanical eigenfrequencies of a few GHz. In this section, we describe the working principle of this design as well as the contributions to the optomechanical coupling rate.

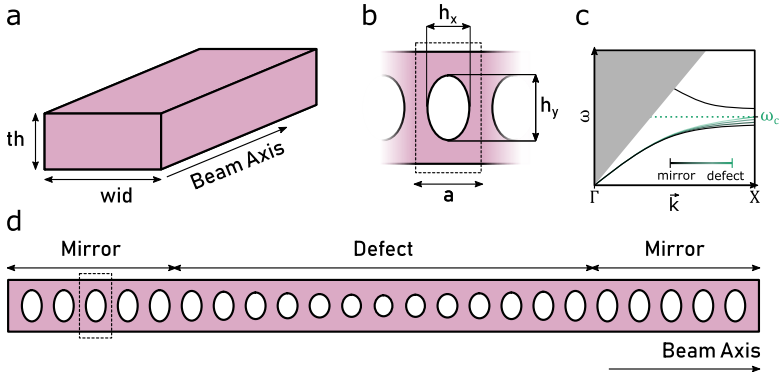

Fig. 1.1 | Anatomy of a Nanobeam OMC a)The nanobeam as a simple waveguide can already confine light and mechanical motion in the two dimensions perpendicular to the beam axis. By patterning such a beam with a periodic hole array, we can turn it into a Bragg mirror for light as well as phonons (b). Illustration of the resulting optical band structure (black curve) (c). The grey area is the light cone and contains non-guided modes. The key feature of this band structure is a band gap near the X point. In order to use two of these Bragg-mirrors to form a cavity (d), we need to create a defect state in the band gap. This is done by changing the hole size towards the center of the defect (d), which moves the lower band up into the band gap (color bar in c).

1.2.1. Anatomy of a Nanobeam OMC

The basic idea of a nanobeam optomechanical crystal is to have an integrated optical and mechanical cavity, where the modes overlap to a high degree. In order to realize this, we start with a suspended 1D beam with characteristic thickness *th* and width *wid* (fig. 1.1a), which confines light in the two directions perpendicular to the beam axis. Both *th* and *wid* need to be on the order of the target wavelength for the waveguide to only host a single transversal mode. Typical values in this work are $th \sim 250$ nm and $wid \sim 500$nm. In order to also obtain confinement along the beam axis, we pattern a 1D photonic crystal along the axis of the nanobeam (fig. 1.1b), which is reflective for light at frequencies inside the bandgap (fig. 1.1c). This reflector is parametrized by an ellipse with axes of lengths h_x and h_y, as well as the lattice constant a (fig. 1.1b). The typical length scale for these parameters is a few 100 nanometer. In order to form a cavity, we use two of these 1D photonic crystals and pattern a defect between them (fig. 1.1d). In this defect, we adiabatically change the hole dimensions towards the center such that the lower band (fig. 1.1c) is pulled up into the band gap and serves as a defect state at $\omega = \omega_c$. While these Bragg mirrors are reflective for light at a certain wavelength λ_c, the same is true for acoustic waves with $\lambda_{sound} \approx \lambda_c$. Thus, the structure in fig. 1.1 can also confine acoustic modes in the central defect region. It is important to note that the mirror region only works as a reflector for mechanical modes which are symmetric with respect to the beam axis. With the design principles laid out, we can now look at the modes of these structures and how they couple to each other. Intuitively, this is best done by looking at the modes and their spatial extents. To this end, we show the simulated optical and mechanical

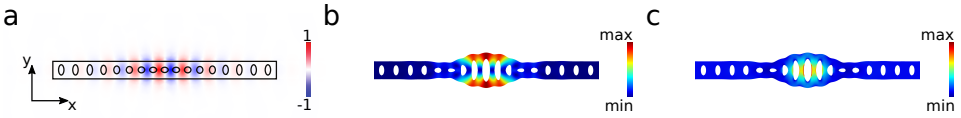

Fig. 1.2 | Optical and Mechanical Modes of a Nanobeam Nanobeam OMCs exhibit an optical mode which is localized in the center of the beam (a). Here, we display the E_y component of the normalized electric field of the mode. The beam also hosts a co-localized mechanical mode. In **b** and **c**, we show the normalized mechanical displacement and strain in the material, respectively (The strain in c is shown in color. The deformation is the same as in b). Notably, the largest electric fields of the optical mode (a) coincide with the maxima of the mechanical stress in the nanobeam (c). This overlap facilitates a large contribution to the optomechanical coupling in these devices.

modes in Figure 1.2. Shown are the E_y component of the normalized electric field of the optical mode (a), as well as the displacement (b) and the induced strain (c) of the mechanical breathing mode. For commonly used dielectrics such as silicon and gallium arsenide, these devices are often designed to exhibit optical resonances in the telecom band ($\lambda_c \sim 1550$nm). The mechanical modes of the structure then have a wavelength comparable to λ_c, typically resulting in a frequency of a few GHz. In the following section, we will discuss how the interaction between these modes is realized.

1.3. Optomechanical Interaction and Hamiltonian

Generally, the optomechanical coupling is defined as a shift of the optical cavity resonance ω_c due to a displacement of the mechanical oscillator x and it is generally given by

$$g_{OM} = \frac{\partial \omega_c(x_m)}{\partial x_m}. \tag{1.1}$$

However, a more commonly used metric is the single photon coupling rate g_0, which is given by

$$g_0 = g_{OM} \cdot x_{zpf}. \tag{1.2}$$

This coupling rate gives the optical resonance shift when the mechanical oscillator is displaced by its zero point fluctuation, x_{zpf}. The coupling can be further broken down to contributions arising from different effects: the moving dielectric boundary (MB) and the photoelastic effect (PE).

$$g_0 = (g_{OM,MB} + g_{OM,PE}) \cdot x_{zpf}. \tag{1.3}$$

The moving boundary effect relies on the changing geometry due to the mechanical mode to produce a resonance shift. The photoelastic effect, on the other hand, couples strain resulting from a displacement of the mechanical oscillator (see Figure 1.2c) to a change in the refractive index and thus, the optical resonance [23].

For a mechanical oscillator of frequency $\omega_m/2\pi$, the zero-point-motion is given by the oscillator displacement x_m corresponding to the zero-point-energy

$E_{zpf} = \frac{1}{2}\hbar\omega_m$. This zero-point motion, x_{zpf}, is then given by

$$x_{zpf} = \sqrt{\frac{\hbar}{2m_{eff}\omega_m}}. \tag{1.4}$$

In this case, we consider the mass m_{eff} of the oscillator to be the moving mass, which is defined as

$$m_{eff} = \int \rho \frac{\mathbf{q}(\mathbf{r})}{max(\mathbf{q}(\mathbf{r}))} d\mathbf{r}, \tag{1.5}$$

Where $\mathbf{q}(\mathbf{r})$ is the shape of the mechanical mode and ρ the density of the material. The moving mass of the mode shown in fig. 1.2 is typically on the order of 100 fg. At a mechanical frequency of $\omega_m/2\pi = 3$ GHz, this results in a zero-point-motion of $\sim$4fm. For the types of OMCs discussed in the previous section, this results in coupling rates of $g_0/2\pi \sim 1$ MHz.

The Optomechanical Hamiltonian

Both the mechanical oscillator and the optical cavity can be treated as quantum harmonic oscillators and as such are independently governed by the Hamiltonians

$$\hat{H}_{mech} = \hbar\omega_m \left(\hat{b}^\dagger \hat{b} + \frac{1}{2}\right) \tag{1.6}$$

and

$$\hat{H}_{opt} = \hbar\omega_c \left(\hat{\alpha}^\dagger \hat{\alpha} + \frac{1}{2}\right), \tag{1.7}$$

respectively. Here, the operators $\hat{b}^\dagger$ and $\hat{b}$ ($\hat{\alpha}^\dagger$ and $\hat{\alpha}$) are the creation and annihilation operators of the mechanical (optical) mode. In this picture, the displacement of the mechanical oscillator, x is defined as

$$\hat{x} = x_{zpf}\left(\hat{b}^\dagger + \hat{b}\right). \tag{1.8}$$

The optomechanical coupling is then a perturbation of the optical cavity resonance ω_c due to a displacement of the mechanical oscillator, x, and can be expanded as follows:

$$\omega_c(x) = \omega_c(0) + \left.\frac{\partial\omega_c(x)}{\partial x}\right|_0 \cdot x + \left.\frac{\partial^2\omega_c(x)}{\partial x^2}\right|_0 \cdot x^2 + \cdots \tag{1.9}$$

As we are dealing with small displacements of the mechanical mode, we truncate this series after the first order. Together with eq. 1.7 and eq. 1.8, we then arrive at the interaction term for the optomechanical coupling:

$$\hat{H}_{int} = \hbar g_0 \left(\hat{b}^\dagger + \hat{b}\right)\hat{\alpha}^\dagger\hat{\alpha}. \tag{1.10}$$

When we drive the system with a laser at ω_L, the optomechanical Hamiltonian is often considered in a frame rotating at the laser frequency $\omega_L = \omega_c + \Delta$.

1

This is realized with the unitary transformation $\hat{U} = exp\left(i\omega_L \hat{\alpha}^\dagger \hat{\alpha} t\right)$. In this frame the full Hamiltonian then takes the shape

$$\hat{H}_{\text{full,rot}} = -\hbar\Delta\hat{\alpha}^\dagger\hat{\alpha} + \hbar\omega_m\hat{b}^\dagger\hat{b} - \hbar g_0\left(\hat{b}^\dagger + \hat{b}\right)\hat{\alpha}^\dagger\hat{\alpha}. \tag{1.11}$$

This Hamiltonian is intrinsically non-linear and relates the displacement of the oscillator to the photon number which is proportional to the radiation pressure force. For the devices considered in this work, the coupling rate g_0 is much smaller than the decay rate of the optical cavity. As such, we can consider the optical field to consist of a coherent state with average amplitude $\bar{\alpha}$ and a fluctuating term $\delta\hat{\alpha}$, giving us the substitution $\hat{\alpha} = \bar{\alpha} + \delta\hat{\alpha}$. The interaction term of eq. 1.11 can now be expanded in powers of $\bar{\alpha}$. The term which is quadratic in $\bar{\alpha}$ corresponds to an average radiation pressure force, which results in a small displacement offset of the oscillator. Neglecting the zeroth order term due to the comparatively small magnitude, we are left with the first-order terms. We introduce the real-valued intracavity field $\sqrt{\bar{n}_{\text{cav}}} = |\bar{\alpha}|$ and arrive at an approximate interaction term [24]

$$\hat{H}_{\text{int,lin}} \approx -\hbar g_0\sqrt{\bar{n}_{\text{cav}}}\left(\delta\hat{\alpha}^\dagger + \delta\hat{\alpha}\right)\left(\hat{b}^\dagger + \hat{b}\right). \tag{1.12}$$

This approximation actually gets rid of the non-linearity in eq. 1.11 and leaves us with the so-called linearized Hamiltonian, which is commonly used in cavity optomechanics. Here, we can also introduce $g = g_0\sqrt{\bar{n}_{\text{cav}}}$ as the cavity-enhanced coupling rate which means that the optomechanical coupling can be boosted by increasing the driving amplitude. If the optical cavity is sufficiently narrow compared to the mechanical frequency of the oscillator, the cavity is called sideband resolved. In this case, with a laser at $\Delta = \pm\omega_m$, the optical cavity can be used to select between two interactions in this Hamiltonian. While the topic of sideband resolution will be discussed in the following section, it is relevant to discuss these two interactions here in greater detail. Both of these interactions are three-wave mixing processes, which result in Stokes or anti-Stokes scattering between photons and phonons.

Two-Mode-Squeezing Interaction

For a blue-detuned laser at $\Delta = +\omega_m$, we can selectively drive the two-mode-squeezing interaction:

$$\hat{H}_{\text{TMS}} = -\hbar g_0\sqrt{\bar{n}_{\text{cav}}}\left(\delta\hat{\alpha}^\dagger\hat{b}^\dagger + \delta\hat{\alpha}\hat{b}\right) \tag{1.13}$$

The resulting Stokes-scattering process down-converts the blue detuned input photon to the cavity resonance. The excess energy is deposited into an excitation of the mechanical mode. This process results in the pairwise creation of excitations in the mechanical mode and the optical field.

Beamsplitter Interaction

For a red-detuned laser at $\Delta = -\omega_m$, we instead drive the beamsplitter interaction:

$$\hat{H}_{\text{BS}} = -\hbar g_0\sqrt{\bar{n}_{\text{cav}}}\left(\delta\hat{\alpha}^\dagger\hat{b} + \delta\hat{\alpha}^\dagger\hat{b}\right) \tag{1.14}$$

Here, the anti-Stokes scattering process up-converts the red-detuned drive photons to the cavity resonance, at the cost of removing an excitation from the mechanical mode. This process effectively swaps an excitation from the mechanical mode to the anti-Stokes field. The selection of interactions based on the laser detuning works best in the sideband-resolved limit where κ is small compared to ω_m. In the following section, we will discuss the role of sideband resolution and its implications, as well as the measurement techniques used for the experiments in this work.

1.4. Sideband Resolution and Photon Counting

Sideband resolution and the associated ability to selectively drive certain interactions is not an on/off criteria, but rather a gradual scale. In the sideband resolved limit ($\kappa/\omega_m \ll 1$), we have perfect selectivity of the beamsplitter- and two-mode squeezing interactions. However, as κ/ω_m becomes larger, we start accidentally driving the unwanted process as well. In order to illustrate this process, we consider the case where the laser is red detuned from the optical cavity ($\omega_l = \omega_c - \omega_m$). In this case, the desired interaction is the beamsplitter interaction, where scattering events up-convert the input photons to the optical resonance. This is shown as the blue peak in fig. 1.3a. This interaction is enhanced because the target state is resonant with the optical cavity (green line in fig. 1.3a). However, if the cavity is not perfectly sideband resolved, there is only a finite suppression of the two-mode squeezing interaction, which excites the mechanical mode (red peak in fig. 1.3a). The reason for the finite suppression is that the down-converted target state at $\omega_l - \omega_m$ is not completely off-resonant to the optical cavity. We can further look at how the ratio κ/ω_m affects the suppression of this unwanted interaction. This is shown in fig. 1.3b. Importantly, we reach the point of 50% suppression when $\kappa/4\omega_m = 1$. As we can see from the figure, there is no sharp cutoff, but the reduction in selectivity for larger κ/ω_m has implications on measurements.

Photon Counting

With a weak coherent drive tone and a linear Hamiltonian such as the one in eq. 1.12 it is only possible to interact with Gaussian states of the mechanical mode. In order to circumvent this and gain insight into non-Gaussian states, we can make use of a non-linear detection method: photon counting using single photon detectors (SPDs). With this method, a detection event projects the state into a non-Gaussian basis which can then be used to make an assumption about the state of the mechanical mode. However, this approach only works if no more than one photon impinge on the detector at one time and if most of the photons originate from an optomechanical scattering process. The former is realized by using weak pump pulses such that the probability of a single scattering event taking place is $p_s \ll 1$. The latter we can realize by spectrally filtering the light coming from the device, which consists of reflected pump light, as well as desired and undesired scattered tones (shown in black, red, and blue in fig. 1.3a). This can be achieved by tuning a sufficiently narrow-band Fabry-Pérot cavity into resonance with the optical mode. In addition to cleaning

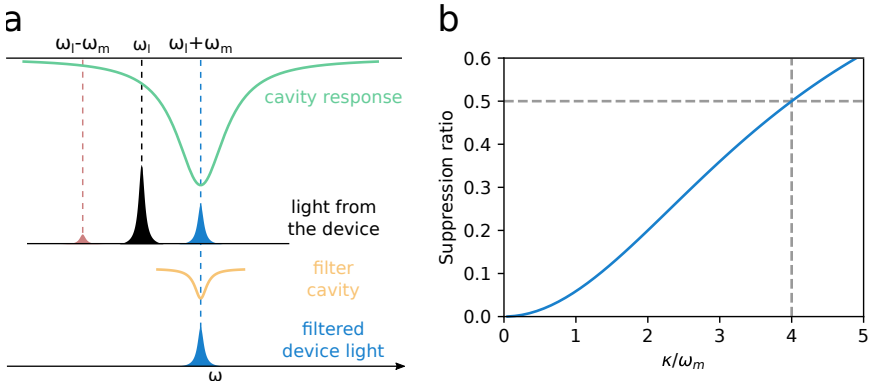

Fig. 1.3 | Sideband Resolution a) In the example of a red sideband drive ($\omega_l = \omega_c - \omega_m$), the optical cavity enhances the beamsplitter interaction which results in the up-conversion of drive photons (black) to the cavity resonance (blue). The two-mode squeezing interaction is suppressed as the resulting down converted photons (red) are off-resonant to the optical cavity. In order to detect only photons originating from the desired scattering process, the device light needs to be filtered using a Fabry-Pérot cavity (shown in yellow) which is tuned into resonance to the optical mode (green). This filtering removes both the unwanted scattered photons (red) and residual drive light (black), leaving only the desired photons to be detected. b) Shown is the rate of the undesired interaction normalized to that of the desired one. For values of $\kappa/\omega_m < 4$, this interaction is suppressed by more than 50%.

the device light of the pump tone, the cavity also removes scattered photons from the unwanted scattering process, leaving us only with scattered photons from the desired interaction. A subsequent detection event on a single photon detector now becomes a witness of a scattering event. In the case where the laser is blue-detuned from the optical cavity, we predominantly drive the two-mode-squeezing interaction, which means that a detected photon heralds the excitation of the mechanical mode. If, on the other hand, the laser is red-detuned from the optical cavity (see fig. 1.3a), a detection event implies the swapping of a single excitation from the mechanical mode to the readout photon [12].

In the regime of weak coherent excitation, we are limited to interacting with small occupations of the mechanical mode. This becomes particularly interesting, when the mechanical mode is near its quantum ground state. Then, single mechanical excitations become appreciably large and the thermal motion vanishes. This can be achieved by placing the sample in a commercial dilution refrigerator with a base temperature of $\sim$10mK. At such temperatures, the Bose-Einstein distribution predicts average occupations of a few-GHz mode of $\bar{n}_{\mathrm{th}} \sim 1 \times 10^{-8}$. In this regime, we can regard the mechanical mode as a quantum harmonic oscillator and applying the lowering operator to the ground state mechanical mode should return zero. The scattering rates for the red (blue) sideband drives are given by $\Gamma_R \propto n_{\mathrm{th}}$ ($\Gamma_B \propto n_{\mathrm{th}} + 1$), where n_{th} is the thermal occupation of the mode in the presence of an optical drive. At occupations near the ground state of motion, the difference between the

two becomes appreciable and can be used to retrieve the actual occupation of the mode [25]. The measured thermal occupation is then given by $n_{th} = \Gamma_R/(\Gamma_B - \Gamma_R)$.

Accidental Heating of the Mode

While a GHz-frequency oscillator should have a negligible thermal occupation when cooled to ∼10mK, in practice the theoretical values are not achieved due to accidental heating of the mode. The biggest source of heating is due to unwanted absorption of the drive laser in the material. This is largely a material- or surface chemistry dependent effect and can be attributed among others to surface states [26] and two-photon-absorption [18]. One other source of accidental heating is related to sideband resolution and scattered photons corresponding to the unwanted interaction. This process is suppressed (see fig. 1.3b) and the resulting scattered photons are filtered out from the device light and not detected. However, the fact that these scattering processes occur at all results in unwanted excitations (de-excitations) in the case of a red (blue) detuned laser. A direct consequence of this process is that the scattering rates from the red (blue) sideband drives is increased (reduced) resulting in an elevated measured occupation and a higher thermal noise background. Typically these experiments are carried out in a pulsed fashion where the device is re-initialized to its ground state between pulses. The probability of a scattering event occurring, P_s, in these experiments scales with the pump power. Typically probabilities in these experiments are on the order of a few percent per pulse. In this context, one undesired and one desired scattering event need to take place within the same pulse in order to have an appreciable effect on the measured temperature. The probability of such a double event is very rare ($P_s^2 \sim 1 \times 10^{-4}$, if $P_s \sim 1\%$) and should not have an appreciable effect. Similarly, the probability of two subsequent desired scattering processes within one pulse P_s^2 is also very low as $p_s \ll 1$. As discussed above, standalone undesired events are not detected and the pulse delay is typically chosen such that the mechanical mode can fully re-thermalize . As such, two neighboring pulses from do not affect each other. Throughout the rest of this work, we will use the photon counting techniques introduced in this section. In the following, we will consider GHz-optomechanics in the context of quantum transduction between signals in the microwave and optical telecom domains.

1.5. Optomechanical quantum transduction

While there are several avenues for optomechanical transduction between microwave and optical signals [27, 28], throughout this work, we will consider one specific conversion process. In this process, we connect three modes with two interactions. Each mode has a characteristic frequency ($\omega_e, \omega_m, \omega_o$) and decay rate ($\kappa_e, \Gamma, \kappa_o$). Here we restrict ourselves to a situation where ω_e and ω_m are equal and the interaction between them is resonant. We consider conversion from the microwave to the optical domain. First, a microwave tone loads an excitation into the mechanical mode. Subsequently, we can read out the state of the mechanical resonator by using the beamsplitter interaction (see

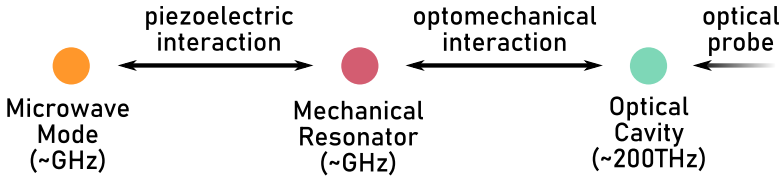

Fig. 1.4 | Schematic of the Conversion Process On the two extreme ends, the conversion process links a microwave mode (left, orange) at a few GHz and an optical mode at telecom wavelengths (right, green). The mediation between the two is realized by using a GHz-frequency mechanical resonator. The coupling between the mechanical and the microwave mode is realized by piezoelectric coupling and made possible by fabricating the device from a piezoelectric material. The optomechanical coupling, on the other hand, is realized by the radiation pressure force through the moving boundary and photoelastic effects.

1.14) to swap it onto the anti-Stokes field. Schematically, this is shown in fig. 1.4. Both interactions are characterized by a cooperativity, which is defined as

$$C = \frac{4g^2}{\kappa^{(i)}\Gamma}, \tag{1.15}$$

where g^2 is the coupling rate, $\kappa^{(i)}$ the decay rate of the microwave or optical resonators, and Γ the decay rate of the mechanical resonator. The cooperativity relates the coupling between modes to their decay rates and affects the transfer-efficiency of excitations between the two modes. Generally, the desirable regime for any transducer is one of high efficiency and low added noise. However, if the application for this transducer is the conversion of single excitations, the added noise should be as low as possible, because even one noise photon will already result in a signal-to-noise (SNR) with a lower bound of one. In the following, we will discuss the efficiency and added noise in an optomechanical transducer under continuous operation, following reference [29]. Further, discuss a measurement protocol which is in line with the measurement schemes from section 1.4. Finally, we will outline potential avenues towards meeting the requirements for quantum transduction.

1.5.1. Conversion Efficiency

The efficiency for the entire conversion process is given by

$$\eta = \eta_e \eta_o \frac{4C_{EM}C_{OM}\mathcal{L}_+^2}{\left[1 + C_{EM} + C_{OM}\left(\mathcal{L}_+^2 - \mathcal{L}_-^2\right)\right]^2}, \tag{1.16}$$

where η_e and η_o are efficiencies of transferring an excitation into the microwave- and out of the optical mode. These coupling efficiencies are given by $\eta_i = \kappa_{i,ext}/(\kappa_{i,ext} + \kappa_{i,int})$, where $\kappa_{i,ext}$ and $\kappa_{i,int}$ are the external and intrinsic loss rates of the microwave or optical cavities. In eq. 1.16 C_{EM} and C_{OM} are the electro- and optomechanical cooperativities, and $\mathcal{L}_+^2$ and $\mathcal{L}_-^2$ the sideband amplitudes of

the optical cavity [29]. The sideband amplitudes $\mathcal{L}_{\pm}^2$ are given by

$$\mathcal{L}_{\pm}^2 = \frac{(\kappa_o/2)\hat{}2}{(\kappa_o/2)^2 + (\Delta \pm \omega_m)^2}, \tag{1.17}$$

where $\Delta = \omega_{laser} - \omega_o$ is the detuning of the drive laser from the optical cavity. Further, $\mathcal{L}_{+}^2$ $(\mathcal{L}_{-}^2)$ corresponds to desired (undesired) scattering events in sec. 1.4. In our conversion scheme, where the drive laser is always red-detuned from the optical cavity such that $\Delta = -\omega_m$, $\mathcal{L}_{+}^2$ becomes unity. Assuming a fixed optomechanical cooperativity, the efficiency reaches its maximum value for

$$C_{EM}^{opt} = 1 + C_{OM}\left(\mathcal{L}_{+}^2 - \mathcal{L}_{-}^2\right). \tag{1.18}$$

In the sideband resolved limit, where $\mathcal{L}_{-}^2$ vanishes, and with this condition for C_{EM}, the efficiency can be approximated to

$$\eta_{limit}^{opt} = \eta_e \eta_o \frac{C_{OM}}{1 + C_{OM}}. \tag{1.19}$$

It is easy to see that in this limit, increasing the optomechanical cooperativity is the way to increase the efficiency [29]. Reducing the decay rates of the optical and mechanical modes will help in this regard. While for an optimized device design, the optical cavity decay rate is rather fixed, the mechanical decay rate can be reduced by acoustic shielding [30]. Another way to improve the cooperativity is to address the optomechanical coupling rate $g = g_0\sqrt{\bar{n}_{cav}}$. While the value of g_0 is typically fixed, the intracavity photon number $\bar{n}_{cav}$ can be tuned with the power of the optical pump. However, this value typically has an upper bound. This bound is due to optical absorption of the pump light and is set by the desired thermal occupation of the mode.

1.5.2. Added Noise

The added noise N is the second important figure of merit. The primary contributions in our scheme are thermal noise and optical amplification noise, giving $N = N_{th} + N_{amp}$. Both the microwave and optical modes are assumed to be in their ground states. For the microwave mode, this can be achieved by operating in a dilution refrigerator and for the optical mode this is already the case at room temperature. As a result, there is no thermal noise arising from either of these modes. The mechanical mode, on the other hand, typically has a finite occupation due to the optical absorption, which does introduce noise into the system. The thermal noise contribution is given by

$$N = \frac{1}{\eta_e}\frac{n_{th}}{C_{EM}}, \tag{1.20}$$

where n_{th} is the thermal occupation of the mechanical mode. As the first term has a lower bound of one, the second term becomes crucial in keeping the added noise at bay. The quantity $\frac{C_{EM}}{n_{th}}$ is also called the electromechanical

quantum cooperativity, which gives the ratio of the coherent coupling rate to the thermal decoherence. In the limit of an electronic noise temperature below n_{th}, a large electromechanical cooperativity effectively cools the mechanical mode. To this end is desirable to have quantum cooperativities greater than one, as well as a small thermal occupation of the mode in order to realize a small added thermal noise figure.
The optical amplification noise is due to accidental driving of the Stokes scattering process as the result of imperfect sideband resolution (sec. 1.4), followed by readout using the anti-Stokes process. This noise term is given by

$$N_{\text{amp}} = \frac{1}{\eta_o}\frac{C_{OM}\mathcal{L}_-^2}{C_{EM}}. \tag{1.21}$$

So far, our discussion describes a continuous conversion process. While this is a valid measurement scheme, it is not entirely aligned with the pulsed optical readout presented in Section 1.4. To this end, we will now introduce and disccuss a pulsed conversion scheme and point out the key differences.

1.5.3. Pulsed Conversion

The conversion protocol we invision for the devices presented in this work relies on pulsed excitation of the mechanical mode from the microwave domain, as well as pulsed optical readout. This modification means that, by separating the excitation and readout pulses in the time domain, we can consider the electro- and optomechanical interactions to be more independent than in the above case. Effectively, this enables us to turn the cooperativities on and off at different times. In our protocol, we send a sufficently long microwave pulse to excite the mechanical mode (red curve in fig. 1.5). In the case of a square RF-pulse, the mode-occupation n_{mech} increases while the RF-pulse is on and eventually reaches a steady state (blue curve in fig. 1.5). At this point, we send a readout pulse (yellow curve in fig. 1.5) which with a certain probability reads out the mechanical resonator (solid blue curve). In the event that the readout is unsuccessful, the occupation of the mechanical mode decays back to its initial value (dashed curve). We then wait for a time $t = \tau_{\text{duty}} > \tau_{\text{mech}}$ before we re-start the sequence such that the system is fully re-initialized. In this scheme, the mechanical mode serves as a short-time storage of the state and, as such, needs to be read out before one mechanical lifetime has elapsed.

Opting for a pulsed conversion protocol comes with one key requirement: The arrival time of a microwave pulse needs to be known to within the mechanical lifetime. While this is not a problem for experiments aiming to characterize a converter, it potentially limits the use of such a device to specific use-cases.

On the other hand, the pulsed protocol allows us to reduce noise contributions. The thermal noise (eq 1.20) will likely be reduced because operating the electro-opto-mechanical converter in a pulsed fashion suppresses absorption-induced heating, and thus reduces n_{th}. Further, the amplification noise (eq. 1.21) corresponds to the driving of the undesired scattering process, described

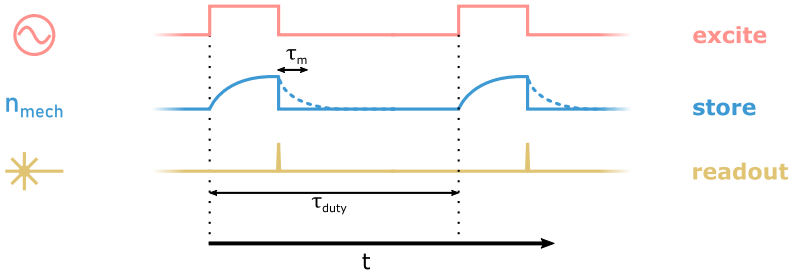

Fig. 1.5 | Pulsed Conversion Protocol We start by sending a sufficiently long, square microwave pulse in order to excite the device (top). During this microwave pulse, the phonon population of the mechanical mode, n_{mech}, (middle) steadily increases and eventually reaches a steady state population. After the microwave pulse is turned off, n_{th} starts to decay with the lifetime of the mechanical mode τ_m (dashed blue curve). At the onset of this mechanical decay, we send an optical readout pulse ($\omega_{laser} = \omega_c - \omega_m$, bottom) to the device. This readout pulse will then, with a probability p_s result in a scattering event, which de-excites the mechanical mode (solid blue line) and returns a scattered photon at ω_c. In the case that no scattering event occurs, the mechanical mode population decays naturally (dashed blue line). We then wait for the mechanical mode to fully relax back to its initial state before the next repetition of this sequence τ_{duty} after the start of the previous one.

in sec. 1.4. This term is greatly suppressed by using a pulsed protocol as subsequent iterations of the sequence (separated by τ_{duty} in fig. 1.5) do not affect each other. As such, only if an accidental excitation of the mechanical mode, followed by a readout, occurs within one optical pulse, does the amplification noise provide a contribution to the overall noise. Due to the typically small scattering probabilities, this double scattering is heavily suppressed in our type of conversion scheme.

Conclusion

In this chapter, we have outlined the basic principles of GHz-optomechanics, as well as the motivation to use them for microwave-to-optics conversion. We have also introduced a measurement scheme which is used throughout this thesis. Finally, we have introduced some background on the relevant figures of merit for wavelength conversion using GHz-frequency optomechanics. In this work, we focus on the use of III/V semiconductors as a material platform for electro-opto-mechanics. In Chapter 2, we discuss the motivation of using these materials as well as their relevant properties. We also discuss the fabrication of electro-opto-mechanical devices and important considerations to make when developing certain processes. In Chapter 3, we use a wavelength conversion device made from gallium arsenide to demonstrate microwave-to-optics conversion with a ground-state mechanical mode. We also evaluate gallium arsenide as a material platform as well as our device design. In Chapter 4, we explore gallium phosphide as a new material system for optomechanics and evaluate it particularly in contrast to our previous results from Chapter 3. In Chapter 5,

we then combine what we have learned from the previous chapters and design a new type of electro-opto-mechanical resonator with an extended mechanical mode in order to be realize engineerable interactions between well-defined modes. Finally, in Chapter 6 we will evaluate this work as a whole and draw conclusions about the approaches we used, as well as provide an outlook on potential other approaches.

2

The Role of Materials

Optomechanics is often hailed as a field that is largely independent of material-intrinsic resonances. This is in part true for micro- and nanopatterned devices which make use of photonic and/or phononic bandgaps. On paper, a suitable material only needs to be a dielectric with a refractive index larger than that of its surroundings and to be transparent for light of a desired wavelength. In practice, the ease of fabrication as well as optical absorption also impact the suitability of a material. Particularly for cryogenic experiments operating near the motional ground state of the mechanical mode, the surfaces of the material play a critical role. In order to utilize integrated optomechanical cavities for frequency conversion, the mechanical mode needs an electrical interface. This can be realized either through parametric, capacitive coupling [27, 28] to a low-frequency mode or by resonant coupling [14–17, 21, 31, 32] between a microwave drive and a GHz-frequency mechanical mode in a piezoelectric electro-opto-mechanical system. In this work we will focus on the latter approach. To this end, we will first discuss the implications of using a piezoelectrically active dielectric for an electro-opto-mechanical converter. Then, we will discuss suitable materials for integrated normal- and superconducting electrodes, followed by a discussion of how the material choices affect the fabrication workflow.

2.1. Piezoelectrics and Optomechanical Devices for Wavelength Conversion

There are several material properties that affect the optomechanical interaction strength g_{OM}. The property that most directly influences this interaction strength is the refractive index **n**, which affects both the photoelastic and moving boundary contributions. Another important criterion is the transparency window of the material. In this work we will focus primarily on materials which are relevant to the telecom band. In this particular wavelength range, silicon (Si) and gallium arsenide (GaAs) are very established materials which exhibit large refractive indices of 3.47 and 3.39 respectively. While silicon has been used for many landmark experiments in the field of cavity optomechanics [9–12, 33, 34], it lacks a piezoelectric moment which is desirable for electronic access to the mechanical mode. Throughout this work we will look at gallium arsenide and gallium phosphide (GaP) as materials for integrated microwave-to-optics converters. The two materials share the same general crystal structure with the only differences stemming from the second basis atom (As,P). Both materials are weakly piezoelectric with the relevant piezoelectric strain coefficients $e_{14,GaAs}$=-0.16 and $e_{14,GaP}$=-0.1. The bigger difference between the two lies in the band structure, particular when considering the interaction with telecom-wavelength photons. GaAs exhibits a direct bandgap at 1.42 eV (λ_g ~875 nm), which coincides with the two photon resonance in the optical telecom band. GaP on the other hand has an indirect bandgap of 2.26 eV (λ_g ~548 nm) and a direct bandgap of 2.78 eV (λ_g ~446 nm), which are both far beyond the two-photon resonance. The relevance of this difference in bandgap is highlighted by recent experiments in GaAs [16, 35], which were potentially limited by two-photon absorption induced heating. In the following we will look at these materials in the particular context of piezo-opto-mechanics. We will start by looking at the constraints that are imposed by the crystal symmetries, followed by a discussion of the fabrication of piezo-opto-mechanical devices.

2.1.1. Crystal Symmetries and Piezoelectricity in Zincblende Lattices

As we have restricted the discussion to semiconductors with zincblende lattices, we will start by reviewing the crystal symmetries and directions in such a lattice.

The zincblende crystal structure consists of two FCC (face-centered-cubic) sublattices (denoted A and B), which are offset relative to each other by (1/4,1/4,1/4)×a, where a is the lattice constant given by the edge length of the cubic unit cell. In Figure 2.1, these sublattices are shown in white (sublattice A) and grey (sublattice B), and represent the positions of the Ga-atoms and the As- or P- atoms, respectively. The cubic unit cell is surrounded by a red bounding box and has cubic symmetry. As such the axes which are parallel with the coordinate system are crystallographically equivalent and described as ⟨100⟩. The blue arrow denotes the ⟨110⟩ directions. While this group of materials is largely symmetric, the bonds between two basis atoms are aligned

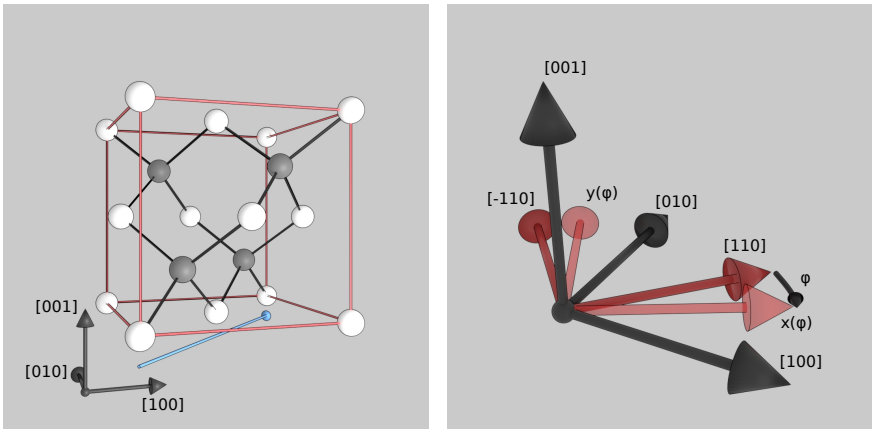

Fig. 2.1 | Zincblende Crystal Structure. left: Depicted is a cubic unit cell of a zincblende lattice. The axes of the coordinate system in the bottom left corner are aligned with the ⟨100⟩ directions. The white colored basis atoms in the A sublattice denote Ga atoms whereas the grey atoms in the B sublattice denote either Arsenic (As) or Phosphorus (P). The blue arrow indicates the ⟨110⟩ directions in the lattice. right: Illustration of the relevant rotated coordinate system. The axes bounding the cubic unit cell (see left part of this figure) are colored black. A set of axes with a 45° z-rotation is shown in solid red. This orientation is the most used one in this thesis. In eq.2.1, we define the piezoelectric tensor for [001]-oriented zincblende substrates for a coordinate system which is subjected from a further z-rotation by angle φ. This coordinate system is indicated by the axes $x(\varphi)$ and $y(\varphi)$.

with the ⟨111⟩ directions, which gives rise to anisotropic properties such as the piezoelectric effect and optical nonlinearities. The piezoelectric response of a material is given by its piezoelectric tensor. For the most common substrate orientation ⟨001⟩ and a zincblende crystal structure, the tensor in stress-charge form is given by:

$$e'_{jk}(\varphi) = \frac{e_{14}}{2}\begin{bmatrix} 0 & 0 & 0 & 2\alpha_2 & -2b_2 & 0 \\ 0 & 0 & 0 & 2b_2 & 2\alpha_2 & 0 \\ -b_2 & b_2 & 0 & 0 & 0 & 2\alpha_2 \end{bmatrix}, \tag{2.1}$$

where φ is the angle between the x-axis and the ⟨110⟩ direction, $\alpha_2 = sin(2\varphi)$ and $b_2 = cos(2\varphi)$ [36]. For GaAs and GaP, the values of e_{14} are -0.16C cm^{-2} and -0.1C cm^{-2} respectively. In Chapters 3 and 5 we consider two distinct types of piezoelectrically active mechanical modes: surface acoustic waves (SAWs) and longitudinal flexural modes. Both of these modes are accessible for φ=0, where the coordinate system $\{\hat{x},\hat{y},\hat{z}\}$ is aligned with $\{[110],[\bar{1}10],[001]\}$. To understand how the actuation of these modes works, it is useful to consider the electric potential which is produced by such modes. To this end, we have performed an eigenfrequency simulation on a rectangular block of GaAs in COMSOL. In fig. 2.2, we show the shape of two modes alongside the electric potential they produce on the top and bottom surfaces: a lamb wave (transverse out-of-plane) and a flexural longitudinal mode. The lamb wave (a) produces a λ_{sound}-periodic potential along the propagation direction, which means it can be

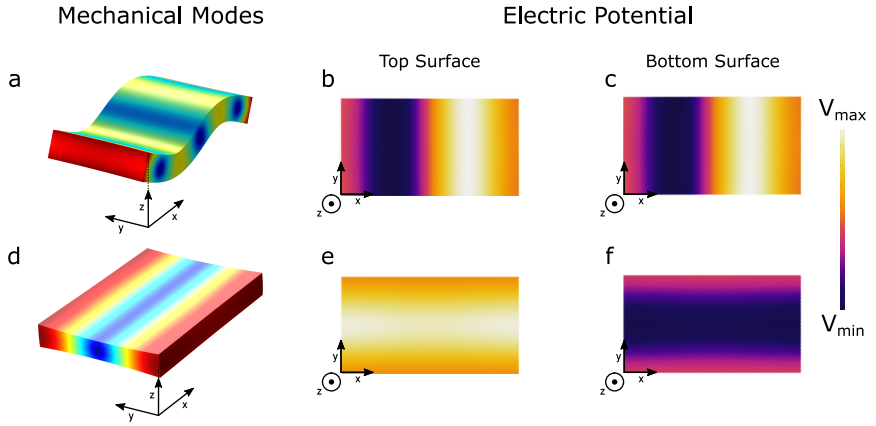

Fig. 2.2 | Two relevant piezoelectrically active modes and their electric potentials for $\varphi = 0$. a) A lamb wave (transverse, out-of plane) produces a $\lambda_{acoustic}$ periodic electrical potential on the top (b) and bottom (c) surfaces. A longitudinal flexural mode (d) produces an out-of-plane electric field (e,f).

detected or produced by an array of electrodes with alternating polarity, such as an interdigital transducer (IDT). Rayleigh, or surface acoustic waves (SAWs, as used in chap. 3) are relatives of the lamb wave which can be observed in films that are thicker than one acoustic wavelength. These waves are bound to one surface and produce a similar electric potential on the surface. As a result, they can be excited using the same electrode configuration. The flexural longitudinal mode (d), on the other hand, produces an out of plane electric field. Such a field can be produced and detected by top and bottom electrodes or by harnessing out-of-plane components of a field between a top electrode and a nearby ground plane. This mode will be discussed in greater detail in Chapter 5. In order to utilize these modes for wavelength conversion, we need to transfer the mechanical excitation into the nanobeam. This can be done by using a travelling surface-bound wave (SAW) which can be launched at the nanobeam from a nearby interdigital transducer (IDT), as is discussed in chapter 3, or by fabricating a piezoelectric resonator which is directly integrated with the nanobeam OMC, which will be discussed in chapter 5. Besides the material properties that are relevant for a final device, the material choice impacts the fabrication workflow. While this is true for devices fabricated from a single material, this impact is even more pronounced when materials are combined, for example as electrodes on a dielectric. As these are separate topics, we will discuss the fabrication for standalone integrated OMCs now and discuss these cross-effects in section 2.3.

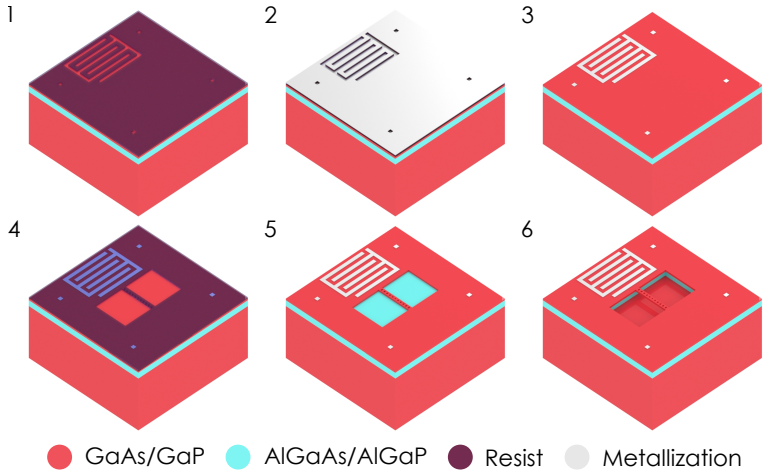

Fig. 2.3 | Fabrication Workflow 1: We start by spin-coating, exposing, and developing the mask for the metallization step. The mask here includes both the electrodes (an IDT is shown here) as well as a set of alignment markers. 2: We deposit metal on the mask. 3: After removing the remaining mask using a hot solvent, only electrodes and the markers remain. 4: We spin-coat the resist for the second step, perform an aligned exposure for the etch mask using the markers which were defined in steps 1-3, and develop the resist. 5: The etch mask is transferred to the device layer and the underlying sacrificial layer is exposed in the etched regions. 6: We perform an underetch and selectively remove a part of the sacrificial layer in the previously exposed areas. This step is also responsible for suspending the optomechanical crystal.

2.2. Fabrication of Integrated OMCs in Piezoelectric Materials

In this section, we will describe the workflow to fabricate integrated OMCs with optional electrodes starting from a layered source material consisting of a thin device layer, a sacrificial layer, all atop a thick substrate layer. In this work, we use material stacks consisting of (device layer-sacrificial layer-substrate) GaAs-$Al_{0.7}Ga_{0.3}As$-GaAs and GaP-$Al_{0.7}Ga_{0.3}P$-GaP. The fabrication of suspended optomechanical crystals generally relies on only one step of patterning. Due to the requirement for electrodes, here we employ an additional step to define the metallized areas. The entire fabrication workflow is shown in fig. 2.3. While the order of these steps is in principle arbitrary, here we choose to start with the metallization. For this step, we spin-coat a single layer of positive tone electron-beam resist on the sample and expose the pattern and a set of alignment markers using a direct-write electron beam lithography (EBL) system. After developing the resist, we deposit the metal followed by a lift-off step in an Anisole bath at 80°C where we remove the metal and resist from previously unexposed areas. During lift-off, placing the Anisole beaker in a sonicator results in additional agitation, which can help remove unwanted metal flakes from the chip. For the second lithography step, we again spin-coat the sample with positive tone electron beam resist. We use an automated marker search to align the etch-mask to our previously deposited markers. After

development, the pattern is transferred to the device layer by dry etching. For the samples in this work, the dry etching was carried out in a RIE system using a $N_2/BCl_3/Cl_2$ chemistry and a 1:2:1 ratio of the respective gasses. The exact parameters for GaAs and GaP are noted in chapters 3 and 4. It is important to note that the other parameters of the dry etching process are continuously subject to change in order to counteract drifts in the process. After dry etching, the resist is removed by immersion in N,N Dimethylformamide at 80°C. At this point we spin-coat a photoresist as a protective layer and use a dicing saw to cut the chip in order to expose the coupling waveguides to the nanobeam OMCs (not shown in fig.2.3). Following this, we remove the dicing resist. As a final step, we selectively remove the sacrificial layer in the vicinity of the OMC. In order to fabricate partially suspended structures, the sacrificial layer needs to be selectively removed without damaging the device layer on top. This is typically done by immersion in an inorganic solution which only etches away the sacrificial layer. In this work, we make use of semiconductor alloys where, in the sacrificial layer, the majority of the Ga-atoms are replaced by Al atoms. In our cases, this differentiates the sacrificial layer sufficiently from the device layer and thus lets us remove the sacrificial layer underneath. During this step, we use a 10% hydrofluoric acid (HF) for GaAs-based devices and a 10% ammonium fluoride (NH_4F, AF) solution for GaP-based devices. After this, the samples can be subjected to cleaning or digital etching steps to remove residues from the underetching [37]. As a final step, the samples are dried by either blow-drying with nitrogen or in a critical point dryer. Critical point drying in III/V samples can be particularly useful with fragile geometries which, due to the brittle nature of the material, might fracture during blow drying. As a disclaimer, we would like to add that for the fabrication of OMCs without any electrodes, the first lithography step, metallization, and lift-off can be omitted.

2.3. Metals for Electro-Opto-Mechanical Transducers

In the previous section, we have laid out a set of process steps to fabricate integrated OMCs with metal electrodes. However, thus far little attention was paid to the issue of which metals to choose. In this section, we aim to answer that question, taking into account the compatibility with the OMC fabrication process as well as deposition and suitable patterning techniques.

2.3.1. Choosing a Metal

Many metals do not survive inorganic treatments well. In the process outlined in section 2.2, the final underetching step makes use of hydrofluoric acid or ammonium fluoride. This step is absolutely necessary and any metal that we choose should survive it. Now that we have established this requirement, another important aspect to consider is whether or not the metal should be superconducting. Here we will first discuss normal conducting metals followed by a section about superconductors.

Normal Conducting Metals

For devices which can be tested at room temperature, a metal with a high conductivity at room temperature is beneficial. A popular choice here is gold, which is naturally unreactive and thus will withstand immersion in HF. However, gold does not generally adhere well to other surfaces, thus necessitating an adhesion layer. Typically titanium (Ti) is used, but due to its very reactive nature, it can be less suitable for inorganic treatments. A common alternative is chromium (Cr), which we use in chapter 3 in combination with a thin platinum (Pt) layer [17] .

Superconducting Metals

For a wavelength conversion device, any resistive losses will result in decreased efficiency. Thus, for devices operating at cryogenic temperatures, using superconducting metals is desirable if they are compatible with the fabrication process. As before, resistance to HF and AF are a necessity. Superconductors which fulfill this requirement are, among others niobium (Nb), niobium-titanium-nitride (NBTiN), and molybdenum-rhenium (MoRe), which we used in some of the work presented in this thesis. Importantly, aluminium (Al) is aggressively removed by both HF and AF and is thus unsuitable.

2.3.2. Choosing a Deposition and Patterning Process

In addition to the choice of which metal to use, the deposition and patterning strategies also have far reaching consequences. There are two predominant deposition methods: evaporation and sputtering.

Deposition Methods

While evaporation of metals can be a very directional process, it works less well for heavy metals as those tend to not melt as well from an electron beam. Sputtering, on the other hand, offers a lot of flexibility in terms of the material choice, but at the cost of the directionality of the deposition process.

Patterning Metal Films

In order to obtain a patterned metal film, there are two principal processes: deposition of metal on a patterned mask followed by lift-off and etching a pattern into a homogeneous film. The former option has the benefit of leaving the substrate surface intact. However, it tends to work best with evaporated films due to the directionality of the evaporation. Lift-off of sputtered films often results in so-called "dog ears", vertical fragments of the metal film along the edges of metallized areas. On the other hand, depositing a homogeneous metal film on the substrate avoids any issues concerning the directionality of the deposition technique. The film can then be patterned by dry etching using a mask. Unlike lift-off, this technique will attack the substrate in the regions where the metal is etched away, resulting in increased roughness. This could be problematic for photonic applications. Ultimately this is the reason we decided to use lift-off techniques with either evaporated Cr-Pt-Au metallizations (chapter 3) or lift-off with sputtered MoRe (chapter 5).

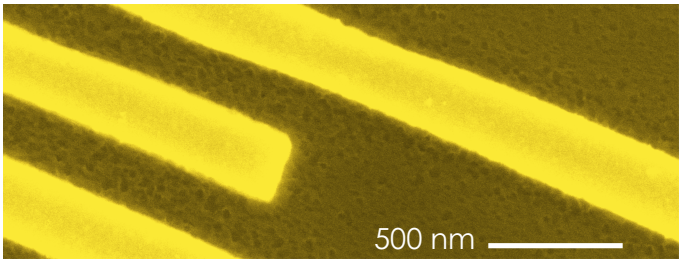

Fig. 2.4 | Scanning Electron Micrograph of Galvanic Corrosion of the GaAs Substrate. In this false-color image, the galvanic corrosion is manifested in the form of a crater-like landscape on the GaAs substrate. This effect is only observed in close proximity to the metal electrodes (bright yellow). The metallization in this case consists of a Cr-Pt-Au material stack.

2.4. Influence of Materials on Device Processing

In addition to predictable complications that arise from the addition of metal to a device, we have observed also a number of effects that only occur when metal is present, but do not affect the metal as such. To this end, this section serves as a reference for future work so that these effects don't need to be identified again.

1. **Galvanic Corrosion with Resist Strippers** When working with substrates with exposed metal, some organic resist removers can cause galvanic corrosion of the GaAs in the vicinity of exposed metal electrodes. During this work, this was observed while fabricating IDTs on GaAs substrates and using NMP (N-Methyl Pyrollidone) as a solvent during lift-off. The observed effect is shown in fig. 2.4, where the corrosion is visible as the formation of small crater-like features in the GaAs surface. This was reported in [38]. For our specific application (lift-off with AR-P 6200 resists), we were able to solve the problem by switching to anisole.

2. **Anisotropic Deformation of Holes During Cleaning Steps** During the fabrication of early GaAs nanobeam OMCs (without any metal) we employed a digital etching step after the final HF underetch in order to remove any residues from the underetch step (such as AlF). This digital etch consists of a 1min immersion in H_2O_2, 1min H_2O rinse, 2min 30% KOH, and a final H_2O rinse [37]. While this cleaning step works very well for samples without any metal, in the presence of metal we observed that the KOH step results in anisotropic etching of the photonic crystal holes in the GaAs. A side-by-side comparison of a normal sample and one with these anisotropic features is shown in fig. 2.5. Using step-by-step inspection, we identified the origin of this effect to be the KOH immersion. While investigating substitutes for KOH in the digital etching procedure, we also found that the same effect occurs when using NH_4OH. We found that, for the Cr-Pr-Au metallization, a solution of 7:1 BOE can be substituted for KOH without resulting in anisotropic etching. We would like to note that we did not observe the anisotropic etching with NH_4OH when using

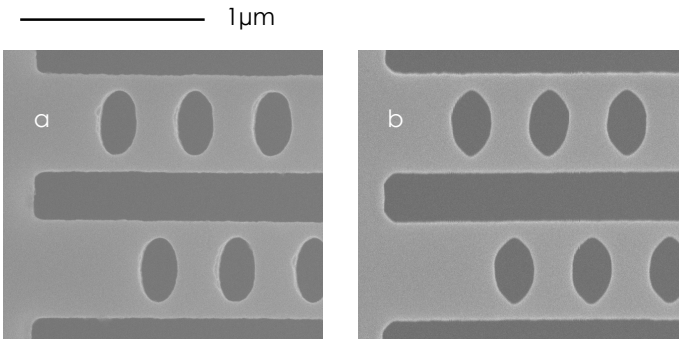

Fig. 2.5 | Normal Etching vs. Anisotropic Etching. Shown are scanning electron micrographs of a normal sample (a), where the holes retain their elliptical shape throughout the fabrication process and a sample which shows anisotropic etching of the holes (b). The anisotropic etching is most clearly visible in the sharp points at the vertices of the ellipse.

MoRe as the metallization.

Conclusion

Ultimately, materials provide a set of properties which form the baseline for property engineering. After careful consideration, we need to select one specific material or material platform, which means we need to accept the potentially undesirable properties that come with it. By understanding key aspects of our fabrication process we can determine fixed process steps. This enables us to keep other steps flexible in order to be able to adjust to potential unexpected cross-reactions.

3

Microwave-to-Optics Conversion Using a Mechanical Oscillator in its Quantum Groundstate

Moritz Forsch, Robert Stockill, Andreas Wallucks, Igor Marinković, and Simon Gröblacher

Conversion between signals in the microwave and optical domains is of great interest both for classical telecommunication, as well as for connecting future superconducting quantum computers into a global quantum network. For quantum applications, the conversion has to be both efficient, as well as operate in a regime of minimal added classical noise. While efficient conversion has been demonstrated using mechanical transducers, they have so far all operated with a substantial thermal noise background. Here, we overcome this limitation and demonstrate coherent conversion between GHz microwave signals and the optical telecom band with a thermal background of less than one phonon. We use an integrated, on-chip electro-opto-mechanical device that couples surface acoustic waves driven by a resonant microwave signal to an optomechanical crystal featuring a 2.7 GHz mechanical mode. We initialize the mechanical mode in its quantum groundstate, which allows us to perform the transduction process with minimal added thermal noise, while maintaining an optomechanical cooperativity >1, so that microwave photons

Parts of this chapter have been published in Nature Physics **16**,69-74 (2020)

mapped into the mechanical resonator are effectively upconverted to the optical domain. We further verify the preservation of the coherence of the microwave signal throughout the transduction process.

3.1. Introduction

Research into novel quantum technologies is receiving significant attention for its potential to fundamentally transform how we receive, process and transmit information. In particular, major endeavors into building quantum processors and quantum simulators are currently underway. Many leading efforts, including superconducting qubits [39] and quantum dots [40] share quantum information through photons in the microwave regime. While this allows for an impressive degree of quantum control [41], it also limits the distance the information can realistically travel before being lost [42]. At the same time, the field of optical quantum communication has already seen demonstrations over distance scales capable of providing real-world applications [43]. In particular, by transmitting information in the optical telecom band, fiber-based quantum networks over tens or even hundreds of kilometers can be envisaged [44]. In order to connect several quantum computing nodes over large distances into a quantum internet [3], it is therefore vital to be able to convert quantum information from the microwave to the optical domain, and back.

Several promising approaches have been taken to realize such a microwave to optics converter, most notably by trying to either directly couple the fields inside a non-linear crystal [45–48], by using rare earth ion doped crystals [49], magnons [50] or mechanical systems as a transducer [14, 51–56]. Recent milestones include bi-directional operation [15], coherent coupling [17], as well as efficient conversion [27], all of which make use of a mechanical oscillator as the transducer. While high conversion efficiency has been a particular success with some mechanically-mediated frequency converters, the demonstration of intrinsic noise sources compatible with conversion of a quantum state has remained an outstanding challenge. For quantum information protocols, particularly those that can tolerate optical loss, the requirement of subphoton added noise necessitates that the converter contains less than one thermal excitation [57]. To this end, several experiments have recently demonstrated cooling of mechanical oscillators into the quantum groundstate of motion [13, 58, 59]. The low thermal occupation forms the basis for quantum control over mechanical states, with demonstrations including quantum state preparation [5, 8, 9] and entanglement between multiple mechanical degrees of freedom [11, 60, 61]. Reaching this occupation regime is complicated by the absorption of optical photons, while at the same time realizing sufficiently strong optomechanical cooperativity to suppress additional noise sources [62]. To date there has been no demonstration of a system with mechanically-mediated interfaces in both microwave and optical domains that operates in the quantum ground state.

In this work, we demonstrate microwave-to-optics conversion with an electro-opto-mechanical device, which contributes less than one quantum of thermal

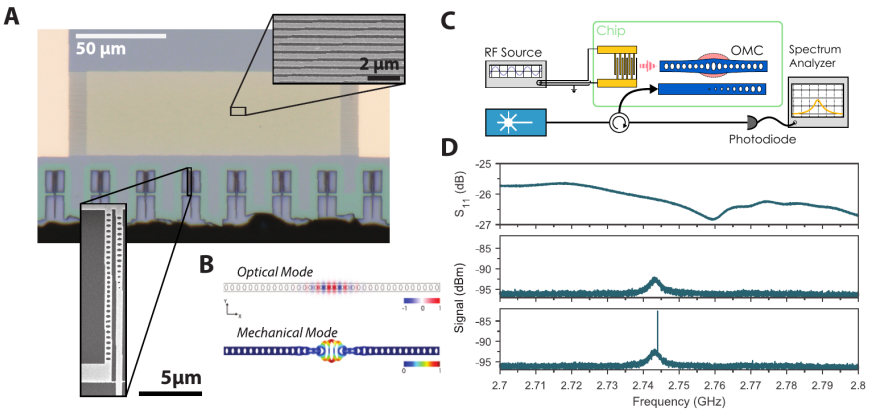

Fig. 3.1 | Device layout and room temperature characterization. (A) Microscope image of the transducer devices: Our structures are comprised of an interdigital transducer (IDT, in gold, cf. upper inset), which spans several optomechanical devices for ease of fabrication. The bottom side of the chip is directly accessible with a lensed fiber, allowing for optical access to the devices. The lower inset contains a scanning electron microscope image of an optomechanical resonator. The waveguide (right) is used for evanescently coupling light in and out of the device using the lensed fiber (accessed from the bottom, not shown). (B) Finite element simulations of the optomechanical device. The E_y component of the fundamental optical mode is shown (top) alongside the displacement field of the co-localized mechanical mode oscillating around 2.7 GHz (bottom). (C) Schematic of the room temperature characterization setup. A laser is used to address the device optically. The reflected light is then measured on a high-speed photodiode to resolve the noise spectrum around the mechanical frequency while an RF source is used to drive the IDT. (D) (Upper Panel) S_{11} reflection measurement of the IDT device with a resonance at 2.76 GHz. (Lower Panels) Optical measurements of the GHz-frequency noise of the reflected light with (bottom) and without (center) the RF drive tone applied to the IDT, which results in a narrow, coherent peak in the spectrum on top of the thermal peak. The laser in these measurements is blue-detuned from cavity resonance by the mechanical frequency, ω_m.

noise. We cryogenically cool a GHz frequency piezoelectric optomechanical crystal device into its quantum groundstate of motion and excite the mechanical mode using a microwave circuit through surface acoustic waves. Crucially, our system remains in the ground state while a drive of sufficient strength for upconversion from the mechanical to the optical domain is applied. This allows for conversion of a microwave pulse to the optical telecom band in a regime where we excite on average one phonon. As our converter features a noise source containing less than one photon, optimizing the electromechanical cooperativity [6, 8], the main efficiency bottleneck in our platform, will allow for the faithful transduction of a single photon from the microwave to optical domain.

3.2. Methods

Our microwave to optics converter consists of a one-dimensional optomechanical crystal (OMC) [23], which is mechanically coupled to an interdigital transducer (IDT) through surface acoustic waves (see Fig. 3.1A). We fabricate the devices from a 250-nm thick GaAs layer, on a 3-μm $Al_{0.7}Ga_{0.3}As$ sacrificial layer, both epitaxially grown on a GaAs substrate. This material combines a large refractive index ($n_{GaAs} = 3.37$ at $\lambda = 1550$ nm) [63] and a non-zero piezoelectric coefficient (ϵ_{14} =-0.16 Cm^{-2}), with well established fabrication processes. The optomechanical device, shown in the lower inset of Fig. 3.1A, is designed using finite-element modeling, such that the patterned nanobeam confines light in the telecom band, while at the same time exhibiting a co-localized mechanical breathing mode at $\omega_m = 2\pi \times 2.7$ GHz (Fig. 3.1B). The electro-mechanical coupling in our device is due to the piezoelectric effect that allows for the excitation of traveling acoustic waves which drive the OMC [17]. The opto-mechanial coupling, on the other hand, is facilitated by the parametric coupling between the mechanical excitation and the intracavity photon number owing to the combination of photoelastic coupling and moving boundary conditions [23]. Both effects can intrinsically operate in a bi-directional and noiseless fashion. The device fabrication consists of a two-stage lithography process to define the IDT and then pattern the nanobeams, followed by an HF etch to remove the AlGaAs sacrificial layer. A final deposition of 5 nm of AlO_x passivates the surfaces and reduces the effect of unwanted drive-laser absorption [26] (see Supplementary Information for details). The lower inset of Figure 3.1A displays a scanning electron microscope image of an optomechanical device, and an evanescently coupled waveguide which provides optical-fiber access to the confined optical mode [9].

We perform an initial characterization of the device properties at room temperature with the setup depicted in Figure 3.1C, the results of which are presented in Figure 3.1D. An S_{11} measurement of the IDT shows a 10 MHz-wide microwave resonance centered at 2.76 GHz. The mechanical mode of the OMC is then measured by locking a laser onto the blue sideband ($\omega_l = \omega_c + \omega_m$) of the optical cavity resonance ω_c ($\omega_c = 2\pi \times 194.3$ THz, with a loaded optical quality factor $Q_o = 3.3 \times 10^4$, see SI), and monitoring the

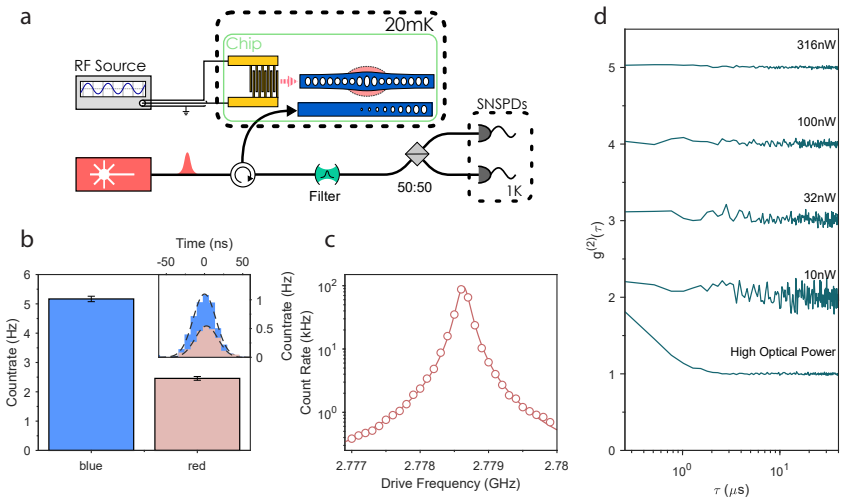

Fig. 3.2 | Device characterization at Millikelvin temperatures. (A) Schematic of the cryogenic experimental setup. The sample with the OMC and IDT, as well as a pair of superconducting nanowire single photon detectors (SNSPDs) are placed inside the dilution refrigerator (at 20 mK and ∼1 K, respectively). We lock the laser on the red sideband of our cavity and filter residual reflected pump light from the cavity, detecting photons scattered on the cavity resonance. (B) Sideband thermometry to extract the thermal occupation of the mechanical resonator. We find an occupancy $n_{\mathrm{th}} = 0.9 \pm 0.01$, confirming the initialization of the device close to its quantum groundstate. The bar graph shows the integrated counts for the red and blue sideband drives as well as the corresponding histograms (inset). Errors are one standard deviation, owing to the shot noise resulting from photon counting. (C) Mechanical characterization and initial RF to telecom-band conversion at mK temperatures. We sweep the RF drive frequency with the laser locked at $\omega_c - \omega_m$ and monitor the count rate. The solid curve is a Lorentzian fit to the data, from which we extract a mechanical linewidth of 197 kHz, corresponding to a mechanical lifetime of ∼0.8 μs. (D) Hanbury Brown and Twiss-type measurement of the photons emitted from our cavity with 7 nW of optical input power. The second order correlations $g^{(2)}(\tau)$ are shown for a selection of the measured RF powers alongside a reference measurement with no RF drive, but high optical power (4.5 μW, bottom curve). The curves are offset for clarity. The bunching in the reference measurement results from absorption heating due to the laser drive, yielding a large thermal state of the mechanical resonator.

high-frequency noise in the reflected signal. The peak in the noise spectrum at 2.744 GHz corresponds to the thermally-occupied mechanical mode ($\sim 1 \times 10^3$ phonons) and has a linewidth of several MHz. The small mismatch between the IDT and mechanical resonances of ∼10 MHz is a result of fabrication-based inhomogeneities. As we apply an RF tone to the IDT at the mechanical frequency ω_{m}, we observe an additional narrow peak on top of the thermal noise, corresponding to the transduced coherent signal from the IDT. The height of this peak is dependent on the RF power and the detuning from the mechanical resonance [17].

The room temperature characterization highlights that the large initial thermal occupation of the mechanical mode is a significant source of noise in this conversion process. Especially at low RF drive powers, the thermal noise dominates over the transduced signal [17]. By placing our device in a dilution

refrigerator (base temperature ~20 mK), we can in principle reduce the thermal occupation of the mechanical mode to $n_{th} \approx 10^{-3}$. In practice, the achievable occupation is limited by residual heating through laser absorption and finite thermalization to the cryostat [9]. With the device cooled to Millikelvin temperatures, we measure the actual thermal occupation of the mechanical mode by monitoring cavity-enhanced Stokes (blue sideband) and anti-Stokes (red sideband) scattering rates (Γ_B and Γ_R, respectively), when we drive the cavity with laser pulses detuned by $\pm\omega_m$ [59]. We suppress the reflected pump light through spectral filtering, such that only scattered photons on cavity resonance are detected by superconducting nanowire single-photon detectors (SNSPD) as shown in Figure 3.2A. Specifically, the rates we measure are set by $\Gamma_B \propto n_{th} + 1$ and $\Gamma_R \propto n_{th}$ [25]. Figure 3.2B shows the histogram of the single photon count rates measured for 40 ns long pulses set to the two detunings with a peak-power of 107 nW at the device. For this power, we find an optomechanical cooperativity of $C = 1.7$ (see SI) [64]. We extract a thermal occupation of $n_{th} = 0.90 \pm 0.01$, which verifies the initialization of the mechanical mode close to its quantum groundstate. This value is higher than the theoretical value set by the cryostat temperature, limited by residual heating of the structure during the laser pulse [9]. A sweep of the pulse power reveals that lower occupations can be achieved (e.g. $n_{th} = 0.36 \pm 0.03$, see SI), at the cost of a lower conversion efficiency.

3.3. Results

We now proceed to verify the conversion from microwave to optical telecom signals at Millikelvin temperatures. Red-detuned ($\omega_l = \omega_c - \omega_m$) optical pulses, which realize an opto-mechanical state-swap [65], are sent into the OMC to read out the state of the mechanical mode, which is coherently excited by sweeping the frequency of an RF drive tone (1 μW) across the mechanical resonance (see Fig. 3.2C). The data is fitted with a Lorentzian, from which we extract a mechanical linewidth of $\gamma_m/2\pi = 197$ kHz, an expected improvement in mechanical quality factor of about one order of magnitude compared to the value at room temperature. Furthermore, we observe a blueshift of both the mechanical mode and the IDT resonance by about 35 MHz compared to room temperature due to the temperature dependence of the GaAs elastic constants.

While the optical absorption can be reduced through tuning of the power of the input light as well as by pulsed operation, thus far little is known about the potential heating due to the RF tone which drives the IDT. In order to investigate the amount of heating resulting from the RF drive, we measure the second order correlation function $g^{(2)}(\tau) = \langle \hat{b}^\dagger(0)\hat{b}^\dagger(\tau)\hat{b}(0)\hat{b}(\tau)\rangle / (\langle \hat{b}^\dagger(0)\hat{b}(0)\rangle \langle \hat{b}^\dagger(\tau)\hat{b}(\tau)\rangle)$ of the mechanical resonator mode [9], by swapping mechanical excitations into optical photons at the cavity resonance frequency. Here $\hat{b}$ ($\hat{b}^\dagger$) is the annihilation (creation) operator of the mechanical mode. We expect the coherence of the RF drive to be mapped first onto the mechanical state in our resonator and then onto the light field. Any sign of heating due to the RF drive should result in bunching of the $g^{(2)}(\tau)$ during the mechanical lifetime (~1.5 μs). For

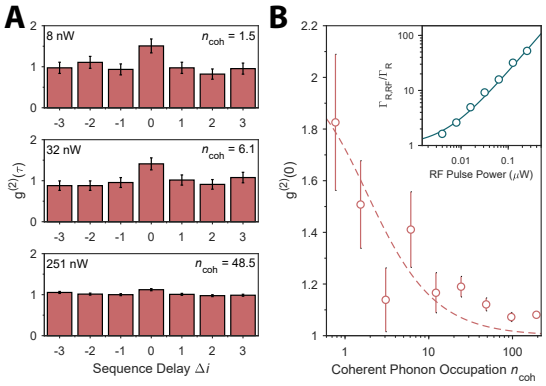

Fig. 3.3 | Correlation measurements of the microwave-to-optical transducer in the pulsed regime. (A) The transducer is operated such that RF drive pulses are upconverted to the optical domain using optical readout pulses. Shown are the correlations between coinciding detection events on the two single-photon detectors for photons emerging from the same $\Delta i = 0$ or different $\Delta i \neq 0$ pulse sequences. The panels correspond to various coherent phonon populations. (B) The full set of $g^{(2)}(0)$ values is shown as a function of RF power applied to the IDT. The dashed curve displays the expected value of $g^{(2)}(0)$ for a displaced thermal state with the corresponding extracted coherent phonon number n_{coh} (see SI). The inset shows the relative increase in the count rate as a function of RF power with a linear fit. We use this to extract the ratio of n_{coh}/n_{th}, which allows us to demonstrate the conversion at the single coherent phonon level for the lowest powers. We can see a clear transition from a bunched (low RF power) towards a not-bunched (high RF power) second order correlation. All error bars are one standard deviation.

this measurement, both the laser (locked onto the red sideband) and the RF source are operated in a continuous wave (CW) mode. The scattered optical photons are detected on a Hanbury Brown and Twiss (HBT)-type setup with two SNSPDs. The time τ here is the relative delay between clicks from the two detectors. We observe a near-flat $g^{(2)}(\tau)$ over the entire range of the RF power sweep (see Fig. 3.2D), clearly indicating that the coherent part of the mechanical state dominates any thermal contribution across the entire power sweep. As a reference, we also perform a measurement without an RF drive but with high enough optical power for absorption-induced heating to occur. In this case, a clear signature of photon bunching is visible, indicating, as expected, a thermal state of the mechanical resonator.

In order to demonstrate the potential of these devices as transducers of microwave to optical signals at the quantum level, we now operate both the RF driving and optical read-out in a pulsed mode [12]. We send a resonant RF pulse (1 μs long) to the IDT to excite our oscillator and access the mechanical state through a 40 ns long red-detuned state-swap pulse. This allows us to minimize the effects of heating due to optical absorption. The pulsed experiment enables us to quantify the absolute number of coherent phonons added to our initial state by comparing the scattering rate in the presence of an RF drive ($\Gamma_{R,RF}$) to the scattering rate we obtain from the remaining thermal population (Γ_R) (inset in Fig. 3.3B). By measuring the photon rate with and without a resonant RF drive, we recover an RF-phonon conversion effciency of

3.57×10^{-10} phonons per RF photon.

Using the same HBT-type setup as above, we detect the second order correlation of the scattered photons, which allows us to compare the coincidences between detection events originating from the same ($\Delta i = 0$) or different ($\Delta i \neq 0$) pulse sequences. A selection of the histograms of these correlations is shown in Figure 3.3A for various coherent phonon occupations (n_{coh}). The full set of $g^{(2)}(0)$ values for increasing coherent phonon occupation is shown in Figure 3.3B. We expect the value of $g^{(2)}(0)$ to be determined by the ratio n_{coh}/n_{th} (cf. the SI). We extract this number from the relative count rate we recover with and without the RF pulse, $\Gamma_{R,RF}/\Gamma_R$, displayed in the inset of Figure 3.3B, making use of $\Gamma_R \propto n$. The dashed curve in Figure 3.3B displays the expected $g^{(2)}(0)$ values for our RF power sweep based on the theory for a displaced thermal state (cf. the SI), which are in good agreement with our measured values. An increase in RF power results in a larger coherent displacement of the thermal state, which in turn leads to a decreased value for $g^{(2)}(0)$.

While our pulsed experiments clearly demonstrate conversion between a coherent state in the microwave and the telecom domain, they do not imply the retention of the input-state phase. In order to access the coherence of the transduction process, we use a modified version of the setup (for a detailed sketch see SI Fig. 3.9). We split the red-detuned excitation laser into two branches of a phase-stabilized Mach-Zehnder interferometer (MZI), one of which contains our device and the other an amplitude electro-optic modulator (EOM). We drive both the IDT and the EOM with a single RF source, such that a coherent transduction process results in a fixed phase relationship between the up-converted light in the two inteferometer arms. We then mix the light on a beamsplitter, matching the photon rate in the two arms. Figure 3.4A displays the count rate at one output port of the MZI when we vary the phase of the interferometer for several coherent phonon occupations. We observe a clear interference pattern with a visibility of $44\pm3\%$ for powers corresponding to a coherent phonon occupation of $n_{coh} = 1.1$, which increases to $85\pm7\%$ as the coherent contribution dominates over the small thermal background. Figure 3.4B displays these experimentally retrieved visibilities for several coherent phonon occupations, the expected modeled behavior assuming only thermal noise ($n_{noise} = n_{th}$, solid line), as well as additional incoherent noise sources ($n_{noise} = n_{th} + n_{other}$, dashed line). These respective trends are given by $\sqrt{n_{coh}/(n_{coh} + n_{noise})}$ and scaled by the maximally achievable interference visibility in our setup of 90%. Here, n_{other} represents the equivalent noise figure for any other source than the thermal occupation of the resonator, including imperfections in the measurement setup. We estimate the upper bound of these sources to be $n_{other} \sim 2.5$. The main contributions to this remaining part are drifts of the interferometer free spectral range over the duration of the measurement, imperfect sideband resolution ($(\kappa/4\omega_m)^2 = 0.27$), as well as mechanical decoherence [52, 57]. With this measurement, we confirm the phase-preserving nature of the conversion process down to the single phonon level.

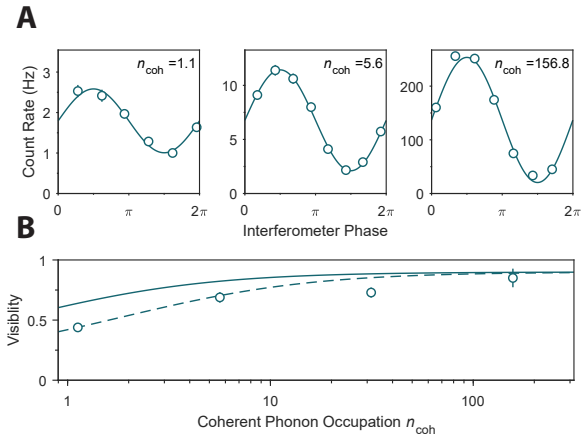

Fig. 3.4 | Preservation of phase coherence during transduction. (A) Interference patterns taken at different values of n_{coh}. The solid curves are sinusoidal fits to the data, from which we extract the visibility. (B) Visibility as a function of the coherent phonon occupation in the mechanical resonator. The error in the visibility for the lower values of n_{coh} is smaller than the data point size. The data is overlaid with the expected visibility from the coherent and noise contributions $\sqrt{n_{coh}/(n_{coh}+n_{noise})}$. The solid line considers thermal noise only ($n_{noise} = n_{th}$), while the dashed line also takes any other sources into account ($n_{noise} = n_{th} + n_{other}$), while both are scaled by the maximum available visibility in our setup. Error bars are one standard deviation.

3.4. Efficiency Considerations

The total efficiency of our device is the product of two parts: the loading efficiency of the mechanical mode from the microwave side (3.57×10^{-10}, measured from the attenuator output at at the mixing chamber to the excitation of phonons in the mechanical mode) and the optical readout efficiency of the mechanical mode 1.55×10^{-5}. The latter one can itself be separated into two parts: $\eta_{ro} = p_r \times \eta_{det}$, with $\eta_{det} = 1.41 \times 10^{-3}$ (see SI). The state swap probability $p_r = 1.1\%$ is a function of the power with which the optical readout is performed and can be increased through improvements with respect to optical absorption. Note that the current performance of our device is already sufficient to read out a non-classical state of the mechanical mode [9]. The low loading efficiency of the mechanical mode can be attributed to the design and size of the electromechanical transducer. We estimate the efficiency of transferring a SAW wave from the IDT (150 μm wide) into a single, narrow ($\sim$1 μm), suspended beam to be less than 2.5×10^{-5}. Additional contributions arise from the difference in the polarizations of the incoming SAW wave and the mechanical mode, the discrepancy between the IDT and mechanical frequencies, as well as the large electrical impedance of the IDT. These factors can be improved by tailoring the size and design of the electromechanical transducer specifically to the purpose of exciting the breathing mode of a single nanobeam [29]. While the small-scale piezo-resonator required to mode-match the nanobeam will necessitate careful electrical impedance matching,

the required network falls into the range accessible with coplanar resonator technology [29]. The relatively small optomechanical state-swap probability and detection efficiency reported here, on the other hand, can be circumvented with post-selection techniques routinely used in quantum optics experiments [9, 10].

3.5. Conclusion

We have demonstrated faithful conversion of a microwave to an optical signal with only a small added thermal contribution due to the groundstate occupation of the mechanical resonator. Furthermore, these measurements show our ability to detect the displacement amplitude of the initial state in our mechanical resonator down to one phonon, (corresponding to our lowest measured RF power), marking a crucial benchmark for applications in the quantum regime [57]. The device used for this experiment is a fully integrated, on-chip hybrid electro-opto-mechanical system with a mechanical mode as the transducer. We cool this mode to its quantum groundstate using a dilution refrigerator, which allows us to operate directly at the quantum noise limit. This work allows for the on-chip integration of a single-photon RF-source, such as a superconducting qubit [6, 7], which paves the way for building a true quantum network over large distances, based on superconducting nodes. The device we consider here is specifically suited towards heralded entanglement generation between remote superconducting qubits, a protocol which is described in Ref. [57].

While we demonstrate quantum limited noise performance in the readout of the mechanical state, the conversion efficiency is currently limited by low microwave-phonon excitation efficiency. We would like to note that this is not a fundamental limit but rather a result of design choices for this proof-of-principle demonstration. The material itself imposes some limitations on the efficiency, such as the remaining absorption heating and the relatively low piezoelectric coupling. However, demonstrations of coherent coupling between superconducting qubits and surface acoustic waves in GaAs [6, 7] suggest the latter are highly suitable choices for noise-free carriers of quantum information. Importantly, our system is already operating in the range of optical drive strengths expected for mediating efficient conversion. In particular, the optomechanical cooperativity of $C \approx 1.7$ (see SI) is sufficient for efficiently converting GHz phonons into telecom photons.

During the submission process we became aware of related work demonstrating GaAs optomechanical crystal in the low thermal occupation regime [35].

3.6. Supplementary Information

3.6.1. Device fabrication

The samples were fabricated on an epitaxial material stack consisting of a GaAs $\langle 100 \rangle$ substrate, a 3 μm thick sacrificial layer of $Al_{0.7}Ga_{0.3}As$, followed by a 250 nm thick device layer of GaAs. The devices are aligned with the $\langle 110 \rangle$ plane to allow propagation of the SAWs into the nanobeam. As a first step, the IDT structures, waveguides and alignment markers are defined

using electron beam lithography. A stack of 5 nm Cr, 15 nm Pt, and 30 nm Au [17] is then evaporated onto the chip, with any excess removed in a lift-off process. The coplanar waveguide is impedance matched to the 50Ω coaxial cables in the setup. The OMC pattern is then aligned to the IDT structure using the markers from the previous lithography step in the second electron beam lithography step. The pattern is transferred into the device layer using a reactive ion etch process in an Alcatel GIR-300 etcher using a $N_2/BCl_3/Cl_2$ chemistry. In order to remove all organic residues, a digital etching step is performed which consists of 1 min submersion in 37% H_2O_2, followed by thorough rinsing, 2 min submersion in 7:1 BOE, and a second round of thorough rinsing. Finally, the OMC structures are suspended by selectively removing the sacrificial layer using a 10% HF solution, which is followed by a second round of the digital etching to remove residue from the underetch process.

3.6.2. ALD passivation

First low temperature tests of our OMCs fabricated from bare GaAs resulted in devices that were very prone to absorption of laser pulses, with varying results for n_{th} of typically many thermal phonons. We attribute the variance between different devices to a variation in the native oxide layer. Previous research [26] has indicated that a thin layer of ALD deposited aluminium oxide can reduce these absorption effects in GaAs microdiscs. We therefore proceeded to strip the native oxide off the GaAs using 7:1 BOE, followed by a 5 nm deposition of ALD AlO_x at 300 °C. Using this method, we observe a reduction in the initial thermal occupation of our mechanical resonator from $n_{th} \sim 2 - 10$ to $n_{th} < 1$.

3.6.3. Optical characterization

Optical characterization of our device is done by measuring the reflected power as we scan a tunable laser across its resonance, which is shown Fig. 3.5. The loaded linewidth is $\kappa = 2\pi \times 5.8$ GHz, corresponding to a quality factor of about $Q_o = 3.3 \times 10^4$. Light is evanescently coupled from a central waveguide into the devices. The waveguide itself is tapered towards the edge of the chip (see Fig. 3.1), where we position a lensed fiber with a focal length of 14 μm. In order to calibrate the coupling efficiency from the fiber to this waveguide, we compare the off-resonant reflected power to the power reflected from a fiber mirror. This ratio gives η_{fc}^2, resulting in $\eta_{fc} = 33\%$. In addition, we determine our optomechanical coupling rate to be $g_0/2\pi = 1.3$ MHz [9], which for 0.5 μW optical power (intra-cavity photon number $n_c = 280$) results in a cooperativity of $C = \frac{4g_0^2 n_c}{\kappa \gamma_m} = 1.73$.

3.6.4. RF-Setup

In order to send the microwave tone into the cryostat to our device, we attenuate the signal by several dB at the respective temperature stages in the fridge. This serves to both thermalize the coaxial cable and to reduce the

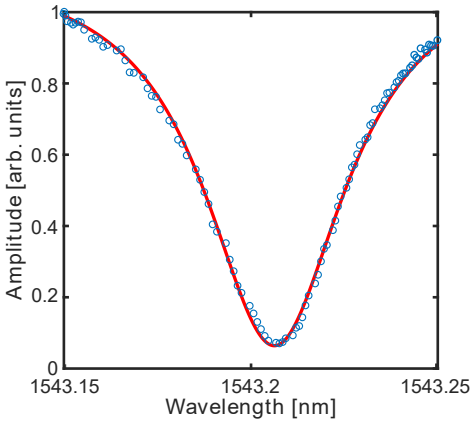

Fig. 3.5 | Scan of the optical resonance of the OMC, fitted with a Lorentzian (red solid line), which yields a linewidth of $\kappa = 2\pi \times 5.8$ GHz.

noise temperature of the signal seen by the device. The specific attenuation steps are shown in Fig. 3.6. The coaxial cables connecting the stages with a temperature of <1 K are made from aluminium and are thus superconducting when the cryostat is cold. In order to be able to perform the S_{11} measurement of our IDT device despite the strong attenuation of the input signal, we use two RF circulators at the bottom of the refrigerator. The first one connects to the device and the second one acts as an isolator sending any thermal noise coming from higher the temperature stages to the 50 Ω terminated 3^{rd} port of the circulator. The reflected signal from the device is then amplified using a cryogenic low-noise amplifier and sent back to the VNA. For the pulsed experiments, we use an RF source which replaces the VNA at the input of the cryostat. To generate these pulses, we send the signal through an RF switch, which is gated using a pulse generator.

3.6.5. Efficiency calibration

The calibration of the overall efficiency consists of two steps. The first part concerns the RF to phonon conversion efficiency. We send 1 μs-long RF pulses into the dilution refrigerator at a nominal power of -14 dBm, which results in, on average, 1 added coherent phonon to the resonator. Combined with the 39 dB of attenuation of the coaxial line inside the cryostat, this means we have around 2.8×10^9 RF photons on the input of the device for every phonon in the resonator. This low efficiency is mostly due to the IDT not being optimized for a single OMC device, but rather being 160 μm wide, which corresponds to about 300 times the width of a single nanobeam device. Furthermore, the structure is not designed to be impedance matched to the OMC, which leads to reflections and additional losses.

We calibrate the total efficiency of our setup by sending a few-photon off-resonant laser pulse to the device. This gives the product: $\eta_{tot} = \eta_{fc}^2 \times \eta_{trans} \times \eta_{QE}$,

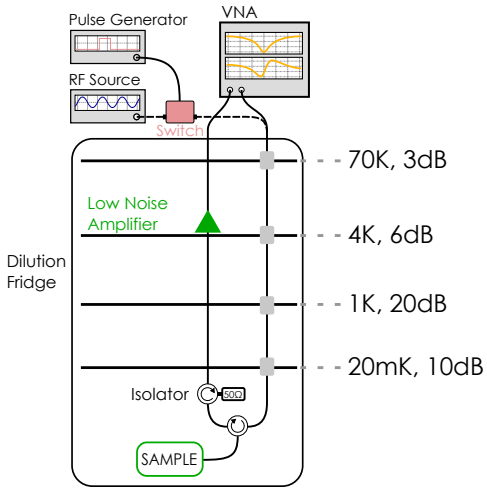

Fig. 3.6 I Schematic of the RF measurement setup. We used a vector network analyzer (VNA) to measure a reflection spectrum of our device. The signal is attenuated on the input line to reduce the noise temperature seen at the lower temperature stages and to thermalize the coaxial cable. We use a circulator to redirect the signal reflected from our device into the unattenuated output line. We use a second circulator to send any high temperature noise coming from the other stages onto a 50 Ω termination. The output signal is amplified at the 4 K stage using a low-noise amplifier. For the pulsed experiments, we used an RF source instead of the VNA and we gate the signal using an RF switch and a pulse generator.

where η_{fc} is the fiber coupling efficiency, η_{trans} the transmission efficiency of the detection path (filter cavities, fiber components, etc.) , and η_{QE} the quantum efficiency of the detectors. We measure this total efficiency to be 8.43×10^{-4}. In addition we determine the coupling between the center waveguide and the nanobeam cavity, $\eta_{\mathrm{dev}} = \kappa_e/\kappa$, to be 0.65. With the previously determined fiber-coupling efficiency of 0.33, we get a total detection efficiency $\eta_{\mathrm{det}} = \eta_{\mathrm{fc}} \times \eta_{\mathrm{dev}} \times \eta_{\mathrm{trans}} \times \eta_{\mathrm{QE}} = \eta_{\mathrm{tot}} \times \eta_{\mathrm{dev}}/\eta_{\mathrm{fc}} = 1.41 \times 10^{-3}$. We estimate the state readout probability (using a red-detuned pulse) to be $p_{\mathrm{r}} = 1.1\%$. Within the 80 ns window considered in the correlation measurements, we find a total detector dark count rate for both detectors of 0.5 Hz.

3.6.6. Sideband asymmetry

At the 20 mK base temperature of the dilution refrigerator, we predict a thermal population of the mechanical mode of around 10^{-3} phonons. The occupation is increased, however by absorption of the laser pulses required to convert the microwave-frequency signal to the optical domain. Owing to this effect, we operate at an elevated occupation of $\sim$0.9 phonons for the pulsed experiments presented in the main text. Notably, the heating occurs on a rapid timescale. Absorption heating is also an important limitation for the operation of coherent opto-mechanical devices fabricated from silicon, however the slower internal dynamics compared to GaAs allow for multiple operations before the mode temperature is raised [59].

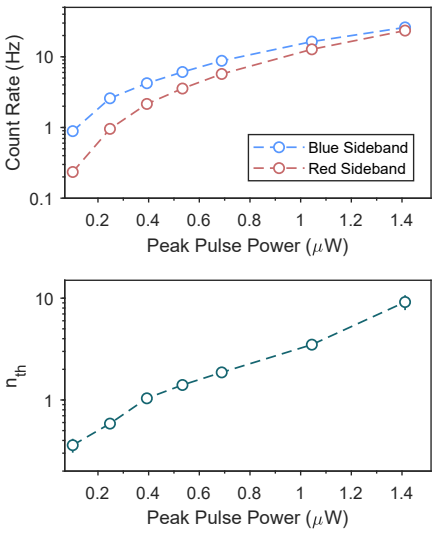

Fig. 3.7 | Sideband asymmetry for varying optical pulse powers. Upper panel: Count-rates for Stokes (anti-Stokes) scattering from the blue (red) cavity sideband. Lower panel: Extracted thermal population of the mechanical mode. Error bars showing one standard deviation are obscured by the data points. The curves in the two panels are empirical power-law fits to the data. This dataset was an early measurement of our device, recorded at slightly different settings than the measurement shown in Fig. 3.2b, which explains the small discrepancy in the thermal occupation.

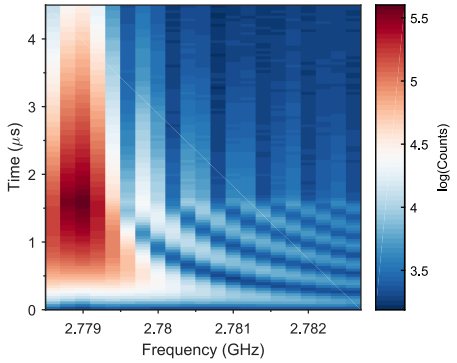

Fig. 3.8 | Time-correlated detected optical signal for continous optical driving under a detuned 1.5 μs-long microwave-frequency pulse.

In order to further illustrate the effect of absorption induced heating on our optomechanical devices, Figure 3.7 displays additional sideband asymmetry measurements taken for 40 ns long Gaussian pulses with different peak powers. The upper panel displays the count rates from driving the blue and red mechanical sidebands of the optical resonance, while the lower panel displays the extracted thermal population of the mechanical resonator. Notably, for a peak power of 0.1 μW, we extract a mechanical occupation of only 0.36 ± 0.03 phonons. While operating at this power would ensure coherent transduction of even lower power microwave pulses, it also reduces the associated conversion efficiency further and increases the total measurement time beyond reasonable time scales.

3.6.7. IDT - Mechanics detuning

In Fig. 3.2c of the main text, we plot the mechanical resonance of the optomechanical device, which we access by monitoring the rate of anti-Stokes scattering as we vary the frequency of the coherent RF drive. This measurement can be supported by the dynamics of the mechanical mode, which we present in Fig. 3.8. For this measurement we continuously drive the red-sideband of the optical resonance at low power, and pulse the IDT with a 1.5 μs-long tone, such that we continuously record the occupation of the mechanical mode. The figure displays the count-rate we record correlated to the pulse arrival time for a variety of microwave-pulse detunings from the mechanical resonance. The detuning-dependent oscillatory signal we measure during the pulse is the transient response of the mechanical oscillator to the detuned surface-acoustic wave. After the end of the pulse at 1.5 μs, the mechanical resonance continuously decays to the thermal background level.

3.6.8. Displaced thermal states

In the main text we have used a displaced thermal state model to fit our data (cf. Fig. 3.3). Here we briefly derive the second order correlation function for such a state. We start with an initial thermal occupancy n_{th} of our mechanics and displace it coherently with an amplitude $\sqrt{n_{\mathrm{coh}}}$. Thus, our resulting mode occupation is given by

$$\langle \hat{n} \rangle = n_{\mathrm{coh}} + n_{\mathrm{th}}. \tag{3.1}$$

To derive the expected $g^{(2)}(0)$ values for a given ratio of $n_{\mathrm{coh}}/n_{\mathrm{th}}$, we follow [66] and start with the general expression for $g^{(2)}(0)$:

$$g^{(2)}(0) = \frac{\langle \hat{\alpha}^\dagger \hat{\alpha}^\dagger \hat{\alpha} \hat{\alpha} \rangle}{\langle \hat{\alpha}^\dagger \hat{\alpha} \rangle^2} = \frac{\langle \hat{\alpha}^\dagger \hat{\alpha} \hat{\alpha} \hat{\alpha}^\dagger \hat{\alpha} \rangle - \langle \hat{\alpha}^\dagger \hat{\alpha} \rangle}{\langle \hat{\alpha}^\dagger \hat{\alpha} \rangle^2}, \tag{3.2}$$

where $\hat{\alpha}$ and $\hat{\alpha}^\dagger$ are annihilation and creation operators,respectively, and we used the commutation relation $[\hat{\alpha}, \hat{\alpha}^\dagger] = 1$. Substituting $\hat{\alpha}^\dagger \hat{\alpha} = n$ and $\sigma^2 = \langle \hat{n}^2 \rangle - \langle \hat{n} \rangle^2$, we can simplify this to

$$g^{(2)}(0) = \frac{\langle \hat{n}^2 \rangle - \langle \hat{n} \rangle}{\langle \hat{n} \rangle^2} = 1 + \frac{\sigma^2 - \langle \hat{n} \rangle}{\langle \hat{n} \rangle^2}. \tag{3.3}$$

For a purely thermal state, this results in

$$g^{(2)}_{\mathrm{th}}(0) = 2 = 1 + \frac{\sigma^2_{\mathrm{th}} - n_{\mathrm{th}}}{n^2_{\mathrm{th}}} \rightarrow \sigma^2_{\mathrm{th}} = n^2_{\mathrm{th}} + n_{\mathrm{th}}. \tag{3.4}$$

Using $\sigma^2 = \sigma^2_{\mathrm{th}} + n_{\mathrm{coh}}(1 + n_{\mathrm{th}})$ [66] and substituting it in Eq. (3.3), we get

$$g^{(2)}(0) = 1 + \frac{\sigma^2_{\mathrm{th}} + n_{\mathrm{coh}}(1 + 2n_{\mathrm{th}}) - \langle \hat{n} \rangle}{\langle \hat{n} \rangle^2}. \tag{3.5}$$

Substituting σ^2_{th} from Eq. (3.4), $\langle \hat{n} \rangle$ from Eq. (3.1) and simplifying yields

$$g^{(2)}(0) = 2 - \frac{n^2_{\mathrm{coh}}}{(n_{\mathrm{th}} + n_{\mathrm{coh}})^2} = 2 - \frac{1}{\left(\frac{n_{\mathrm{th}}}{n_{\mathrm{coh}}} + 1\right)^2}. \tag{3.6}$$

This result is also consistent with the one obtained by Marian et al. [67]. We directly extract the ratio $\frac{n_{\mathrm{coh}}}{n_{\mathrm{th}}}$ from $\Gamma_{\mathrm{R,RF}}/\Gamma_{\mathrm{R}} = (n_{\mathrm{coh}} + n_{\mathrm{th}})/n_{\mathrm{th}}$, where Γ_{R} is the count rate resulting from a red-detuned pulse alone and $\Gamma_{\mathrm{R,RF}}$ is the count rate resulting from a red-detuned pulse, which is overlapped with the RF drive pulse, displayed in the inset of Figure 3.3b in the main text.

3.6.9. Phase Sensitive Detection Setup

In order to confirm the coherence of the transduction process from our RF source all the way to the telecom-band photons, we use an interferometer

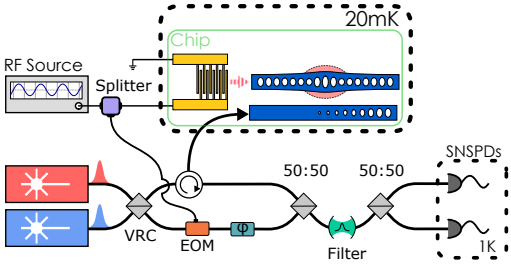

Fig. 3.9 | Phase sensitive measurement setup. We lock one laser (red) on the red sideband and the other (blue) far off resonance and split them into the two interferometer arms using a variable coupler (VRC). One RF source is used to drive both the device and the electro-optical modulator (EOM). The EOM creates sidebands on the red-detuned laser pulse, while at the same time providing a well defined phase with respect to the IDT RF drive tone. The off-resonant laser is only used to stabilize the interferometer.

with our device in one arm and an electro-optic modulator (EOM) in the other (cf. Fig. 3.9). By driving both the IDT and the EOM with the same RF source, we generate optical sidebands of the drives in both interferometer arms with a well defined phase. This allows us to verify the coherence of the transduction process by measuring the interference between the two signals. We use a strong second, far detuned laser pulse (blue in Fig. 3.9) to stabilize the interferometer. This locking-drive is reflected from the photonic crystal mirror in the waveguide without resulting in intracavity photons and is delayed from the red measurement tone. The stabilization is done by measuring the transmission of this strong laser pulse at both outputs of the interferometer and feeding back the signal to a fiber stretcher (φ in the figure). We change the interferometer phase for the red (and the upconverted) light by sweeping the frequency of the locking laser over the free spectral range (approx. 20 GHz) of the interferometer. Both lasers, as well as other sidebands which are not resonant with the cavity, are filtered out before the SNSPDs.

4

Gallium Phosphide as a piezoelectric platform for quantum optomechanics

Robert Stockill, Moritz Forsch, and Simon Gröblacher

Recent years have seen extraordinary progress in creating quantum states of mechanical oscillators, leading to great interest in potential applications for such systems in both fundamental as well as applied quantum science. One example is the use of these devices as transducers between otherwise disparate quantum systems. In this regard, a promising approach is to build integrated piezoelectric optomechanical devices, that are then coupled to microwave circuits. Optical absorption, low quality factors and other challenges have up to now prevented operation in the quantum regime, however. Here, we design and characterize such a piezoelectric optomechanical device fabricated from gallium phosphide in which a 2.9 GHz mechanical mode is coupled to a high quality factor optical resonator in the telecom band. The large electronic bandgap and the resulting low optical absorption of this new material, on par with devices fabricated from silicon, allows us to demonstrate quantum behavior of the structure. This not only opens the way for realizing noise-free quantum transduction between microwaves and optics, but in principle also from various color centers with optical transitions in the near visible to the telecom band.

Parts of this chapter have been published in Phys. Rev. Lett. **123** 163602 (2019)

4.1. Introduction

The interaction of light and mechanical motion in nanofabricated resonators provides a flexible interface between telecom photons and long-lived phononic modes. Rapid progress in this field has resulted in the realization of nonclassical states of light and motion at the single photon and phonon level [9–12], demonstrating the suitability of these structures as quantum light-matter interfaces. One particularly interesting application for which these interfaces could provide their unique functionality is the transduction of quantum information between different carriers. To this end, piezoelectric materials are of great interest, as the electromechanical coupling in principle allows for transduction of a quantum state between the microwave and optical frequency domains [14, 16, 17]. Additionally, wide-bandgap materials make simultaneous coupling to both visible wavelength light (at which many optically-active quantum systems operate) and the low-loss telecom bands in the near-infrared possible [64, 68]. One of the main challenges to realize such a quantum transducer is the ability to faithfully exchange excitations between optical and mechanical modes, which requires any stray absorption of light to be minimal in order not to introduce thermal noise.

A particularly interesting class of optomechanical resonators for quantum interfaces are formed from the simultaneous confinement of light and mechanical motion in periodically patterned nanobeams [69]. These devices feature high frequency (few GHz) mechanical modes, such that the resolved sideband regime is accessible with reasonable optical resonator quality factors ($\gtrsim 2 \cdot 10^4$), while the mechanical mode can be initialized to the quantum groundstate by cryogenic cooling. The low mass of the mechanical mode and small optical cavity mode volume allow for strong optomechanical coupling and the monolithic design facilitates on-chip integration with other quantum systems. While optomechanical crystals have been fabricated out of materials such as GaAs [16, 17, 35], GaP [19, 70], $LiNbO_3$ [21], SiN [22] AlN [14, 15] and diamond [20], amongst others, to date nonclassical optomechanical interaction in such structures has been limited to silicon-based devices.

4.2. Methods

In this work we realize an optomechanical crystal (OMC) in gallium phosphide (GaP) featuring high cooperativity interaction between an optical resonance at 1550 nm and a mechanical breathing mode close to 3 GHz. Due to the minimal absorption of GaP at these wavelengths, cooling our device to 7 mK allows us to operate deep in the mechanical quantum groundstate with mode occupations of as little as 0.04 phonons. Furthermore, we demonstrate quantum behavior of our device by measuring nonclassical correlations between photons and phonons [12]. Our results validate that the device performs at a similar level to comparable designs in Si [9–11, 13], while far surpassing current achievements in GaAs or other piezoelectric materials [16, 35]. Owing to the wide electronic bandgap and piezoelectric properties of GaP the successful operation of our device in this parameter regime opens the door

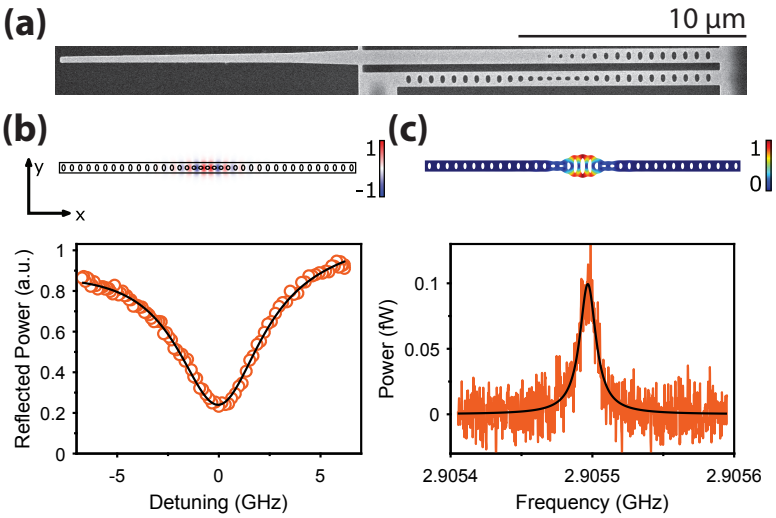

Fig. 4.1 | a Scanning electron micrograph of the optomechanical crystal (bottom) with a coupling waveguide (top). **b** Normalized E_y component of the simulated optical mode (top) and corresponding reflection spectrum of the fabricated device (bottom). The solid black curve is a lorentzian fit to the data, including a linear offset to account for changing laser power. The over-coupled linewidth of the optical resonance is $\kappa = 2\pi \times 5.14$ GHz. **c** Normalized displacement of the simulated mechanical mode (top) and power spectral density of the mode at ~7mK (bottom). The solid black curve is a lorentzian fit to the data. The linewidth of the resonance is $\gamma_m = 2\pi \times 13.8$ kHz.

for novel quantum experiments as well as the potential for using such devices for microwave-to-optics conversion. Strong optical $\chi^{(2)}$ and $\chi^{(3)}$ non-linear coefficients [71, 72] and the ability to integrate GaP with current silicon technologies [70] makes this material a unique platform for quantum experiments and technologies.

Our device consists of an optomechanical crystal evanescently coupled to an optical waveguide, as shown in Fig. 4.1(a). We fabricate the device from a 200 nm thick layer of GaP, on a 1 μm $Al_{0.64}Ga_{0.36}P$ sacrificial layer, both epitaxially grown on a GaP substrate. The material features a large refractive index $n_{GaP} = 3.05$ at $\lambda = 1550$ nm [73] as well as a piezoelectric response $\epsilon_{14} = -0.1$ Cm^{-2} [74]. The optomechanical device is designed to exhibit an optical mode in the telecom band ($\lambda \sim 1560$ nm) as well as a co-localized mechanical mode at $\omega_m \sim 2\pi \times 2.85$ GHz. The simulated mode profiles are shown in Fig. 4.1(b) and (c). The optomechanical coupling between these modes is realized through the photoelastic effect and the moving boundary conditions due to the shape of the mechanical mode [75]. Simulations of these contributions, with photoelastic coefficients from reference [76], predict a single photon optomechanical coupling strength $g_0 = 2\pi \times 525$ kHz.

We place our sample inside a dilution refrigerator at a base temperature of ~7 mK. Optical access to the device is provided by lensed fiber coupling to the evanescantly coupled reflective waveguide (see Fig. 4.1(a)). The initial characterization is performed by scanning a tunable laser across the optical

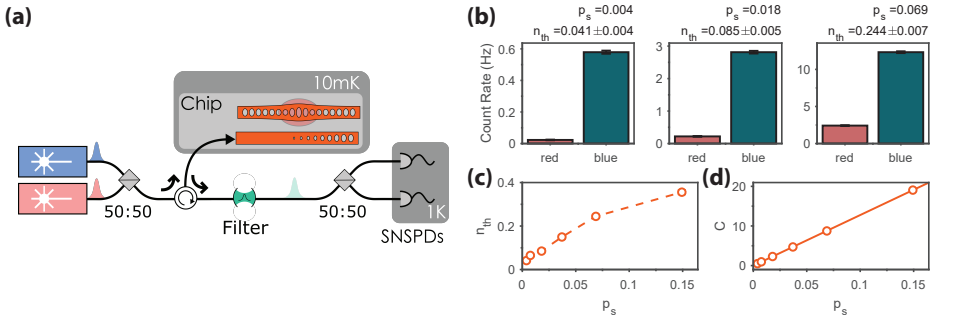

Fig. 4.2 | Device characterization at Millikelvin temperatures. **a** Schematic of the measurement setup. We excite or read out our device using a laser on either the red or blue sideband, resulting in cavity-resonant scattered photons. We then filter out the residual pump light and detect the scattered photons on single photon detectors (SNSPDs). **b** Sideband thermometry measurements taken at varying optical powers (corresponding to different scattering probabilities). The bars represent integrated counts over the duration of the pulse and the error bars correspond to one standard deviation. **c** Extracted thermal occupations from the sideband thermometry measurement. In this panel, the errorbars are smaller than the corresponding data points. **d** Extracted values of the cooperativity C as a function of the scattering probability. The line is a linear fit to the data.

4

resonance at $\omega_c = 2\pi \times 194.8$ THz, shown in Fig. 4.1(b). The mechanical resonance at $\omega_m = 2\pi \times 2.905$ GHz is obtained by monitoring GHz-frequency noise in the reflected light, when stabilizing the laser a few GHz blue-detuned from the optical resonance, shown in Fig. 4.1(c). We extract optical and mechanical linewidths of $\kappa = 2\pi \times 5.14$ GHz (loaded Q-factor of 3.79×10^4) and $\gamma_m = 2\pi \times 13.8$ kHz, respectively (cf. Fig. 4.1(b,c)). The optical resonator is over-coupled to the nearby waveguide 4.5.2, such that we extract an intrinsic linewidth of $2\pi \times 1.31$ GHz (intrinsic Q-factor of 1.49×10^5).

4.3. Results

While the cryogenic cooling of the device should initialize the mechanical mode in its quantum groundstate, previous research [16, 35] has indicated that, owing to optical absorption, the measured thermal occupation can be significantly higher [62]. We therefore experimentally determine the absorption-limited mode temperature using sideband thermometry [25, 77]. In order to limit the effects of absorption-induced heating, we send 40 ns long optical pulses to our device, spaced by 160 μs. During this measurement, we stabilize our drive laser to either the blue ($\omega_l = \omega_c + \omega_m$) or red ($\omega_l = \omega_c - \omega_m$) sideband of the optomechanical cavity. The blue (red) pulses realize a two-mode squeezing (state-swap) interaction, which creates (annihilates) an excitation of the mechanical mode and produces a scattered photon on resonance with the optical cavity. We then filter out the reflected pump light and use superconducting nanowire single photon detectors (SNSPDs) to measure the photons on cavity resonance. The corresponding setup is shown in Fig. 4.2(a). In the weak excitation limit, the photon rates resulting from the blue (Γ_b) and red (Γ_r) sideband drives are proportional to $p_s(n_{th} + 1)$ and $p_s n_{th}$, respectively. Here, p_s is the

optical power-dependent scattering probability [12] (see SI for details). This measurement allows us to extract the thermal occupation of the mechanical mode, n_{th}, using the ratio $n_{th} = \Gamma_r/(\Gamma_b - \Gamma_r)$. By performing this measurement at several optical powers, we can assess the thermal mechanical occupation due to quasi-instantaneous heating from the optical drive, which forms the baseline for further experiments. A selection of photon count rates is shown in Fig. 4.2(b) and the full set of extracted thermal occupations is shown in Fig. 4.2(c) as a function of p_s. The measured thermal occupations are as low as $n_{th} = 0.041 \pm 0.004$, a significant improvement over the lowest reported thermal occupations in other III/V-based optomechanical devices [16, 35]. From the asymmetry measurements, we extract the single-photon optomechanical coupling strength, $g_0 = 2\pi \times 845 \pm 34$ kHz. We attribute the discrepancy between the simulated and measured values of g_0 to our imperfect knowledge of the photoelastic coefficients of GaP, as well as small fabrication-related differences between the designed and actual devices. The power-dependent optomechanical cooperativity, $C \equiv 4g^2/\kappa\gamma_m$, with $g = \sqrt{n_c}g_0$ and n_c being the intra-cavity photon number, is shown in Fig. 4.2(d). Operating at the highest cooperativities comes at the cost of a raised thermal occupation. However, cooperativities $C \gg 1$ are achievable while remaining well below $n_{th} = 1$. In particular, C exceeds 1 for a low occupation of $n_{th} < 0.1$, an important benchmark for the conversion of quantum states [64].

The parameter regime in which our device operates is similar to recent demonstrations of nonclassical behavior in silicon optomechanical resonators [9–12]. In these optomechanical devices delayed heating of the mechanical mode is a major challenge for quantum experiments [16]. In order to study the presence of similar effects in our current system, we investigate the heating dynamics by sending two consecutive red detuned pulses to the device. The first pulse provides a source of heating to the thermalized device. The second pulse then converts any thermal phonons at an elevated occupation into photons, resulting in an increased scattering rate ($\Gamma_r \propto n_{th}$). By varying the delay between the two pulses, we can access the time dynamics of the heating process. The measured mode occupations are shown in Fig. 4.3(a) for three different scattering probabilities. To gain insight into the heating dynamics, the occupations are fitted with a phenomenological biexponential function ($n_{th}(\tau) = A \cdot e^{-\tau/\tau_{decay}} \cdot (1 - e^{-\tau/\tau_{rise}}) + n_{th,i}$). We extract the characteristic decay constant, τ_{decay} for the mechanical mode to be 22 ± 1 μs, in reasonable agreement with the Q-factor extracted from the linewidth of the mechanical mode shown in Fig. 4.1(c). For these scattering probabilities, we recover a heating time for the mode τ_{rise}, between 150 and 180 ns.

In order to investigate the suitability of GaP as a piezolectric material platform for quantum optomechanics, we use a pulsing scheme from the DLCZ protocol [12, 78]. It consists of a weak blue-detuned pulse, which excites the mechanical mode with a small probability and returns a scattered photon on resonance with the cavity. A subsequent red-detuned pulse swaps the state of the mechanical mode onto the light field and again produces a cavity-resonant scattered photon. Just as before, both the excitation and readout pulse are

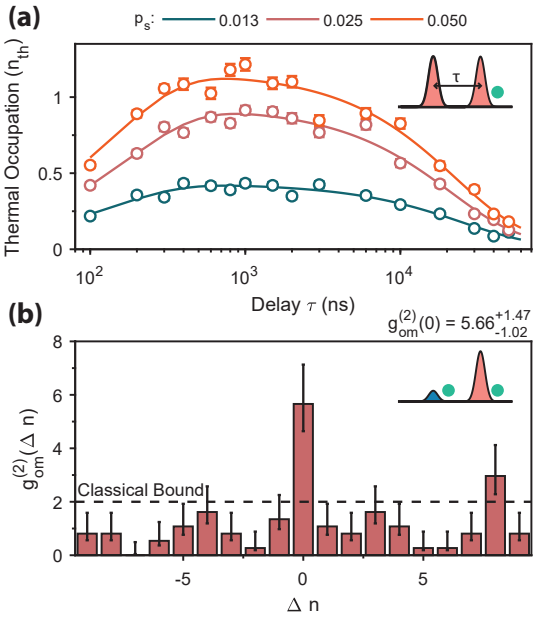

Fig. 4.3 | a Heating dynamics of a GaP optomechanical crystal. The data points display the measured occupation of the mechanical mode following an initial red-detuned state swap pulse, which results in scattering probabilities of 0.013, 0.025 and 0.050. The occupation is inferred from the count rate of a second red-detuned pulse, delayed by time τ, as displayed in the inset schematic. The solid curves are phenomenological two-exponential fit to the data, accounting for the delayed onset of thermal excitation and the relaxation time of the mechanical mode. **b** Correlations between state-projecting and state readout photons. The displayed two-photon correlations are calculated by normalizing to the single photon rates during the blue-(red-)detuned write (state-swap) pulse. The errorbars represent 68% confidence intervals.

40 ns long. Based on the characteristic heating time, τ_{rise}, we choose the time delay between our excitation and readout pulses to be 150 ns. As such, we read out the state of the mechanical mode before the delayed heating of the mode adds excess thermal population. Given the small probability of exciting the device, detection of a scattered photon from the weak blue-detuned pulse heralds the creation of a nonclassical mechanical excitation of the resonator, consisting predominantly of a single phonon [9]. The correlation of the projection photon and the remaining phonon (accessed through the red-detuned state-swap pulse) can then be determined through the statistics of the detected photons during many repetitions of the sequence. We operate at scattering probabilities for the write and read pulses of $p_{\text{s,write}} \sim 0.06\%$ (corresponding to 25 nW peak power) and $p_{\text{s,read}} \sim 2\%$ (750 nW), respectively, to limit the parasitic heating, and set the repetition rate to be 25 kHz, such that the mechanical mode can fully re-thermalize between each sequence. More details on the experimental parameters can be found in section 4.5.1.

We analyze the second order correlation $g^{(2)}_{\text{om}}(\Delta n) = P(W \cap R, \Delta n)/(P(W) \times P(R))$ between detector clicks originating from write (W) and read (R) pulses from the same ($\Delta n = 0$) or different ($\Delta n \neq 0$) pulse sequences. Here, $P(W \cap R, \Delta n)$ is the probability of detecting a read photon Δn sequences after a write photon, while $P(W)$ and $P(R)$ are the independent detection probabilities of write- and read photons. The measured correlation values are displayed in Fig. 4.3(b). We observe a correlation of $g^{(2)}_{\text{om}} = 5.66^{+1.51}_{-0.98}$ for read and write pulses from the same sequence, and confirm that detection events from different sequences are on-average uncorrelated. The uncertainty in our measured correlation value is a 68% confidence interval determined from the likelihood function of rare two-photon coincident events occurring. The high levels of bunching are a clear signature of nonclassical phonon-photon correlations in this system. The correlations we measure here are limited by three sources – the presence of residual incoherent heating in the device from both the write and read pulses, dark-counts in the SNSPDs (0.08 Hz, $\sim 1/5$ of the write pulse clicks), which are important during the low-probability write pulse, and the imperfect filtering of the drive laser in the detection setup. In order to limit the effect of readout-induced heating and detector dark-counts, we consider events occurring in the first 50% of the read pulse, and the central 50 ns of the write pulse, respectively. Small improvements to our optomechanical device and setup will hence allow to realize more complex single phonon experiments [9, 11].

Based on the optomechanical performance shown in this report and the piezoelectric properties of GaP [74], it is pertinent to consider how the device presented here could be adapted for the conversion of quantum states between the microwave and optical domains. This could be achieved by supplementing the nanobeam with a mechanically coupled, resonant piezoelectric actuator [29]. Faithful conversion of a quantum state requires that less than one photon of noise is added throughout such a conversion process. At the same time, efficient conversion requires that the cooperativity of the electrome-

chanical interface must be much greater than 1 and closely matched to the optomechanical cooperativity [64]. As a result of the low optical absorption in GaP observed in our measurements, for an optomechanical cooperativity above 10 (see Fig. 4.2(c)-(d)), a matched electromechanical interface could result in an added noise figure of only 0.02 photons owing to incoherent heating of the device and imperfect sideband resolution [57].

Maintaining a large optomechanical coupling strength requires for the piezoelectric resonator to have a similar mass to the 280 fg mechanical mode studied here. Considering the piezoelectric tensor of GaP and the alignment of the nanobeam to the [110] crystal orientation, the appropriate breathing mode could then be actuated through a vertical electric field. A generic resonator of matched mass and frequency can be formed by designing a 950 nm wide and 580 nm long beam between superconducting electrodes in a parallel-plate capacitor configuration [14]. This idea is further discussed in section 4.5.5 The resulting interface is expected to convert electrical and mechanical energy with a coupling coefficient $k^2_{\text{eff}} \approx 0.017\%$. Assuming a mechanical loss rate equal to our nanobeam, and taking pessimistic values for on-chip parasitic capacitance of $\sim$100 fF, an electromechanical cooperativity of 20 could be achieved by the addition of a microwave-resonator with a Q-factor of as little as $\sim$150. While further investigations of microwave losses in GaP are required, the devices presented here, together with the recently developed GaP-on-Silicon platform [72] offer robust materials systems for incorporation of low-loss coplanar microwave circuitry.

4.4. Conclusion

We have demonstrated nonclassical behavior of an optomechanical crystal fabricated from gallium phosphide. Our device can be operated deep in the quantum groundstate with significantly reduced heating compared to similar devices fabricated from GaAs and other piezoelectric materials. GaP combines several unique properties, such as a large electronic bandgap, high refractive index, and a significant piezoelectric response, making it extremely well-suited for many novel applications for optomechanical quantum systems. Combined with the piezoelectric properties of GaP, our demonstration of nonclassical optomechanical interaction will enable microwave-to-optics converters to operate in a previously unreached regime. In addition, the large bandgap could allow for coupling of photons to quantum systems which natively operate in the visible spectrum. Our system can further be used for non-linear optics experiments [71, 79] owing to the strong optical $\chi^{(2)}$ and $\chi^{(3)}$ non-linearities and the large index contrast between the suspended device and vacuum, potentially even allowing to increase the optomechanical coupling rate into the strong-coupling regime [80].

4.5. Supplementary Information

4.5.1. Device fabrication

The samples were fabricated from an epitaxial structure grown by MOCVD on a GaP ⟨100⟩ substrate, consisting of a 1 μm thick sacrificial layer of $Al_{0.64}Ga_{0.36}P$, followed by a 200 nm thick device layer of GaP. The growth was performed in a Veeco Turbodisc D180 reactor under hydrogen as carrier gas, trimethylgallium and trimethylaluminum as organometallic precursors and under phosphine at a reactor pressure of 70 Torr. The OMC pattern is first defined in a ∼200 nm thick layer of AR-P 6200-13 resist using a Raith 5000+ direct-write electron beam writer. The pattern is then transferred into the device layer using a reactive ion etch process in an Alcatel GIR-300 etcher using a $N_2/BCl_3/Cl_2$ chemistry. The remaining resist is removed in a 80°C bath of N-N Dimethyl Formamide (DMF). The OMC structures are suspended by selectively removing the sacrificial layer using a 10% Ammonium Fluoride (NH_4F) solution. To avoid stiction between the devices and the substrate layer, we use critical point drying as a final step before a 5 nm thin film of AlO_x is deposited using atomic layer deposition (ALD) in order to passivate the surface.

4.5.2. OMC-Waveguide coupling

In order to couple light into our optical cavity, we use a coupling waveguide in close proximity to the OMC. The evanescent field of this waveguide overlaps with the optical mode of the cavity and thus, by setting the distance between the two, we can set the external coupling (decay) rate. The cavity decay rate is $\kappa = \kappa_i + \kappa_e$, where κ_i is the intrinsic (cold cavity) and κ_e is the external decay rate. The efficiency of coupling light into or out of the optical cavity is then given by $\eta_{dev} = \kappa_e/\kappa$. For a single-sided optical cavity, this efficiency cannot simply be extracted from a reflection spectrum because for a given depth of the cavity dip two solutions exist for η_{dev}, where one corresponds to an over-(under-)coupled cavity with $\eta_{dev,over} > 0.5$ ($\eta_{dev,under} < 0.5$). In order to determine whether our device is over- or under-coupled, we employ a technique from [81], where we stabilize our laser far detuned from the optical cavity and generate sidebands on this carrier using an EOM. We sweep the sideband across the resonance by driving the EOM with a vector network analyzer (VNA) and monitoring the reflected signal at the driving frequency using a high-frequency photodiode. From the resulting amplitude and phase responses, we determine our device to be over-coupled, with $\eta_{dev} = 0.75$.

This strong over-coupling results in our device being imperfectly sideband resolved $(\kappa/4\omega_m)^2 = 0.196 < 1$. For the present measurement, this does not pose any restrictions, however, as we are not operating in the bad cavity limit either. In particular, when driving at $\omega_l = \omega_c \pm \omega_m$ the optomechanically generated sidebands at $\omega_c \pm 2\omega_m$ are suppressed by 7.8 dB compared to the tone that is resonant with the cavity (at ω_c). In addition, we filter the light leaving the OMC using tuneable Fabry-Pérot cavities with a bandwidth of 40 MHz, allowing us to further suppress signals that are off-resonant from the

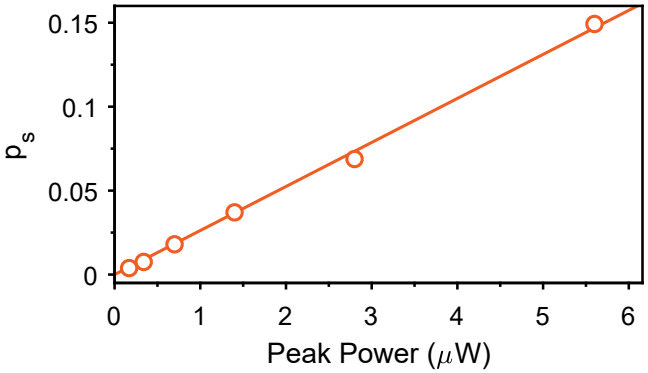

Fig. 4.4 I Calibration of scattering probability p_s from input peak power, for 40-ns long pulses. The line is a linear fit to the data. The power that reaches the device is attenuated by the 55% fiber coupling efficiency. Data set as used for Fig. 4.2 in the main text.

optical cavity.

4.5.3. Scattering probabilities

The scattering probability p_s in our experiment describes the probability of either exciting (blue sideband) or reading out (red sideband) the mechanical mode. We retrieve this probability from the measured count rates (Γ_r and Γ_b, respectively) and our calibrated detection efficiency η_{det}

$$\Gamma_r = p_{s,read} \cdot n_{th} \cdot \eta_{det}, \tag{4.1}$$

$$\Gamma_b = p_{s,write} \cdot (n_{th} + 1) \cdot \eta_{det}, \tag{4.2}$$

where, in the weak coupling limit ($g \ll \kappa$), $p_{s,r}$ and $p_{s,b}$ are given by

$$p_{s,r} = 1 - \exp\left(\frac{-4\eta_{dev} g_0^2 E_p}{\hbar\omega_c\left(\omega_m^2 + (\kappa/2)^2\right)}\right), \tag{4.3}$$

$$p_{s,b} = \exp\left(\frac{4\eta_{dev} g_0^2 E_p}{\hbar\omega_c\left(\omega_m^2 + (\kappa/2)^2\right)}\right) - 1. \tag{4.4}$$

Here, E_p is the total energy of the incident laser pulse [9]. In the limit of small scattering probability, where $p_{s,read/write} \ll 1$, the two values converge to

$$p_s \approx \frac{4\eta_{dev} g_0^2 E_p}{\hbar\omega_c\left(\omega_m^2 + (\kappa/2)^2\right)}. \tag{4.5}$$

Calibration of the detection efficiency η_{det} using an attenuated laser pulse reveals a value of $\eta_{det} = 0.023$. This value includes the efficiency between

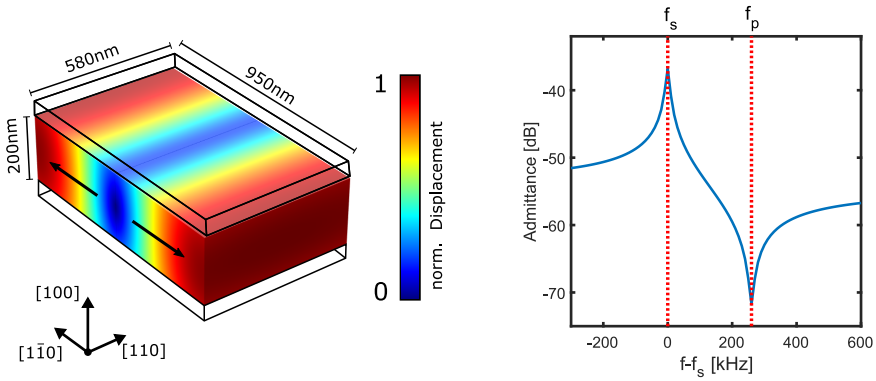

Fig. 4.5 | Simulated GaP piezo resonator. The left panel shows a generic block resonator. The thickness is set by the device layer in the main text, while the width is set to closely match the frequency of the confined nanobeam mode and the length chosen to ensure the mode mass matches the nanobeam breathing mode mass. The relation of the block to the crystal axes are displayed. The color coding displays the displacement of the breathing mode along the [1$\bar{1}$0] direction. Top and bottom electrodes that actuate the mode are indicated by the wire-frame. The right panel shows the simulated electrical admittance between the electrodes. The electromechanical series and parallel resonances, f_s and f_p, respectively, are illustrated.

the overcoupled optical resonator and the nearby waveguide $\eta_{dev} = 0.75$ and the coupling efficiency between the waveguide and the fiber $\eta_{fc} = 0.55$. The remaining losses stem from the filtering setup and the single-photon-detector efficiency. Having calibrated the mode occupation n_{th}, the scattering probability can then be found from the click rate. The calibration between the peak input optical power for 40-ns long pulses and the scattering probability is plotted in Fig. 4.4, as a function of the pulse energy, from the same data set as Fig. 4.2 in the main text. The line is a linear fit to the data, with a proportionality constant of 2.6×10^{-2} μW^{-1}.

4.5.4. Parameters for cross correlation measurement

In our DLCZ-type pulsed experiment, we send two optical pulses to our device. The first pulse, on the blue sideband of the optomechanical cavity, has a length of 40 ns and a peak power of 25 nW, corresponding to a scattering probability $p_{s,write} = 0.06\%$. The second pulse, detuned to the red sideband, also has a length of 40 ns and a peak power of 750 nW, corresponding to a scattering probability $p_{s,read} = 2\%$. The delay between the two pulses is 150 ns and the repetition rate of the experiment is 25 kHz.

4.5.5. Piezoelectric interface

Supplementing the nanobeam discussed in the main text with a high-cooperativity piezoelectric interface would allow for transduction between microwave and optical domains. In such a conversion device, the added noise would predominantly be set by the thermal occupation of the nanobeam, which we show to be

sufficiently low to allow for conversion of a quantum state. The main figures of merit for a conversion device are the efficiency and the added noise. The latter in particular is critically important to the success of the conversion process, as with sufficiently low noise levels, successful conversion can be heralded through detection events. In particular, the added noise, N follows

$$N = \frac{n_m}{\eta_e C_{em}}, \tag{4.6}$$

where η_e is the external efficiency of the electrical input, C_{em} the electromechanical cooperativity, and n_m the unwanted population of the mechanical mode, either due to thermal excitation, incoherent photon absorption or unwanted optomechanical excitation. For the largest optomechanical cooperativity measured in Figure 4.2 in the main text, $C_{om} = 20$ we find a value oof $n_m = 0.35 \pm 0.01$. If we consider a matched electromechanical cooperativity (peak efficiency would occur at $C_{em} \approx C_{om} + 1$), and unity external efficiency ($\eta_e = 1$), we would expect to only add $N = 0.02$ photons of noise in the conversion process. A value of C_{em} that far exceeds the optomechanical cooperativity would further reduce the value of added noise, however at the expense of a reduced conversion efficiency [29].

In Fig. 4.5, we show a simulated generic GaP piezo-resonator and the corresponding electrical admittance curve. The dimensions of the resonator are chosen to match the mass of the optomechanically coupled mode considered in the main text, such that we maintain a large optomechanical coupling rate. As a best estimate for mechanical dissipation in the system, we use the loss rate of the nanobeam mode ($\gamma_m = 2\pi \times 7.96$ kHz, following the mechanical decay rate displayed in Fig. 4.3(a) of the main text). The breathing mode of the pictured piezo-resonator is actuated by a vertical electric field, according to the GaP piezoelectric tensor [74], which could be supplied by top-and-bottom electrodes, as is done in reference [14]. The right panel of Fig. 4.5 shows the simulated admittance of the resonator, around the value of $f_s = 3.05$ GHz to approximately match the nanobeam mode. The typical resonance/ anti-resonance curve of the coupled electrical and mechanical system allows us to estimate the piezoelectric coupling coefficient k^2_{eff}, according to $k^2_{eff} \approx \left(f_p^2 - f_s^2\right)/f_p^2$, where f_s is the resonant frequency of the mechanical mode, and f_p is the parallel resonance of the coupled electromechanical system. From these values, we extract $k^2_{eff} \approx 1.7 \times 10^{-4}$.

Through the addition of a microwave frequency resonator, we can realize high-cooperativity electromechanical interaction with the piezoelectric resonator. In particular, the cooperativity of the piezoelectric interface is described by $C_{em} = k^2_{eff}\omega_m^2/\kappa_e\gamma_m$ [29], where κ_e is the decay rate of the microwave-frequency resonator, and γ_m is the decay rate of the mechanical mode. Importantly, owing to the small size of the piezoelectric resonator, the addition of a microwave resonator will decrease the value of k^2_{eff} through additional parasitic capacitance. Taking a relatively large value of 100 fF for the parasitic capacitance (resulting in a characteristic impedance of 520 Ω, for comparison, see reference [82]), and the simulated value of 0.19 fF for the capacitance of the piezo-resonator,

we estimate a reduced value of $k^2_{\mathrm{eff,red}} \approx 3.3 \times 10^{-7}$. Nonetheless, to achieve a cooperativity of $C_{\mathrm{em}} = 20$, the required quality factor for the microwave resonator can be found to be only $Q_{\mu\mathrm{w}} \equiv \omega_{\mathrm{m}}/\kappa_{\mathrm{e}} \approx 170$.

5

Exploiting Mechanical Supermodes for Wavelength Conversion

In chapter 3 we have seen that an approach using mesoscopic IDTs as an electromechanical interface is not an ideal route towards highly efficient conversion between the microwave and optical telecom domains. A large portion of the inefficiency is attributed to poor mode matching between the nanobeam mode and the itinerant surface acoustic wave. In this context, both the spatial extent and the polarisation of the mode need to be considered. In this chapter we redesign the optomechanical crystal and the electromechancial transducer to solve these problems. We design a nanobeam OMC which allows the mechanical mode to leak out more easily. We opt for a miniaturized piezoelectric bulk acoustic resonator instead of a large traveling wave actuator. We engineer the block resonator such that it is resonant with the mechanical mode of the nanobeam. By achieving strong coupling between the two modes, we are able to treat them as one where the first half interacts optomechanically and the second half electromechanically. As a final step, we surround the device with phononic shields such that we can confine the phonons inside the area of interest. Due to its superior optical properties, we design and fabricate these devices from gallium phosphide.

5.1. Introduction

In chapter 3, we have shown that it is possible to coherently excite a GHz-frequency breathing mode by launching surface acoustic waves at a nanobeam OMC. The efficiency of this process was limited by several geometric and polarisation mismatches between the participating mechanical modes. In order to improve on this, we start by revisiting the mechanical mode of the nanobeam.

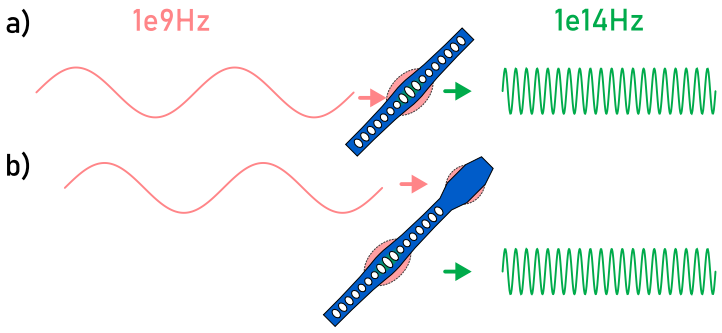

Fig. 5.1 | Optomechanical wavelength conversion schemes. a) A hypothetical scheme where the breathing mode of a nanobeam OMC is directly actuated by a resonant microwave tone. b) A scheme making use of a supermode consisting of two coupled resonators. In this case the microwave tone only interacts with the upper part of the mode while the light field only interacts with the bottom part.

Ideally, this mode is directly actuated using a microwave field. However, as this typically requires nearby electrodes which will likely perturb the light field in the optical cavity and is thus undesirable. To overcome this obstacle, we extend the mechanical mode of the nanobeam so that part of it can interact with the optical cavity in the standard manner and another part can interact with a microwave field. The concept is sketched in fig. 5.1. In this chapter we will first address the design of the device as well as the coupling to the respective modes. Then we will explain how the mechanical mode can be excited efficiently from the microwave domain.

5.2. Device Design

As a first step, we need to address the issue of how we obtain such an extended mechanical mode. Here, we pursue a coupled resonator approach where we couple the breathing mode of the nanobeam to a mechanically connected piezoelectric resonator [18]. In this chapter we break down the problem into three distinct parts:

- Design of the OMC
- Design of the piezo resonator
- Efficient excitation of the mechanical mode from the microwave domain

5.2.1. OMC Design

While a conventional nanobeam OMC is targeted towards a strongly confined and well-isolated mechanical mode, for this application a less isolated mode is desirable in order to facilitate the coupling to the piezoelectric resonator. In order to realize such a mode, we first consider the phononic band structure of the mirror region of a conventional nanobeam OMC, which is shown in the

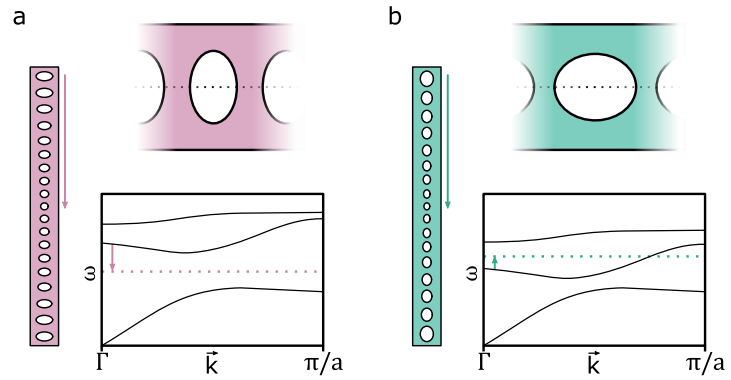

Fig. 5.2 | Comparison of phononic mirror designs. a) A conventional mirror design (top) and the corresponding phononic band structure for modes that are symmetric with respect to the beam axis (dashed line). The defect in OMC (left) is designed such that the second band is pulled down towards the beam center, resulting in a mechanical mode with a frequency inside the mirror band gap (dashed line). This results in highly confined mechanical modes. b) A "leaky" mirror design. The defect here is designed such that the second band is instead pulled up (dashed line), such that the defect mode only sees a partial bandgap. For low k-values, the mode is confined, but near the edge of the Brillouin zone, the defect mode overlaps with one of the mirror bands and can leak out, resulting in weaker confinement.

bottom panels of fig. 5.2 a,b. Between the two lowest bands, a band gap is formed for modes which are symmetric with respect to the beam axis. As the mirror holes are deformed to form the defect (see. Chapter 1), the bands shift to create a defect state. For mirror designs where with a short and wide hole as used in Chapters 3 and 4, this transformation moves the second band down into the band gap (fig. 5.2a), resulting in the defect state, indicated by the dashed red line. Because this mode lies fully within the bandgap, typically this results in high quality factors and little mode leakage. An alternative approach is to use a design, where the second band is pulled up during the transformation to the defect as shown in fig. 5.2b. In this case the defect state (dashed green line), does not fully lie in a band gap and overlaps with the second band at larger k-values [31, 83]. This means that a mechanical excitation can couple to this second band and tunnel out of the beam. Our approach makes use of exactly this process to realize the coupling of OMC mode to that of the nearby piezoelectric resonator.

While the primary motivation for this low-Q mode is an increased coupling to the piezo-resonator, the weak confinement of the mode will also increase the coupling to the bath. In order to suppress the undesirable coupling to the environment, the device can be embedded in a phononic shield [33, 34]. While the 1D structures shown in fig. 5.2 only exhibit band gaps for modes with particular symmetries and polarisations, a phononic shield such as the "cross" design [13, 30] exhibit a full phononic bandgap for modes of all polarisations and symmetries. With this design philosophy, we designed an optomechanical crystal using this leaky design. In simulations, it exhibits an optical mode

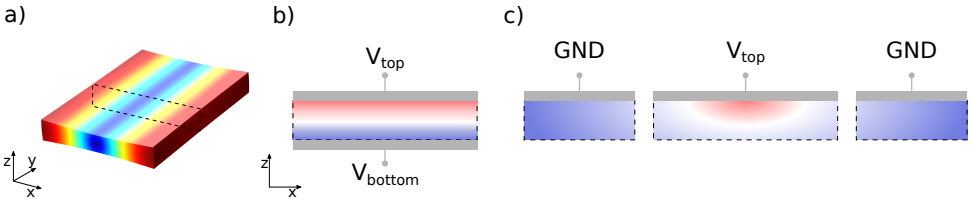

Fig. 5.3 | Actuation and electrode configuration for a block resonator. a) Illustration of the breathing mode of a block resonator in the relevant coordinate system, where y||[110] and z||[001] in a zincblende crystal structure. b) Ideal electrode configuration for this mode where a potential difference between the top and bottom surfaces can be produced directly. Electric potential is sketched in color. c) Alternative electrode geometry, where the potential difference is applied (detected) between the center pad (V_{top}) and the two ground planes on the side (GND). This geometry harnesses only the out-of-plane component of the produced electric field.

at ∼1565 nm and a mechanical mode at 3.07 GHz. In addition to an optomechanical crystal with controllable mode-leakage, we need an appropriate, piezoelectrically active resonator which we can bring into resonance with the mode of interest such that the two modes can hybridize. In the following section, we will discuss our approach to the design of such a resonator in greater detail.

5.2.2. Piezo-Blockresonator Design

Ideally, such a resonator exhibits a breathing mode which can easily be matched to the mode of the nanobeam OMC. As we have seen in fig. 2.2 in chapter 2, the breathing mode of a rectangular block, aligned with the [110] crystallographic direction, produces a well-defined out-of-plane electric field. While such a field could, in principle, be produced by depositing electrodes on the top and bottom of this piezo-resonator (fig. 5.3b), this approach is impractical due to a high level of fabrication complexity. An alternative route is given by a coplanar waveguide configuration where the out-of-plane component of the field under the central electrode is used instead (fig. 5.3c).

5.2.3. Strong Coupling Between Mechanical Modes

By aligning the nanobeam OMC with the [110] direction, we can straightforwardly attach such a block resonator to the end of the nanobeam. In order to reduce the effect of a width mismatch of the two resonators, we make use of a 500 nm-long tapering region to bridge the difference in width. We also add a second, identical taper on the far side of the piezo-resonator to preserve the symmetry of the mechanical mode. The resonance frequency of the block's breathing mode is set by the width of the block. By attaching the block to the end of the nanobeam OMC and sweeping the block width, we can tune the block-resonance through the resonance of the OMC. We perform a width sweep of the block resonator in COMSOL and compute the eigenfrequencies of the structure. We observe a pronounced anticrossing of the OMC and piezo-resonator breathing modes as shown in fig. 5.4. From the splitting of

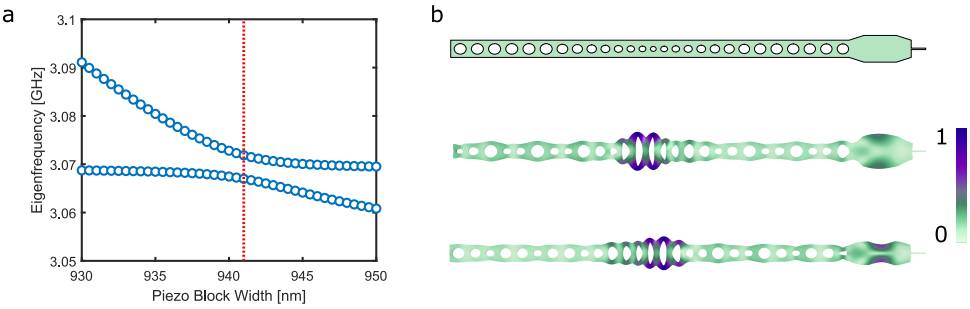

Fig. 5.4 | Strong coupling of the piezoelectric resonator to the OMC mode a) simulated width sweep of the piezo resonator. Shown are a selection of relevant eigenfrequencies. Around 942 nm, we see a clear anticrossing of the two resonances. b) Schematic of the full coupled-mode design (top). Normalized displacements of the symmetric (middle) and antisymmetric (bottom) modes of the hybrid structure for a resonator width of 942 nm (dashed line in a)).

the two modes, we estimate a coupling of ∼3MHz.

5.2.4. Electromechanical Actuation

As a last simulation step, we analyze how the piezo-resonator responds to a microwave drive. We use the electrode configuration shown in fig. 5.3c and set the center electrode as a terminal. The microwave impedance of the coaxial line is assumed to be 50 Ω (see fig. 5.5a). We then perform a frequency domain study where the driving frequency is swept and calculate S11. From this simulation, we can both extract the impedance of the device as well as the k_{eff}^2 parameter, which quantifies how much of the incident microwave energy is converted to the mechanical domain. The simulated result in fig. 5.5b shows two resonances corresponding to the antisymmetric (lower frequency) and symmetric (higher frequency) modes. While the lower frequency mode is noticeably narrower, this difference stems from the difference in the quality factors (∼16000 and ∼6800 respectively) of the modes. For the low- and high-freguency mode, we estimate k_{eff}^2 values of 2.6×10^{-5} and 2.15×10^{-4}. The on-resonance impedance of both modes is in excess of 1MΩ. Due to the large mismatch between these impedances and the 50 Ω coaxial line, the predicted dips for an S11-measurement (see fig. 5.5b) are extremely shallow and will not be resolvable in a real measurement. The implication is that most of the incident microwave power is reflected and the overall conversion will not be very efficient. Moreover, without being able to measure a dip in the microwave spectrum, it is impossible to extract how much of the incident microwave power is actually deposited into the mechanical mode (i.e. the electromechanical conversion efficiency). For an efficient converter, the reflected signal would be extinguished on resonance, meaning that all incident microwave power is actually deposited in the mechanical mode. In order to approach this ideal case, we need to impedance match our piezo-resonator at $\omega_{RF} = \omega_m$. Because our target is efficient conversion, we aim to avoid resistive losses

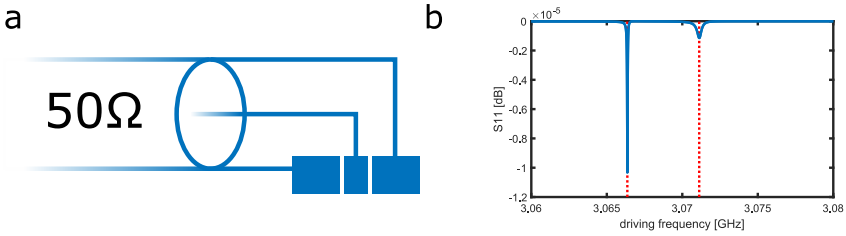

Fig. 5.5 | Simulated S11 Measurement. When connecting such a device to a 50Ω coaxial line as shown schematically in a, the resonances we expect in an S11 measurement are extremely shallow (b). In particular, they are so shallow that they are realistically not measurable.

and fashion this microwave circuit from only inductive and capacitive elements. This means, that the resulting matching circuit is resonant with our device $\omega_m = \omega_{matching} = 1/\sqrt{LC}$. The impedance of the matching circuit is then given by $Z_{matching} = \sqrt{L/C}$. In order to match the high-frequency, high-impedance load of the piezo-resonator, it is crucial to keep the capacitance low and the inductance as high as possible within the constraints. To this end, we use a spiral-inductor as our inductive element and use its parasitic capacitance as the capacitor in order to get a large L/C ratio [82]. The value of L can then be adjusted by the number of turns on the inductor in order to match the resonance frequency to the device. Parasitic capacitances are typically on the order of 10s of fF, which means in order to match a resonance at $\omega_m = 2\pi \cdot 3.06$ GHz, we need an inductance of some 10 nH. With all the design considerations laid out, it is now time to discuss the fabrication and then look at an actual fabricated device.

5

5.3. Fabrication

The Fabrication of these structures consists of two lithography steps. The first step is used to define the microwave circuits and alignment markers for the second exposure. We then sputter a 50 nm thick film of molybdenum-rhenium (MoRe) on the developed resist and remove unwanted metal using a lift-off technique with sonication. The second exposure, which defines the dry-etched areas, is then aligned to the markers from the previous step using an automated marker search. This results in an alignment precision of $\sim$ 10nm. After development, we use a dry etch with a $Cl_2/BCl_3/N_2$ chemistry (flow rates of 10/20/10 SCCM) and 100W of RF power to etch through the 200 nm-thick device layer. We then remove the remaining resist in an 80° bath of N-N Dimethylformamide. In order to access the devices with a lensed fiber, we then proceed to cover the chip in a protective photoresist layer and use a dicing saw to cut alongside the devices (shown in fig. 5.6a). After removing the protective photoresist using a hot acetone bath, we perform a timed underetch in a 10% ammonium fluoride solution, which selectively removes the $Al_{0.64}Ga_{0.36}P$ beneath the device layer. As a final step, we use a critical point dryer (CPD) to dry the sample.

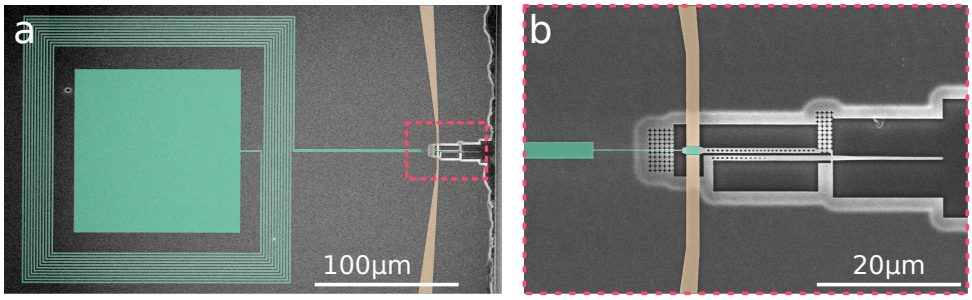

Fig. 5.6 | SEM Images of a Finished Device a) Image of one full device, including the microwave resonator. The center electrode is false-colored in green and the ground in orange. The red-dashed frame indicates the zoom in shown in b). b) Closeup view of the electro-opto-mechanical device. We use a coupling waveguide (bottom) for optical access to the device using a lensed fiber (not shown). The nanobeam (top) is attached to the bulk using phononic shields. The ground electrodes are separated from the beam by a small gap $\sim$ 100nm. The center electrode is connected to the inductor (a) using a small tether which runs through the phononic shield. Light gray areas are suspended.

5.4. Device Characterisation

The fabricated device is shown in fig. 5.6. The center electrode(ground) is false-colored in green (orange). In order to electrically access the shown microwave circuit, we wirebond the chip to a coplanar waveguide on a pcb (not shown). We also wirebond the center conductor of this waveguide to the central pad on the spiral inductor (shown in a). A zoom-in to the device (b) shows how the electrodes attach to the electro-opto-mechanical converter, as well as the full device geometry. The nanobeam (top) is positioned next to a coupling waveguide (bottom), which tapers to a tip in for optical access with a lensed fiber from the edge of the chip. The nanobeam device is attached to the bulk of the chip using a phononic shield.

An initial characterisation of the device reveals an optical mode at $\lambda_c = 1565.7$ nm with a full width at half maximum (FWHM) of 7.34 GHz (see fig. 5.7a). We blue-detune a laser from the optial resonance by $\approx \omega_m/2\pi$ and monitor high frequency noise in the reflected light from the device to find the mechanical modes. At room temperature, we observe two mechanical peaks of equal height around 2.91 GHz with a splitting of 8.7 MHz. In order to fully characterize the device, we then place the device in a dilution refrigerator with a base temperature of $\sim$ 10mK. Cooling the device results in a blueshift of the mechanical modes by $\sim$ 25MHz. While the separation of the two peaks remains relatively constant at 9.2 MHz, the relative heights appear quite different. In this plot, it is possible that the lower frequency mode was driven into self-oscillation, which can explain both the narrow linewidth of 34 kHz and the large peak height. In contrast, the higher-frequency mode is barely visible such that linewidth of 894 kHz of the fitted curve in fig. 5.7c is not necessarily a good representation. At cryogenic temperatures below the T_c of our superconducting electrodes ($\sim$10K for MoRe), we can now also measure our microwave circuit. We perform a simple microwave-

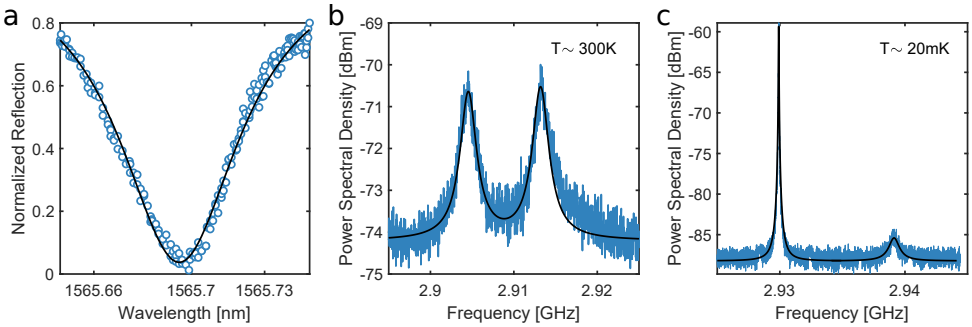

Fig. 5.7 | Basic Device Characterization. The optical cavity (a) has a resonance at 1565nm, with a FWHM of 7.34 GHz. At room temperature, we see two mechanical modes at 2.9045 and 2.9132 GHz. They have linewidths (FWHM) of 1.9264 and 2.4563 MHz, respectively. The black line is a combined fit to both resonances. At millikelvin temperatures (c), the mechanical modes shift to 2.9299 and 2.9391 GHz. The modes are fitted independently (black lines). The lower mode has a FWHM of 34 kHz, but the peak of the higher mode is so poorly resolved that the fit is not a good indication of the actual linewidth (shown is 894kHz).

S11 measurement, which reveals a clear resonance at 2.472 GHz, shown in fig. 5.8 a. Unfortunately, this resonance is rather far-detuned from our mechanical mode, resulting in an impedance-unmatched piezoelectric resonator. Nonetheless, we can still perform a conversion experiment with this device. As in Chapter 4, we start by measuring the lifetime of the mechanical mode using two red-detuned optical pulses with variable delay (not shown). From this measurement, we find the lifetime of the mode to be 1.4 µs. We then red-detune our laser from the optical cavity by ω_m and send 40 ns-long optical pulses to the device with a repetition rate of 50 kHz. At the same time, we send a continuous microwave tone at ω_{MW} to the microwave port of the device. We then sweep the frequency of the microwave tone across both of the mechanical resonances, while collecting scattered photons on resonance with the optical cavity using single photon detectors. The retrieved mechanical spectra are shown in fig. 5.8b and c, and are 192.8 and 212.1 kHz wide. While these linewidths are in reasonable agreement with the measured lifetime, we would expect a slower decay for a device with a properly functioning phononic shield, indicating a discrepancy between the fabricated and nominal shield design. Compared to the measurement in fig. 5.7c, the optical pump is much weaker here and accidental optical driving of the mode can be excluded, meaning that the se extracted linewidths are a better measure than the previously extracted ones. While this experiment confirms that both of these modes are piezoelectrically active, it is not in line with the pulsed protocol from Chapter 1. In order to determine the efficiency as well as noise contribution of our device, we proceed to perform a pulsed conversion experiment using the lower frequency mechanical mode, which showed a slightly higher count rate in fig. 5.8b.

In this experiment, we consider the ratio of the countrate with- and without an RF drive to extract the coherent phonon population of the mode. As a first

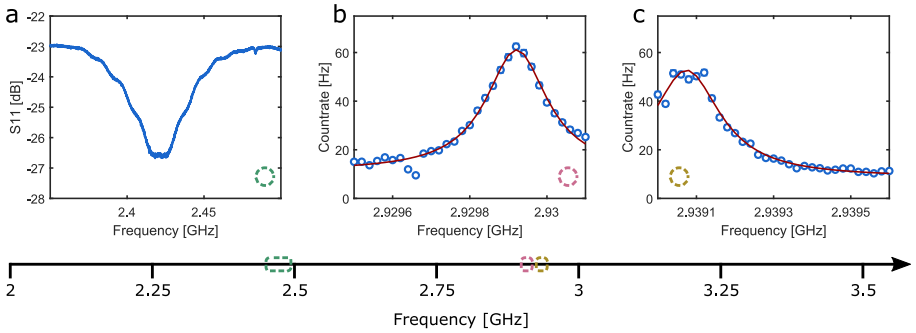

Fig. 5.8 | Continuous Microwave Conversion a) Microwave S11 measurement of an identical device on the same chip. We believe that the dip at 2.42 GHz corresponds to the resonance of our impedance matching circuit, based on the temperature dependence of the resonance. This resonance is red-detuned from the mechanical mode by ∼500 MHz. The S11 is measured with device connected to port 2 of a circulator. We attenuate the input to the circulator by a total of 36 dB (10 dB, 20 dB, 6 dB at the mK, 1K, and 4K stages of the cryostat). The output line is amplified using a low-noise amplifier with 37 dB gain (LNF-LNR1_ 15A). b,c) Characterisation of the microwave-to-optics conversion at mK temperatures. We sweep the frequency of a continuous microwave drive tone while sending laser pulses at $\omega_{\text{Laser}} = \omega_c - \omega m$ to the device. From the spectra, we extract the actual linewidths to be 192.8kHz for the lower frequency mode and 212.1kHz, indicating that the narrow linewidth from fig. 5.7 is likely due to excessive optical driving of the mode. Datapoints show integrated count rates over the length of an optical pulse with dark counts subtracted. Errorbars are one standard deviation resulting from shot noise in photon counting.

step, we need to find the countrate corresponding to the thermal occupation ($\Gamma_{\text{R,base}} \propto n_{\text{th}}$) as well as determine the occupation itself. We achieve this by performing a sideband asymmetry measurement to assess the thermal occupation of the mechanical mode in the presence of our optical drive. With the microwave drive turned off, we send 40 ns-long optical pulses with a peak-power of 250 nW on the blue and red sidebands to the device and monitor the scattering rates Γ_B and Γ_R using SPDs. The scattering rates are shown in fig. 5.9a. We observe a pronounced asymmetry between the two and retrieve a thermal occupation of $n_{\text{th}} = \Gamma_R/(\Gamma_B - \Gamma_R) = 0.71 \pm 1.7 \times 10^{-4}$. Using this measurement, we also determine the optomechanical coupling rate to be $g_0 = 431$ kHz, in reasonable agreement with a simulated value of 699 kHz. We now proceed to use the same settings as for the red-detuned pulse sequence from fig. 5.9a and add a 3 µs-long microwave pulse. The duration of this pulse is chosen such that, using a square microwave pulse, the loading of the mechanical mode with a lifetime of 1.4 µs is most efficient.

As in Chapter 1, we time the two pulses such that the optical pulse arrives at the end of the microwave pulse. In this fashion, the microwave pulse first excites the mode and the subsequent optical pulse reads out the mechanical mode. We then sweep the frequency of the microwave tone across the lower-frequency resonance. By comparing the peak countrate $\Gamma_{\text{R,conv,peak}} = 1.66 \pm 0.13$ Hz in fig. 5.9b to the countrate obtained from a red-detuned optical pulse alone ($\Gamma_{\text{R,base}} = 0.3 \pm 0.026$ Hz), we can use $\Gamma_R \propto n_{\text{phonon}}$ to determine the coherent

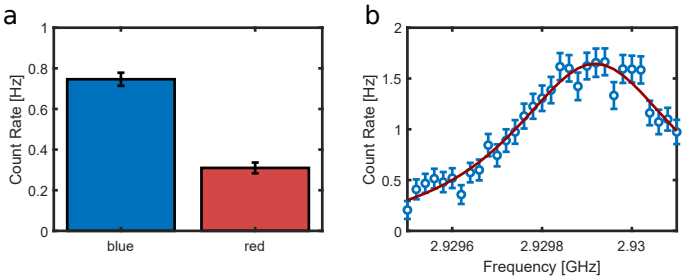

Fig. 5.9 | Pulsed Conversion and Asymmetry a) Sideband asymmetry measurement. We send 40 ns-long laser pulses either on the blue or red sideband to the device and monitor the scattering rate from the Stokes- or anti-Stokes processes using superconducting nanowire single photon detectors (SNSPDs). We retrieve a thermal occupation of $n_{\mathrm{th}} = 0.71 \pm 1.7 \times 10^{-4}$ for a peak power of 0.25 µW and a repetition rate of 50 kHz. We then use the same settings from the red sideband setting from (a) and turn on a 3 µs-long microwave pulse with a peak power of -41 dBm. We set the timing such that the optical pulse arrives at the end of the square pulse and sweep the frequency of the microwave pulse across the lower-frequency resonance. Shown are detector countrates integrated over the optical pulse with the dark counts subtracted. We extract a linewidth of 234 kHz. The increased linewidth is due to the spectral breadth of the microwave pulse compared to the continuous tone in fig. 5.8b.

phonon occupation due to the microwave drive. We determine $n_{\mathrm{phonon,coh}} = n_{\mathrm{phonon,total}} - n_{\mathrm{th}} = \Gamma_{\mathrm{R,conv,peak}}/\Gamma_{\mathrm{R,base}} \cdot n_{\mathrm{th}} - n_{\mathrm{th}}$ to be ~3.8 phonons. Referencing this to the number of microwave photons incident to the input of the device with each pulse yields a microwave photon-phonon efficiency of 3.1×10^{-11}. Further, we can determine the rate of incident microwave photons at the input of the device to be (6.13×10^{15} Hz). Comparing this to the peak measured photon countrate in fig. 5.9b yields a photon number efficiency of $2.71 \pm 0.22 \times 10^{-16}$. We can now further break down this efficiency into its contributions $\eta_{\mathrm{total}} = \eta_{\mathrm{MW,phonon}} \cdot \eta_{\mathrm{readout}} \cdot \eta_{\mathrm{dev}} \cdot \eta_{\mathrm{fc}} \cdot \eta_{\mathrm{det}}$, where $\eta_{\mathrm{MW,phonon}}$ is the previously determined microwave photon-phonon transfer efficiency, η_{readout} the efficiency of swapping the phonon onto the optical readout field, and η_{dev},η_{fc},η_{det} are the coupling efficiency to the waveguide, the fiber-coupling efficiency, and the efficiency of the detection path, respectively. The latter three can be measured independently and we extract $\eta_{\mathrm{readout}} = 2.39 \times 10^{-4}$, $\eta_{\mathrm{fc}} = 0.22$, and $\eta_{\mathrm{det}} = 0.012$. While this proof-of-principle demonstration does not improve on the previous result from Chapter 3 in terms of efficiency, the approach itself shows more promise for future improvements. The largest limitation remains in the microwave-phonon conversion, which is due to the very large resonator impedance and the difficulty associated with the proper impedance matching. The other contributions can be improved by smaller technical improvements. The readout efficiency can be improved by using a stronger optical pump pulse, at the cost of a higher thermal occupation. However, the thermal occupation is assumed to originate from absorbed intracavity photons and thus, a narrower optical resonance would allow for a stronger pump at an equal detuning of ω_{m}. The fiber-coupling and the detection efficiencies can be improved by using tapered fiber coupling [81] as well as improvements in the detection setup.

Ultimately, the most important step forward lies in improving the frequency-matching of the microwave- and mechanical resonators. Further, reducing the mechanical linewidth will boost the electro-and optomechanical cooperativities and thus, also improve the efficiency.

Conclusion

In this chapter, we have introduced a new type of electro-opto-mechanical resonator for microwave-to-optics conversion. This converter makes use of an extended mechanical mode where only a part of the mode interacts with the microwave- and optical fields, respectively. We realize this extended mode by bringing two mechanical modes of equal symmetry into resonance with each other and coupling them strongly through a mechanical waveguide. We then demonstrate conversion using both the symmetric and antisymmetric modes, as well as extract a total photon number conversion efficiency of $2.71 \pm 0.22 \times 10^{-16}$, including all setup losses. While this efficiency is very low, this is likely due to the large mismatch in the resonance frequency of our impedance matching circuit and the mechanical mode. Effectively, this means that our 50Ω coaxial input line sees a device impedance of several Mega-Ohm, which causes an overwhelming fraction of the microwave tone to be reflected without interacting with the piezo resonator. As a result, we have demonstrated the working principle of the device, but improvements on the microwave side are needed in order to raise the efficiency by an appreciable amount.

6

Conclusion and Outlook

The work presented in this thesis is the story of the exploration of III/V semiconductors for the purpose of electro-opto-mechanical microwave to optics conversion. We studied both gallium arsenide and gallium phosphide as they are piezoelectric as well as exhibit desirable properties for optomechanics such as a a large refractive index. Because the main motivation for this reasearch direction is the realization of a converter capable of converting single microwave excitations from a qubit, this motivation imposes several constraints: low added noise and a high conversion efficiency. Added noise in an electro-opto-mechanical converter predominantly stems from thermal motion of the mechanical mode. In Chapters 3 we address this issue by cryogenically cooling the mechanical mode of a GaAs nanobeam OMC near its quantum ground state to reduce the thermal noise to a minimum. While we were able to operate the device with a thermal background of less than one phonon, the work highlighted the shortcomings of GaAs as a material platform for quantum optomechanics at telecom wavelengths, primarily due to optical absorption and the associated incoherent heating of the mechanical mode. In Chapter 4, we address the issue of optical absorption by exploring gallium phosphide as a material platform. While similar to GaAs in many regards, GaP exhibits a significantly larger bandgap than GaAs. With this material, we operate a piezoelectric optomechanical crystal at much lower thermal occupations of the mode compared to similar devices in GaAs. Further, we are able to demonstrate non-classical correlations between photons and phonons using this device, indicating that gallium phosphide is a superior material platform for quantum optomechanics compared to GaAs. Finally, in Chapter 5, we design, fabricate, and characterize a new type of optomechanical device, specifically aimed at wavelength conversion. By strongly coupling two separate mechanical modes, we are able to interact with one part of the mode optically and with the other part electrically. While this approach allows for independent engineering of the electrical and optical interfaces, the small footprint of the piezoelectric resonator results in a large electrical impedance. Because coupling from a

50 Ω coaxial line to such a high impedance resonator can never be efficient, we fabricate an on-chip impedance matching circuit consisting of a lithographically patterned spiral inductor. The inductor provices a geometric inductance as well as a parasitic capacitance, which we use as an LC resonator, whose resonance frequency we try to match to our mechanical resonator. While early attempts at the impedance matching resulted in a rather large detuning between the impedance matching circuit and the piezo-resonator, we are able to demonstrate conversion with both the symmetric and antisymmetric modes and a thermal noise corresponding to only 0.71 phonons. While the efficiency is so far only a small improvement over the one measured in Chapter 3, further efforts aimed at improving the impedance matching of the device should allow significant improvements of the efficiency.

The single-material approach that we pursued throughout this work allows for a fabrication workflow with relatively few steps. In addition, the small number of non-zero components in the piezoelectric tensor of III/V semiconductors allows for the engineering of well-controllable modes. However, this approach also has large drawbacks such as the requirement to choose either strong piezoelectric and weak optomechanical coupling or vice versa. While we opted for the latter option, particularly the electrical impedance of small-scale piezoelectric resonators becomes very large when the piezoelectric coupling is weak. A further complication arises if one considers the long-term goal of integrating these devices directly with superconducting qubits. While demonstrations of III/V thin films on SiO_x on silicon exist, that would allow for integration with silicon qubits, they are typically not scalable approaches. One promising approach to overcoming these challenges is the use of hybrid material platforms. By using a piezoelectric thin-film on top of silicon-on-insulator (SOI) as a starting material, it becomes feasible to pick and choose properties for a final device. While this comes at the cost of a more complex fabrication procedure, the potential payoffs due to the use of strong piezoelectrics are very large and recent demonstrations using an aluminium-nitride on SOI platform [31] are very promising.

In principle, on-chip electro-opto-mechanical converters are well-suited to the integration with superconducting qubits in terms of their size. However, the lack of tunable resonances combined with inherent fluctuations in the fabrication process highlights an issue that, to date, has not been addressed: scalability. For the experiments in this thesis, we fabricated 10s of devices on a chip and chose the best ones. For small experiments involving only a few qubits, it seems likely that this strategy can be upscaled such that the probability of having n devices with the desired properties become finite. In the long term, where is desirable to have many qubits on a chip, each with its own optical interface, this strategy breaks down. In order to reach this goal, it will be necessary to be able to repeatably fabricate near-identical devices. To this end, it will be of interest to transition to more industry-ready fabrication flows, with the goal of achieving this high degree of reproducibility as well as high yield. In addition, developing devices with tunable optical- or mechanical resonances could make the constraints on reproducibility a little bit looser.

Currently, electro-opto-mechanical wavelength converters are starting to move beyond proof-of-principle demonstrations. While there are technical challenges ahead, solutions to these will unlock more and more exciting applications, which may in the near term start to impact also the quantum computing community.

Summary

In cavity optomechanics, optical fields are coupled to the displacement of mechanical resonators. While it is interesting to study fundamental aspects of this interaction, it is the ability to link this mechanical displacement to various other degrees of freedom that inspires many applications in the field. In these applications, the mechanical resonator can be used as a handle to an external influence for the purpose of sensing, but also as a transducer between two otherwise detached degrees of freedom. The latter approach is the focus of this work. A particularly interesting regime for such a transduction process is between a few-gigahertz microwave tone and optical photons at telecom wavelengths around 1550 nm, connecting the operating regimes of long-range telecommunication with that of superconducting quantum nodes. Bridging the gap between these domains is an essential step towards any size of quantum network based on superconducting nodes, as the losses encountered in microwave transmission lines prohibits the connection of such nodes over length scales extending beyond a few meters. As such, a transducer between the few-gigahertz and optical telecom domains would enable the use of low-loss optical channels to connect remote superconducting nodes, given that the quantum information is preserved throughout the conversion process. One approach of realizing such a converter makes use of a gigahertz-frequency mechanical mode as the transducing element, which is coupled to the optical telecom domain using the optomechanical interaction and to the microwave domain using the electromechanical interaction.

In this work, we aim to unify both of these interactions in a single device by designing and fabricating optomechanical devices from the III/V semiconductors, which, alongside their good optical properties, are also piezoelectric.

In Chapter 2, we motivate our material choice and introduce the relevant properties of the materials, as well as their impact on the fabrication process. Following the material discussion, we then set out in Chapter 3 to realize a microwave-to-optics converter made of an optomechanical crystal in gallium arsenide, which we resonantly couple to a interdigital transducer using surface-acoustic-waves. With this device, we demonstrate the first microwave-to-optics conversion using a mechanical mode with an average number of thermal excitations below one. As well as verifying the coherence of the conversion process, our experiments also highlight the limitations arising from the material choice due to absorption-induced incoherent heating of the mechanical mode. The material choice itself then becomes the central topic of Chapter 4, where we opt for a gallium phosphide, a relative of gallium arsenide, which prominently features a larger bandgap. With this material we show non-classical correlations between photons an phonons. We enter a a regime that was

previously inaccessible to devices made from piezoelectric materials, a promising step towards realizing the noise-requirements for microwave-to-optics converters. In Chapter 5, we use the insights from the two previous chapters to design a new type of electro-opto-mechanical resonator, specifically aimed at microwave-to-optics conversion. We miniaturize the electromechanical interface and use strongly coupled mechanical resonators for the transfer of excitations between the microwave and mechanical mode. We fabricate and characterise initial devices as well as demonstrate the validity of the functioning principle. Finally in Chapter 6, we reflect on the results of the previous chapters and highlight some potential advantages of other approaches.

Samenvatting

In cavity-optomechanica wordt licht gekoppeld aan de verplaatsing van een mechanische oscillator. Deze interactie is het onderwerp van fundamenteel onderzoek, maar de mogelijkheid om de verplaatsing aan verschillende andere graden van vrijheid te koppelen inspireert de meeste toepassingen van dit onderzoek. Het mechanische element kan worden gebruikt als een sensor, maar ook als een omzetter tussen twee onafhankelijke graden van vrijheid. Het laatstgenoemde is de focus van dit werk. Een belangrijk voorbeeld van een omzettingsproces is die tussen radiogolven met een frequentie van enkele GHz en optische signalen in het nabij-infrarood deel van het optische spektrum met golflengten rond 1550 nm. Dit proces maakt een verbinding tussen het bedrijfsregime van supergeleidende quantum computers en die van de lange afstands telecommunicatie. Technologisch gezien is dit noodzakelijk om een netwerk van supergeleidende quantum computers te realiseren, omdat gewone radiogolfleiders te veel verliezen hebben om quantum informatie te kunnen delen tussen twee quantum computers die meer dan enkele meters uit elkaar staan. Als het mogelijk zou zijn om radiogolf-signalen om te zetten in nabij-infrarood fotonen, kunnen glasvezels worden gebruikt om efficient en bijna zonder verlies informatie te delen tussen twee of meer quantum computers. Als de quantum eigenschappen van de signalen kunnen worden bewaard tijdens dit omzettingsproces, dan kan de omzetter fungeren als een onderdeel van een quantum netwerk. Één mogelijke maneer om zo een omzetter te realiseren maakt gebruik van een hoog frequente mechanische resonator als het omzettende element. Deze resonator kan worden gekoppeld aan nabij infraroode fotonen middels de optomechanische interactie. Tegelijkertijd kan dezelfde resonator ook worden gekoppeld aan radiogolf-signalen middels de piezoelectrische interactie. In deze scriptie proberen wij deze twee interacties op één chip te verenigen. Om dit doel te bereiken, fabriceren wij onze electro-opto-mechanische structuren van III/V halfgeleiders, die wenselijke optische eigenschappen hebben en piezoelectrisch zijn. In hoofstuk 2 motiveren wij de materiaalkeuze en introduceren wij de belangrijkste materiaaleigenschappen. Verder worden de gevolgen van de materiaalkeuze voor het fabricatie proces besproken. In hoofdstuk 3 realiseren wij een microgolf-naar-licht omzetter die bestaat uit een optomechanisch kristal gemaakt van galliumarsenide. Dit optomechanisch kristal wordt resonant gekoppeld aan een interdigital transducer door surface-acoustic-waves. Met deze omzetter demonstreren wij voor het eerste keer microgolf-naar-optics conversie waarbij de mechanische resonator in een toestand blijft met gemiddeld minder dan één thermische excitatie. Wij bevestigen de coherentie van dit process en leggen uit waar de limitaties van de materiaal keuze liggen. In hoofdstuk 4 wordt de materiaalkeuze zelf het centrale onderwerp. In dit hoof-

stuk kiezen wij voor galliumphosphide, een halfgeleider uit de III/V familie met een grotere band gap dan galliumarsenide. Met dit materiaal demonstreren wij een niet-klassieke correlatie tussen fotonen en fononen. Wij bereiken daarmee een regime dat eerder nooit toegangelijk was voor piezoelectrische materialien. In hoofdstuk 5 gebruiken wij inzichten uit de voorafgaanden twee hoofdstukken en ontwerpen een nieuw soort electro-opto-mechanische resonator die is aangepast voor het doel microgolf-naar-optics conversie. Wij verkleinen het elektro-mechanische deel van dit resonator een gebruiken twee aparte, maar sterk aan elkaar gekoppelde mechanische resonatoren om beter signale te kunnen omzetten tussen de microgolf en mechanische domeinen. Wij presenteren eerste gefabriceerte resonatoren en bevestigen dat het idee achter dit ontwerp kan werken. Tot slot, in hooftstuk 6 kijken wij terug naar de drie experimenten en trekken we conclusies over mogelijke voordeelen van andere materialen.

Zusammenfassung

Das Forschungsgebiet der Cavity-Optomechanik beschäftigt sich mit der Kopplung zwischen Lichtfeldern und der Auslenkung eines mechanischen Resonators. Einerseits ist es interressant die optomechanische Wechselwirkung selbst zu untersuchen. Andererseits bietet die Möglichkeit, auch andere Freiheitsgrade an diese mechanische Auslenkung zu koppeln eine Vielzahl an potentiellen Anwendungen solcher Systeme, z.B. als Sensoren oder Signalwandler. Genau dieser zweite Aspekt ist der Hauptfokus dieser Dissertation. Ein besonders interessantes Beispiel eines solchen Signalwandlungsprozesses spielt sich zwischen Mikrowellen mit Frequenzen im GHz-Bereich und Licht im optischen Telekom-Band, mit Wellenlängen um 1550 nm ab. Dieser Prozess verbindet dann den Frequenzbereich in dem sich supraleitende Quantencomputer befinden mit dem technologisch interessanten regime der Telekommunikation. Aufgrund der starken Verluste in Mikrowellenleitern ist es nicht möglich zwei separate supraleitende Quantencomputer miteinander zu verbinden, sofern diese durhc mehr als einige Meter voneinander getrennt sind. Sollte es möglich sein diese Mikrowellensignale erst ins optische Telekom-Band umzuwandeln, ohne dass Quanteninformation veloren geht, dann würde dies die Realisierung eines Quantennetzwerkes ermöglichen. Ein Ansatz, einen solchen Signalwandler zu realisieren, beruht auf der Verwendung eines hochfrequenten mechanischen Resonators im GHz-bereich. Dieser Resonator kann dann mithilfe der optomechanischen Wechselwirkung an das optische Telekom-Band, und mithilfe des piezoelektrischen Effektes an elektrische Mikrowellen gekoppelt werden. In dieser Dissertation ist das Ziel diese beiden Wechselwirkungen in einem hybrid-resonator zu vereinen in dem wir optomechanische Strukturen aus III/V Halbleitern entwerfen und herstellen. Diese Materialien weisen sowohl wünschenswerte optische Eigenschaften als auch ein piezoelektrisches Moment auf. In Kapitel 2 behandeln wir die Auswahl der Materialien und stellen ihre relevantesten Eigenschaften vor, sowie ihren Einfluss auf den Herstellungsprozess. Danach, in Kapitel 3, präsentieren wir einen Mikrowellen-zu-Licht Wandler, hergestellt aus Galliumarsenid. Dieser Wandler besteht aus einem optomechanischen Kristall welcher mithilfe resonanter surface-acoustic waves an einen interdigital transducer gekoppelt ist. Hiermit demonstrieren wir zum ersten mal einen Mikrowellen-zu-Licht Wandlungsprozess der mithilfe eines mechanischen Resonators geschieht, welcher im Durschnitt weniger als eine thermische Anregung besitzt. Darüberhinaus zeigen wir, dass dieser Prozess Kohärent abläuft und diskutieren zusätzlich die Limitationen der verwendeten Materialplatform. Die Auswahl des Materials selbst rückt dann in Kapitel 4 in den Vordergrund. Hier verwenden wir nun Galliumphosphid, ein zu Galliumarsenid verwandter III/V Halbleiter der eine erheblich größere Bandlücke aufweist. Mit einem op-

tomechanischen Kristall aus diesem Material demonstrieren wir nicht-klassische Korrelationen zwischen Photonen und Phononen. Damit dringen wir in ein Regime vor, welches mit piezoelektrischen Materialien bisher nicht zugänglich war. Weiterhin stellt dieses Resultat einen vielversprechenden Schritt in Richtung optomechanischer Mikrowellen-zu-Licht Wandlung im Quantenregime dar. In Kapitel 5 bringen wir dann die neuen Einsichten aus den zwei vorherigen Kapiteln zusammen und entwerfen einen neuartigen elektro-opto-mechanischen Resonator der konkret auf Mikrowellen-zu-Licht Wandlung ausgelegt ist. Wir verwenden einen einen miniaturisierten elektromechanischen Resonator, welchen wir stark an sein optomechanisches Gegenstück koppeln, um Anregungen zwischen der Mikrowellen- und der Optischen Domäne transferieren zu können. Wir stellen erste solche Resonatoren her und bestätigen die Idee des Funktionsprinzips. Zum Schluss in Kapitel 6 blicken wir dann zurück auf die vorherigen Kapitel und vergleichen den gewählten Ansatz mit möglichen Alternativen.

Acknowledgements

No part of a research project is ever truly a solo effort. So I would like to take this part of my thesis to thank people who helped make this four-year project a great experience.

First and foremost, I would like to thank **Simon Gröblacher** for taking me on for this project and for believing in me for the last four years. While I don't think I had a good grasp of the project when I agreed to join, today I can happily look back and say that I cannot think of a project which would have suited me better. When I joined the group it was still a small group of first-generation students. It's been a joy to see the group develop and grow as it transitions to a second generation and I am very curious how the group will develop over the coming years.

Secondly, I would like to thank my co-promotor **Kobus Kuipers**. While we didn't interact very much, I always appreciated your direct style of communication and your humor during our meetings. Your questions always forced me to reflect on my work and planning and, as such, were extremely helpful.

Thirdly, I would like to express my thanks to the person with whom I've had the pleasure of sharing a large fraction of the work in this thesis: **Rob**. It's been a pleasure working together for the past 2.5 years. I really enjoyed being able to share my fabrication knowledge and at the same time being able to learn from you in the lab. I also cherished our non-work discussions about bread baking or speaker stands and I will continue to listen to many great artists that you've recommended to me over the years. Thank you especially for your help with this thesis. I wish you all the best for the future.

At this point, I would like to thank the members of the group, both current and former: **João**, I really enjoyed our discussions about food or sneakers. You were always a reliable source for restaurant recommendations. **Claus**, I really enjoyed our coffee breaks together. Thank you also for teaching me a lot of cleanroom stuff in the beginning and sharing your III/V knowledge with me. **Andreas**, your expertise in the lab, combined with your willingness to help others makes you a truly special person. You've taught me a lot about cryogenic measurements and setups and I hope I've given a small amount back to you. It was my pleasure to be your paranymph and I wish you all the best for your fellowship and beyond. **Igor**, much like Andreas, you've taught me a lot in the lab and I've really enjoyed being able to share some of my knowledge in the context of the slapping project. **Richard**, thank you for mentoring me in the cleanroom in the beginning and for fabrication tips along the way. I wish you success with your own group at 3ME. **Niccolo** and **Rodrigo**, I really enjoyed working with you guys and talking about silicon etch recipes. **Maarten**, I've really enjoyed the slightly different angle you brought

to the group and discussing fabrication stuff with you. **Jingkun**, I wish you all the best with your ambitious slapped devices. They look extremely cool and I hope they give you nice results. **Clemens**, thank you for teaching me about microwave measurements and for introducing me to bouldering. I really enjoyed our interactions both at and outside of work. **Bas**, I really enjoy the different perspectives you have brought to the group and I'm excited to follow your scientific career. Also thank you for proofreading my samenvatting. **Max**, it's been a pleasure being able to discuss parts of your Master's project with you. Yiwen is lucky to have you in her group and I wish you all the best for your own PhD. Also thanks for proofreading chapter 2. **Kees**, I enjoyed being able to mentor you as "my" Master's student (together with Rob). I've enjoyed your visits whenever you were back at the university and it's always fun to catch up. I wish you the best of luck for your future. **Matthijs**, even though our projects were quite far apart, I enjoyed our discussions at lunch or during group meetings. Also thanks for the 12 o' clock lunch reminders. **Parsa**, I've really enjoyed discussing your project with you and thinking about wavelength conversion in a different material system. Hopefully the things we've found out in the past years can help you a little along the way. **Fred**, thanks for all the things you've taught me about superconducting qubits. I also enjoyed our discussions on how to make superconducting resonators in III/Vs work. **Nina** and **Yu**, good luck with your projects. **Pieter**, I really enjoyed your short stay in the group. Good luck with your PhD project in the US. **Ulderico**, **Stefanos**, **Jie**, **Wouter**, **Klara**, and **Roald**, I also want to thank you for the interesting discussions we've had in the past years.

Important contributions to this work were also provided by collaborators on the various sub-projects. I would like to thank **Kartik Srinivasan** for help with the GaAs work and specifically the paper which is Chapter 3. I also want to thank the people who were involved in the epitaxy of the source material which we used. For the GaAs samples, I want to thank **Andrea Fiore** and **Frank van Otten**. For the GaP samples, I want to thank **Rémy Braive**, **Ines Sagnes**, **Grégoire Beaudoin**, **Konstantinos Pantzas**. Without you this work would not have been possible.

Of course, many people outside the Gröblacher Lab contributed to this work as well. Here I would like to mention those with whom I've interacted the most.

Felix, you're an extremely kind person and a pleasure to work with. I'm glad you introduced me to the PhD council and I am glad that I was able to be physically at your defence and even play photographer. Also thanks for all the tips for the job hunt. I wish you and your family a great future in Germany. **Mark**, you were a tremendous source of information and a fantastic officemate. You're extremely patient in explaining things and always eager to help. Thank you. **Martijn**, our interactions were mostly of a non-work nature, but nonetheless I always enjoyed stopping by in D115 for a chat. Also thanks for telling me about "In de Keuken van Floris", it's become one of my favorites and I will miss it when I move away from Delft. **Sarwan** and **Ines**, we met when TAing for the PEP project. Back then we were all still at the beginning,

but we've all matured a lot since then as researchers. I wish you both the best for finishing your PhDs and for the future beyond. **Daniel**, your corner in D112 always had a bit more of a chill energy than Igor's (right next to you). Thank you for patiently answering my questions about microwave physics. **Fatemeh**, you are a very kind person and a great officemate. I wish you and your family the best for the future.

Martin, I enjoyed our time during the Physics with Industry workshop and I admire your drive and motivation to get things done. **Sonakshi**, I've had a lot of fun teaching you about fabrication. I also really enjoyed to be on the PhD council together with you. **Thomas**, thanks for all the n-tuple chocolate cake over the years.

Michael, you're a great addition to our office. Thank you for keeping D113 a fun place. **Luigi**, I've enjoyed our cleanroom discussions about your nanopillars. Good luck with all the *ETCHING*.

While it is impossible to mention all the cleanroom users who contributed in some way, I would like to extend a special thanks to the members of the Kavli-EBPG WhatsApp group, who have put up with my frequent early-morning holder unload requests over the years. Special thanks in this regard to **Elvedin**. Also thank you to **Sergei** for our discussions on processing recipes and all your patience with the wirebonder. You are truly a wizard with that machine.

A big thank you also goes to the people who keep the cleanroom running day in and out. **Marc**, **Charles**, **Marco**, **Pauline**, **Eugene**, **Ewan**, **Arnold**, and **Anja**, thank you for your assistance over the years. You all keep the cleanroom running smoothly and always try to solve problems quickly.

I would like to thank the support staff of the department for their work during the years. **Maria** thank you for handling all the paperwork in the beginning and for helping me with all sorts of orders or shipping issues. **Tino**, thank you for help with all the little things around the lab, but also the big stuff like helping set up the Yellow Lab in the K-Wing. **Ronald**, thanks for all the parts you have made over the years and for your advice on designing them. I also want to thank the rest of the management team for their support during the last four years: **Etty**, **Heleen**, **Marijke**, and **Erika**.

I also want to extend a special thank you to anyone who helped keep building 22 and the cleanroom open for business during the pandemic. This is really a tremendous achievement that makes a big difference for many researchers.

Finally, I would like to thank the people who have contributed to this work through emotional support more than anything. **My parents**, **Martina** and **Markus**, thank you for everything. For supporting me up to this point and always believing in me. And thank you for all the advice you have given me over the years. **My grandparents**, **Eva**, **Otmar**, **Heidi**, and **Oskar**, also thank you for supporting me and for believing in me. And last but not least, I want to thank you, **Loes**, for supporting me when I was struggling and for sharing most of the last 4 years with me. I am glad that through this project we have found each other and I am more than excited to see what the future has in store for us.

Appendix

6.1. Device Parameters

Here, the relevant design parameters for the OMC designs in this work will be given.

GaAs Nanobeam, conventional design

Beam Width	550 nm
h_x	200 nm
h_y	360 nm
Beam Thickness	250 nm
a	418 nm
Orientation Along Crystal Axis	[110]

GaP Nanobeam, conventional design

Beam Width	610 nm
h_x	180 nm
h_y	360 nm
Beam Thickness	200 nm
a	490 nm
Orientation Along Crystal Axis	[110]

GaP Nanobeam, leaky design

Beam Width	570 nm
h_x	360 nm
h_y	300 nm
Beam Thickness	230 nm
a	550 nm
Block Length	1500 nm
Taper Length	500 nm
Tether Length	500 nm
Orientation Along Crystal Axis	[110]

6.2. MATERIAL PROPERTIES

Here, relevant material properties are given which were used for simulations in this work

GAAS

Refractive Index	3.989
Poisson Ratio	0.31
Density	5329 $kg\,m^{-3}$
p_{11}	-0.165
p_{12}	-0.12
p_{44}	-0.072

GAP

Refractive Index	3.054
Poisson Ratio	0.31
Density	4140 $kg\,m^{-3}$
p_{11}	-0.151
p_{12}	-0.082
p_{44}	-0.074

MORE

Poisson Ratio	0.31
Density	13500 $kg\,m^{-3}$
Young's Modulus	365 GPa
Poisson Ratio	0.285

Curriculum Vitæ

Moritz Forsch

20-02-1993 Born in Duisburg, Germany.

Education

2004–2011 Secondary School
Städtisches Stiftsgymnasium, Xanten, Germany (2004–2008)
St. Paul's Episcopal School, Mobile, AL, USA (2008–2011)

2011–2016 B.Sc. and M.Sc. in Physics
Universität Regensburg
B.Sc. Thesis: Low-field magnetotransport through pn junctions in graphene: Numerical study
Supervisor: Prof. Dr. K. Richter
M.Sc. Thesis: Interface-induced Spin-Orbit Coupling in GaAs Core-Shell Nanowires
Supervisor: Prof. Dr. D. Bougeard

2016–2020 PhD. Physics
Delft University of Technology
Thesis: Building Blocks for Wavelength Converters
Promotor: Dr. S. Gröblacher

List of Publications

6. R. Stockill*, **M. Forsch***, G. Beaudoin, K. Pantzas, I. Sagnes, R. Braive, and S. Gröblacher, *Gallium Phosphide as a Piezoelectric Platform for Quantum Optomechanics*, Phys. Rev. Lett. **123**, 163602 (2019)

5. **M. Forsch***, R. Stockill*, A. Wallucks, I. Marinković, C. Gärtner, R. A. Norte, F. van Otten, A. Fiore, K. Srinivasan, and S. Gröblacher, *Microwave-to-optics conversion using a mechanical oscillator in its quantum ground state*, Nature Phys. 16, 69-74 (2020)

4. R. A. Norte, **M. Forsch**, A. Wallucks, I. Marinković, and S. Gröblacher, *Platform for measurements of the Casimir force between two superconductors*, Phys. Rev. Lett. **121**, 030405 (2018)

3. F. Dirnberger, D. R. Abujetas, J. König, **M. Forsch**, T. Koller, I. Gronwald, C. Lange, R. Huber, C. Schüller, T. Korn, J. A. Sánchez-Gil, and D. Bougeard, *Tuning spontaneous emission through waveguide cavity effects in semiconductor nanowires*, Nano Lett. **19**, 7287 (2019)

2. F. Dirnberger, M. Kammermeier, J. König, **M. Forsch**, P. E. Faria Junior, T. Campos, J. Fabian, J. Schliemann, C. Schüller, T. Korn, P. Wenk, and D. Bougeard, *Ultralong spin lifetimes in one dimensional semiconductor nanowires*,Appl. Phys. Lett. **114**, 202101 (2019).

1. S. Furthmeier, F. Dirnberger, M. Gmitra, A. Bayer, **M. Forsch**, J. Hubmann, C. Schüller, E. Reiger, J. Fabian, T. Korn, and D. Bougeard, *Enhanced spin-orbit coupling in core/shell nanowires*, Nature Comm. **7** 12413 (2016).

* These authors contributed equally to this work

References

[1] Zhang, J. *et al.* Observation of a many-body dynamical phase transition with a 53-qubit quantum simulator. *Nature* **551**, 601–604 (2017).

[2] Arute, F. *et al.* Quantum supremacy using a programmable superconducting processor. *Nature* **574**, 505–510 (2019).

[3] Kimble, H. J. The quantum internet. *Nature* **453**, 1023–1030 (2008).

[4] Satzinger, K. J. *et al.* Quantum control of surface acoustic-wave phonons. *Nature* 661–666 (2018).

[5] Chu, Y. *et al.* Quantum acoustics with superconducting qubits. *Science* **358**, 199–202 (2017).

[6] Moores, B. A., Sletten, L. R., Viennot, J. J. & Lehnert, K. W. Cavity quantum acoustic device in the multimode strong coupling regime. *Phys. Rev. Lett.* **120**, 227701 (2018).

[7] Gustafsson, M. V. *et al.* Propagating phonons coupled to an artificial atom. *Science* **346**, 207–211 (2014).

[8] O'Connell, A. D. *et al.* Quantum ground state and single-phonon control of a mechanical resonator. *Nature* **464**, 697–703 (2010).

[9] Hong, S. *et al.* Hanbury Brown and Twiss interferometry of single phonons from an optomechanical resonator. *Science* **358**, 203–206 (2017).

[10] Marinković, I. *et al.* Optomechanical Bell test. *Phys. Rev. Lett.* **121**, 220404 (2018).

[11] Riedinger, R. *et al.* Remote quantum entanglement between two micromechanical oscillators. *Nature* **556**, 473–477 (2018).

[12] Riedinger, R. *et al.* Non-classical correlations between single photons and phonons from a mechanical oscillator. *Nature* **530**, 313–316 (2016).

[13] Chan, J. *et al.* Laser cooling of a nanomechanical oscillator into its quantum ground state. *Nature* **478**, 89–92 (2011).

[14] Bochmann, J., Vainsencher, A., Awschalom, D. D. & Cleland, A. N. Nanomechanical coupling between microwave and optical photons. *Nature Phys.* **9**, 712–716 (2013).

[15] Vainsencher, A., Satzinger, K. J., Peairs, G. A. & Cleland, A. N. Bi-directional conversion between microwave and optical frequencies in a piezoelectric optomechanical device. *Appl. Phys. Lett.* **109**, 033107 (2016).

[16] Forsch, M. *et al.* Microwave-to-optics conversion using a mechanical oscillator in its quantum groundstate. *Nature Physics* **16**, 69–74 (2020).

[17] Balram, K. C., Davanço, M. I., Song, J. D. & Srinivasan, K. Coherent coupling between radiofrequency, optical and acoustic waves in piezo-optomechanical circuits. *Nature Photon.* **10**, 346–352 (2016).

[18] Stockill, R. *et al.* Gallium phosphide as a piezoelectric platform for quantum optomechanics. *Phys. Rev. Lett.* **123**, 163602 (2019).

[19] Ghorbel, I. *et al.* Optomechanical Gigahertz Oscillator made of a Two Photon Absorption free piezoelectric III/V semiconductor. *arXiv:1901.05922* (2019).

[20] Burek, M. J. *et al.* Diamond optomechanical crystals. *Optica* **3**, 1404 (2016).

[21] Jiang, W. *et al.* Lithium Niobate Piezo-optomechanical Crystals. *Optica* **6**, 845–853 (2019).

[22] Davanço, M., Ates, S., Liu, Y. & Srinivasan, K. Si_3N_4 optomechanical crystals in the resolved-sideband regime. *Appl. Phys. Lett.* **104**, 041101 (2014).

[23] Chan, J., Safavi-Naeini, A. H., Hill, J. T., Meenehan, S. & Painter, O. Optimized optomechanical crystal cavity with acoustic radiation shield. *App. Phys. Lett.* **101**, 081115 (2012).

[24] Aspelmeyer, M., Kippenberg, T. J. & Marquardt, F. Cavity optomechanics. *Rev. Mod. Phys.* **86**, 1391 (2014).

[25] Safavi-Naeini, A. H. *et al.* Observation of quantum motion of a nanome-chanical resonator. *Phys. Rev. Lett.* **108**, 033602 (2012).

[26] Guha, B. *et al.* Surface-enhanced gallium arsenide photonic resonator with quality factor of $6x10^6$. *Optica* **4**, 218–221 (2017).

[27] Higginbotham, A. P. *et al.* Electro-optic correlations improve an efficient mechanical converter. *Nature Phys.* **14**, 1038–1042 (2018).

[28] Arnold, G. *et al.* Converting microwave and telecom photons with a silicon photonic nanomechanical interface. *arXiv:2002.11628* (2020).

[29] Wu, M., Zeuthen, E., Balram, K. C. & Srinivasan, K. Microwave-to-optical transduction using a mechanical supermode for coupling piezo-electric and optomechanical resonators. *Phys. Rev. Applied* **13**, 014027 (2020).

[30] Alegre, T. P. M., Safavi-Naeini, A., Winger, M. & Painter, O. Quasi-two-dimensional optomechanical crystals with a complete phononic bandgap. *Opt. Express* **19**, 5658–5669 (2011).

[31] Mirhosseini, M., Sipahigil, A., Kalaee, M. & Painter, O. Quantum transduction of optical photons from a superconducting qubit. *arXiv:2004.04838* (2020).

[32] Jiang, W. *et al.* Efficient bidirectional piezo-optomechanical transduction between microwave and optical frequency. *Nature Comm.* **11**, 1166 (2020).

[33] Wallucks, A., Marinković, I., Hensen, B., Stockill, R. & Gröblacher, S. A quantum memory at telecom wavelengths. *arXiv:1910.07409* (2019).

[34] MacCabe, G. S. *et al.* Phononic bandgap nano-acoustic cavity with ultralong phonon lifetime. *arXiv:1901.04129* (2019).

[35] Ramp, H. *et al.* Elimination of thermomechanical noise in piezoelectric optomechanical crystals. *Phys. Rev. Lett.* **123**, 093603 (2019).

[36] Soderkvist, J. & Hjort, K. The piezoelectric effect of GaAs used for resonators and resonant sensors. *Journal of Micromechanics and Microengineering* **4**, 28–34 (1994).

[37] Midolo, L., Pregnolato, T., Kiršanskė, G. & Stobbe, S. Soft-mask fabrication of gallium arsenide nanomembranes for integrated quantum photonics. *Nanotechnology* **26**, 484002 (2015).

[38] Moore, J., Hendriks, H. & Morales, A. Characterization and control of galvanic corrosion during gaas wafer photoresist processing. *Proc. 2003 Intl. Conf. Compound Semiconductor Manuf.* (2003).

[39] Kelly, J. *et al.* State preservation by repetitive error detection in a superconducting quantum circuit. *Nature* **519**, 66–69 (2015).

[40] Watson, T. F. *et al.* A programmable two-qubit quantum processor in silicon. *Nature* **555**, 633–637 (2018).

[41] Hofheinz, M. *et al.* Synthesizing arbitrary quantum states in a superconducting resonator. *Nature* **459**, 546–549 (2009).

[42] Kurpiers, P. *et al.* Deterministic quantum state transfer and remote entanglement using microwave photons. *Nature* **558**, 264–267 (2018).

[43] Liao, S.-K. *et al.* Satellite-to-ground quantum key distribution. *Nature* **549**, 43–47 (2017).

[44] Boaron, A. *et al.* Secure quantum key distribution over 421 km of optical fiber. *Phys. Rev. Lett.* **121**, 190502 (2018).

[45] Witmer, J. D., Hill, J. T. & Safavi-Naeini, A. H. Design of nanobeam photonic crystal resonators for a silicon-on-lithium-niobate platform. *Opt. Express* **24**, 5876–5885 (2016).

[46] Fan, L. *et al.* Superconducting cavity electro-optics: A platform for coherent photon conversion between superconducting and photonic circuits. *Sci. Adv.* **4**, eaar4994 (2018).

[47] Wang, C. *et al.* Integrated lithium niobate electro-optic modulators operating at CMOS-compatible voltages. *Nature* **526**, 101–104 (2018).

[48] Rueda, A. *et al.* Efficient microwave to optical photon conversion: an electro-optical realization. *Optica* **3**, 597–604 (2016).

[49] O'Brien, C., Lauk, N., Blum, S., Morigi, G. & Fleischhauer, M. Interfacing superconducting qubits and telecom photons via a rare-earth-doped crystal. *Phys. Rev. Lett.* **113**, 063603 (2014).

[50] Hisatomi, R. *et al.* Bidirectional conversion between microwave and light via ferromagnetic magnons. *Phys. Rev. B* **93**, 174427 (2016).

[51] Stannigel, K., Rabl, P., Sørensen, A. S., Zoller, P. & Lukin, M. D. Optomechanical Transducers for Long-Distance Quantum Communication. *Phys. Rev. Lett.* **105**, 220501 (2010).

[52] Andrews, R. W. *et al.* Bidirectional and efficient conversion between microwave and optical light. *Nature Phys.* **10**, 321–326 (2014).

[53] Bagci, T. *et al.* Optical detection of radio waves through a nanomechanical transducer. *Nature* **507**, 81–85 (2014).

[54] Laer, R. V., Patel, R. N., McKenna, T. P., Witmer, J. D. & Safavi-Naeini, A. H. Electrical driving of x-band mechanical waves in a silicon photonic circuit. *APL Photonics* **3**, 086102 (2018).

[55] Moaddel Haghighi, I., Malossi, N., Natali, R., Di Giuseppe, G. & Vitali, D. Sensitivity-bandwidth limit in a multimode optoelectromechanical transducer. *Phys. Rev. Applied* **9**, 034031 (2018).

[56] Suchoi, O., Ella, L., Shtempluk, O. & Buks, E. Intermittency in an optomechanical cavity near a subcritical hopf bifurcation. *Phys. Rev. A* **90**, 033818 (2014).

[57] Zeuthen, E., Schliesser, A., Sørensen, A. S. & Taylor, J. M. Figures of merit for quantum transducers. *arXiv:1610.01099* (2016).

[58] Teufel, J. D. *et al.* Sideband cooling of micromechanical motion to the quantum ground state. *Nature* **475**, 359–363 (2011).

[59] Meenehan, S. M. *et al.* Pulsed Excitation Dynamics of an Optomechanical Crystal Resonator near Its Quantum Ground State of Motion. *Phys. Rev. X* **5**, 041002 (2015).

[60] Lee, K. C. *et al.* Entangling macroscopic diamonds at room temperature. *Science* **334**, 1253–1256 (2011).

[61] Ockeloen-Korppi, C. F. *et al.* Stabilized entanglement of massive mechanical oscillators. *Nature* **556**, 478–482 (2018).

[62] Meenehan, S. M. *et al.* Silicon optomechanical crystal resonator at millikelvin temperatures. *Phys. Rev. A* **90**, 011803 (2014).

[63] Skauli, T. *et al.* Improved dispersion relations for GaAs and applications to nonlinear optics. *J. Appl. Phys.* **94**, 6447–6455 (2003).

[64] Hill, J. T., Safavi-Naeini, A. H., Chan, J. & Painter, O. Coherent optical wavelength conversion via cavity optomechanics. *Nature Commun.* **3**, 1196 (2012).

[65] Galland, C., Sangouard, N., Piro, N., Gisin, N. & Kippenberg, T. J. Heralded Single-Phonon Preparation, Storage, and Readout in Cavity Optomechanics. *Phys. Rev. Lett.* **112**, 143602 (2014).

[66] Oz-Vogt, J., Mann, A. & Revzen, M. Thermal coherent states and thermal squeezed states. *J. Mod. Opt.* **38**, 2339–2347 (1991).

[67] Marian, P. & Marian, T. A. Squeezed states with thermal noise. i. photon-number statistics. *Phys. Rev. A* **47**, 4474–4486 (1993).

[68] Liu, Y., Davanço, M., Aksyuk, V. & Srinivasan, K. Electromagnetically Induced Transparency and Wideband Wavelength Conversion in Silicon Nitride Microdisk Optomechanical Resonators. *Phys. Rev. Lett.* **110**, 223603 (2013).

[69] Eichenfield, M., Chan, J., Camacho, R. M., Vahala, K. J. & Painter, O. Optomechanical crystals. *Nature* **462**, 78–82 (2009).

[70] Schneider, K. *et al.* Optomechanics with one-dimensional gallium phosphide photonic crystal cavities. *Optica* **6**, 577–584 (2019).

[71] Rivoire, K., Lin, Z., Hatami, F., Masselink, W. T. & Vučković, J. Second harmonic generation in gallium phosphide photonic crystal nanocavities with ultralow continuous wave pump power. *Opt. Express* **17**, 22609–22615 (2009).

[72] Wilson, D. J. *et al.* Integrated gallium phosphide nonlinear photonics. *arxiv:1808.03554* (2018).

[73] Bond, W. L. Measurement of the Refractive Indices of Several Crystals. *J. Appl. Phys.* **36**, 1674–1677 (1965).

[74] Nelson, D. F. & Turner, E. H. Electro-optic and piezoelectric coefficients and refractive index of gallium phosphide. *J. Appl. Phys.* **39**, 3337–3343 (1968).

[75] Balram, K. C., Davanço, M., Lim, J. Y., Song, J. D. & Srinivasan, K. Moving boundary and photoelastic coupling in GaAs optomechanical resonators. *Optica* **1**, 414–420 (2014).

[76] Mytsyk, B. G., Demyanyshyn, N. M. & Sakharuk, O. M. Elasto-optic effect anisotropy in gallium phosphide crystals. *Appl. Opt.* **54**, 8546 (2015).

[77] Diedrich, F., Bergquist, J. C., Itano, W. M. & Wineland, D. J. Laser cooling to the zero-point energy of motion. *Phys. Rev. Lett.* **62**, 403– (1989).

[78] Duan, L. M., Lukin, M. D., Cirac, J. I. & Zoller, P. Long-distance quantum communication with atomic ensembles and linear optics. *Nature* **414**, 413–418 (2001).

[79] Lake, D. P. *et al.* Efficient telecom to visible wavelength conversion in doubly resonant gallium phosphide microdisks. *Appl. Phys. Lett.* **108**, 031109 (2016).

[80] Lemonde, M.-A., Didier, N. & Clerk, A. A. Enhanced nonlinear interactions in quantum optomechanics via mechanical amplification. *Nature Commun.* **7**, 11338 (2016).

[81] Gröblacher, S., Hill, J. T., Safavi-Naeini, A. H., Chan, J. & Painter, O. Highly efficient coupling from an optical fiber to a nanoscale silicon optomechanical cavity. *Appl. Phys. Lett.,* **103**, 181104 (2013).

[82] Harabula, M.-C. *et al.* Measuring a quantum dot with an impedance-matching on-chip superconducting LC resonator at gigahertz frequencies. *Phys. Rev. Applied* **8**, 054006 (2017).

[83] Fang, K., Matheny, M. H., Luan, X. & Painter, O. Optical transduction and routing of microwave phonons in cavity-optomechanical circuits. *Nature Photonics* **10**, 489–496 (2016).